Energetics, synthesis, and structural characteristics of ferromagnetic metals for shape memory alloy and catalysis

Sawyer Morgan

A dissertation

submitted in partial fulfillment of the

requirements for the degree of

Doctor of Philosophy

University of Washington

2020

Reading Committee:

Daniel Schwartz, Chair

Qiuming Yu

Stephanie Valleau

Program Authorized to Offer Degree:

Department of Chemical Engineering

University of Washington

Abstract

Energetics, synthesis, and structural characteristics of ferromagnetic metals for shape memory alloy and catalysis

Sawyer Morgan

Chair of the Supervisory Committee:

Daniel Schwartz

Department of Chemical Engineering

The ferromagnetic metals iron and nickel have valence *d* electrons that allow for magnetic responsivity and catalytic activity, enabling their use in a variety of applications. The iron–palladium alloy $Fe_{70}Pd_{30}$ is a ferromagnetic shape memory alloy whose magnetostriction and pseudoelasticity can be exploited for potential use as a controllable nanoactuator. Here we synthesize and characterize $Fe_{70}Pd_{30}$ nanomaterials, a better understanding of whose properties at the nanoscale may lead to its practical deployment. We developed a pulsed electrodeposition and thermal annealing process to produce high aspect ratio nanowires in an alumina template and investigate the size effects on temperature-induced austenite–martensite phase transition with the crystal structure. We also explore the energetics of nickel surfaces to improve catalyst design for efficiency in industrial reactions. Here we measure the adsorption energies of formic acid and formate intermediates on nickel and nickel oxide (111) surfaces to provide benchmarks for more accurate calculations. This is performed by single-crystal adsorption calorimetry to directly measure heats of adsorbate formation.

Table of Contents

Acknowledgements

I would like to recognize my doctoral advisor Professor Minoru Taya (1944–2020), who provided supervision and support during my studies. He passed away during the progress of this work but he provided many contributions to the development of this dissertation and will have continuing impact in future of intelligent materials. Thanks to my group members Satoshi Yamamoto, Zhongjie Quan, Satomi Takao, and Cerwyn Chiew for their advice and collaboration on this project and for teaching me about Japanese, Chinese, and Malaysian cultures in this diverse group.

I would like to thank Liam Bradshaw, Samantha Young, Ellen Lavoie, and Scott Braswell for their help with analysis at the UW Molecular Analysis Facility; Darick Baker at the Washington Nanofabrication Facility; and Shogo Kawaguchi at SPring–8.

Thanks to Professor Charlie Campbell and my labmates Spencer Carey, Dr. Wei Zhao, Wei Zhao, James Lownsbury, and Stephanie Hemmingson for their advising and support during my first project.

A huge thank you to Professor Dan Schwartz for volunteering to be my new advisor after the death of Professor Taya and providing backing and guidance for completing my dissertation and defense, as well as to my committee members Professors Qiuming Yu, Stephanie Valleau, and Christine Luscombe (and former member Eric Stuve) for their flexibility and encouragement as COVID-19 disrupted UW operations.

I thank my parents Leslie and David and partner Seth for their support to push through to the end.

Chapter 1: Introduction

Ferromagnetic metals are studied for versatile applications derived from their unique electronic structure, allowing for iron, cobalt, and nickel, as well as many of their alloys, to be magnetized. This dissertation focuses on the use of nickel and iron, and how their structures provide for their use as catalysts and as shape memory alloys. Nickel is highly reactive and its stable (111) surface provides a platform for heterogeneous catalysis as its transition metal *d* block valence elections promote bonding with adsorbates. Iron alloyed with palladium has high magnetostriction and can change its lattice structure during cooling or under a magnetic field, resulting in volume change. These are among the diverse properties these ferromagnetic elements exhibit.

1.1 Catalysis

Heterogeneous catalysts are necessary for the vast majority of manufactured products in the chemical industry, including fuels, fertilizers, and specialty products. They can also facilitate reactions that remove pollutants from exhaust to improve air quality. To develop more efficient, cost-effective, and novel catalysts for variety of major applications, it is important to understand the characteristics of the metals involved and how their structures allow them to interact with reactive materials. The ferromagnetic elements are all late transition metals, in groups 8, 9, and 10 of period 4. They have valence electron configurations of $4s^2 3d^6$ (Fe), $4s^2 3d^7$ (Co), and $4s^2 3d^7$ (Ni), with the outer-shell electrons enabling their potential for ferromagnetism. For iron, four of the 3d electrons are unpaired, and when the magnetic moments of each atom are aligned in the same orientation they generate a magnetic field.

Catalysts have complex structures, typically taking the form of metal nanoparticles bound to supports such as alumina and silica to ensure distribution and maximize surface area. Variously sized metallic particles interact differently with different supports, depending on their crystal structure and surface morphology. Crystal lattice structures of the same element can take a variety of forms including cubic and tetragonal, both with simple, body-centered, and face-centered variations. Cutting the unit cells of the lattice structure with different plane intersections reveals a crystal face, the surface of which interacts with reactants in unique ways. Nickel and iron can both take the austenite phase, or face-centered cubic. The fcc phase cut by a plane with the same value in the x-, y-, and z-axes reveals the (111) surface with hexagonal symmetry and closest one-dimensional packing of atoms. With such spacing, interactions between the crystal surface and other molecules occur in particular manners, and better understanding this mechanism can provide generalized lessons about catalyst activity.

Theoretical techniques like density functional theory efficiently provide for effective modeling of molecular dynamics, demonstrating the catalysts' reactive mechanisms and how their structures influence their behavior. This allows for comparing known reactive species against a library of catalytic materials. However, experimentally known values for involved reactions are necessary to benchmark the theoretical values for steps involved in the catalytic process. Our experimental measurements of formic acid adsorption on Ni(111) and NiO(111) surfaces contributes to this comparison to this database for the optimization of DFT models. This allows for improved understanding of the interplay of elementary steps beyond the previously measured single atom adsorbate. Nickel and nickel oxide are widely used catalysts that are well studied but these experiments provide for newly reported measurements of adsorption energies with larger molecular fragments. Nickel catalysts are commonly used for hydrogenation

reactions,[1] used on broad classes of unsaturated chemicals for synthesizing pharmaceuticals and polymers.[2]

Both nickel and iron can act as catalysts because like other transition metals they can change their oxidation states, allowing them to accept or donate various numbers of electrons to a reacting molecule as needed. Iron is a particularly effective and widely used catalyst because its location at the center of the *d* block makes it versatile, formally able to reach the –II to +VI states,[3] though most stably in the Fe^{2+} and Fe^{3+} states, losing both its s orbital electrons and up to one of its *d* orbital electrons, leaving one electron in each of the five *d* suborbitals under Hund's rule. By splitting of the d-orbital energy levels, iron can form complexes in tetrahedral, octahedral, and square-planar configurations, allowing to bind with a variety of ligands. It has particularly high affinity to oxygen- and nitrogen-based ligands and cyclic carbenes, making it particularly effective for organic synthesis.[3], [4] While nickel most commonly loses the s electrons to form Ni^{2+}, such as in NiO, it can form compounds as Ni^{1+} to Ni^{4+}. Iron and nickel's surfaces allow for adsorption of materials and coordination to compounds in various configurations, helping them reach a lower-energy path to a product.

While characteristics of both the adsorbate and metal are relevant to the catalytic process, these free *d*-orbital electrons largely determine the adsorption binding energy.[5] As the d-band of the metal hybridizes between bonding (*d*-σ) and antibonding (*d*-σ)* states with the adsorbate's bonding (σ) orbital, the (*d*-σ) state fills up while the (*d*-σ)* is only partially full. The filling of the (*d*-σ)* orbital is then determined by the d-band center.[6] A higher d-band center, with higher energy relative to the Fermi level, has a less filled (*d*-σ)* state, with less destabilization in antibonding and therefore a stronger metal–adsorbate bond. The antibonding states can shift

above the Fermi energy and become empty while bonding states shift below it can fill up, increasing bond strength.[7] Conversely, a lower *d*-band center, with a larger difference between the center and Fermi level, is a weaker bond. This is applicable for hydrogen- and oxygen-containing adsorbents, so binding energy can be modeled for alloys with various combinations of metals, as alloying changes the lattice structure and electronic configuration of the surface. Bimetallic surfaces involving Ni, Pd, or Pt on other metals experience longer average bond lengths due to strain and ligand effects of bonding interactions. These combined can broaden or narrow the *d* band, decreasing or increasing the *d* band's average energy, respectively, to maintain constant filling. The surface *d* band not experiencing significant change in filling indicates negligible charge transfer between the metals.[8]

The volcano plot relates a catalyst's activity to its thermodynamic ability to adsorb a reaction intermediate.[9] The inverted-V shape derives from Sabatier's principle, which states adsorption energy should not be too high as to slow adsorption nor too low as to slow desorption, both of which would hinder the overall reaction rate.[10] There is a maximum reaction rate (or turnover frequency) between ascending and descending branches, each having heterogenous catalysts with endergonic and exergonic free energies of adsorption, respectively. While certain metals may be located away from the maximum rate peak for a particular reaction, alloying metals from either side of the peak may produce a compound that is located on the summit, with computation screening potentially determining the optimal catalyst.[11] Sabatier's principle however is not the only controlling rule, as hydrogen may bond both weakly and strongly, with either the overpotential or underpotential being more favorable at different points of adsorption coverage.[10]

Nickel's *d* bands are spin polarized, with an energy shift between bands with up or down

spin. This affects the 1s spin of hydrogen, which on other metals is polarized for a greater distance, but on Ni(111), the surface with the densest and stablest packing, it dissipates much closer to the nucleus. This is attributable to the H 1s up and down orbital spins forming bonding and antibonding peaks with the respective spin of nickel's 3d orbital. With nickel's compact 3d orbitals, the interaction with hydrogen is highly dependent on distance.[12] The result of this is that unlike other metals, Ni(111)'s adsorption of hydrogen occurs only strongly at the hollow site of the lattice, placing it on the right (descending) side of the volcano curve.[10]

For the decomposition of ammonia into hydrogen and nitrogen, ruthenium catalyst has a high reaction rate at the peak of the volcano plot, while the lower-cost iron and nickel catalysts are located on either side of the N_2 adsorption energy curve with lower reaction rates. This leads to a Ni–Fe alloy catalyst design that has similar catalytic activity to the noble metal at a lower cost.[13] An Fe(110) surface has a higher *d*-band center than Ni(111), so the adsorption energies of the reaction intermediates are higher. NH and H adsorb as *hollow* sites on Fe(110) rather than *fcc* on Ni(111), resulting in less catalytic activity.[14] For a Fe catalyst, adsorbed NH is the intermediate species during decomposition of NH_3, without presence of a stable NH_2 radical,[15] and partial dehydrogenation to NH_2 is the rate-limiting step of the mechanism over nickel,[16] suggesting how use of both metals promotes the reaction with lower adsorption energies from mixed sites.

When investigating suitability of catalysts for promoting complex reactions of diverse compounds, it can be done with analogous smaller molecules that are characteristic of the actively modified atoms that bind with the active sites. Formic acid (HCOOH) is a useful molecule to study because as the simplest carboxylic acid, it is representative of a large class of useful organic chemicals that may undergo catalyzed reactions or interact with surfaces. Its anion

formate ($HCOO^-$) is a typical intermediate during catalytic reactions. Since it is easily formed from CO_2 and H_2 or water, significant reactions such as methane steam reforming,[17] synthesis of methanol,[18] and the water-gas shift reaction[19], [20] involve formate. Understanding of the kinetics of formate can apply to those involving acetate (and acetic acid) and any other carbonate, which also act as catalytic intermediates. Formic acid is itself a useful chemical, used for leather tanning, preservation of animal feeds, mineral removal, and pharmaceutical and rubber manufacturing.[21] Production of formic acid from CO_2 can be a carbon-neutral replacement of the current fossil fuel synthesis process, and hydrogenation of CO_2 over Ni(111) may be a feasible method.[22] In Chapter 3, we measure the enthalpy of adsorption of formic acid and its anion formate on the (111) surface of nickel. One or both oxygen atoms bind to the clean metal surface as a monolayer forms from a molecular beam in a vacuum calorimeter. Understanding the energetics of this process can lead to better modeling of heterogeneous catalytic reactions involving carboxylic acids and design of nickel catalysts for industrial and environmental uses.

1.2 Alloys

Development of alloys for desired properties is based on tuning the presence of elements that either substitute into the primary matrix, usually a similar-sized atom, or intercalate into the gaps of the matrix, typically a much smaller atom. As they interact with neighboring atoms depending on their free electrons and coordination pattern, this creates inhomogeneities in the lattice structure that result in internal stresses due to differing tensile forces. This changes the metal's properties, often ideally to enhance hardness, toughness, or ductility.

The structure of the pure iron lattice produces a soft metal because the atoms are able to

slip around each other, but alloying it with a small amount of carbon hardens it into steel, as carbon atoms are forced into the interstices of the lattice and, with their coordination number of 4, strengthen the material. Certain types of steel are further strengthened by the addition of elements like chromium and molybdenum, which also resist corrosion due to their preferential oxidation. These are substitutional changes rather than interstitial. Nickel alloyed into iron along with chromium promotes austensitic stainless steel, which is preferred for its impact toughness and resistance to corrosion. However, this alloy loses iron's magnetization, as ferritic steel shifts from its body-centered cubic structure to the face-centered cubic structure of austenite. The higher-Fe bcc lattice allows movement of elections in the inner-core energy level, while the higher-Ni fcc lattice prevents alignment of the magnetic moment of Fe atoms due to the greater spacing between them.[23]

Other iron alloys promote interesting thermal and magnetic properties. Permalloy, an alloy of about 80% nickel and 20% iron, has magnetic permeability about 200 times greater than other iron alloys.[24] Its magnetostriction is near zero, making it optimal for applications that must avoid stresses, such as thin films for magnetic sensors and transformer cores.[25] This lack of change of shape during magnetization results from the very low magnetocrystalline anisotropy of the alloy's fcc structure.[26] The magnetic domains have little change in their borders during magnetization,[27] though for polycrystalline material the Fe/Ni composition for zero magnetostriction in the (111) and (100) directions is slightly different.[28] This derives from Fe and Ni having opposites signs in their anisotropy constants, with the former lattice being body-centered and the latter being face-centered which balance each other out in Permalloy.[29], [30] Permalloy's zero magnetostriction occurs at 20% iron because this is where the average number of *d* electrons per atom is an integer, with the electron contribution equally compensating for the

hole contribution in the *d* band with down spin.[31]

Inconel is a family of alloys that is highly resistant to corrosion and oxidation, also known as a superalloy. Like Permalloy its composition is majority nickel and therefore has an austenite structure. The high amount of its secondary metal, chromium, provides for a passivating oxide layer on the surface, preserving the bulk from further oxidation. It maintains strength at high temperatures, as crystal vacancies prevent creep deformation. About 5% niobium added results in the tetragonal structure Ni_3Nb, forming the γ″ phase, a precipitate within the primary γ phase formed during age hardening. The impurity inhibits dislocations of the primary crystal lattice and results in a harder material for use in extreme conditions.[32] Certain alloys in the Inconel family, such as alloy 783, were developed to have very low coefficient of thermal expansion,[33] putting it among many high-nickel alloys that experience little thermal expansion (around $14x10^{-6}$ m/m°C),[34] making them useful for precision environments like aerospace and automobiles. This is also due to the γ″ precipitate, which produces a slight tetragonal distortion in the fcc matrix, preventing the increase in grain size during heating.[35]

Even lower coefficients of thermal expansion are observed in the Invar (invariable) alloy, with a CTE of $1.2x10^{-6}$ m/m°C or even lower. With composition $Fe_{64}Ni_{36}$, it is a single-phase solid solution, without precipitates, but its consistent structure can result in creeping. The Invar effect only occurs below the Curie temperature, while the material is ferromagnetic.[36] Although the exact mechanism behind this property is still debated, it arises from the magnetic structure, which has a transition from an ordered ferromagnetic state to a disordered non-collinear configuration. While anharmonic lattice vibrations result in lattice expansion, this is compensated for by thermal excitations between high- and low-volume magnetic states.[37] Conversely, while invar has no volume change from temperature effects, it has significant

expansion from magnetostriction.[36]

Unlike permalloy but like invar, the ferromagnetic $Fe_{70}Pd_{30}$ alloy has very high magnetocrystalline anisotropy and magnetostriction, providing for significant shape deformation in presence of a magnetic field, with a transition from austenite phase to martensite phase.[38] Magnetic field-induced strain reaches saturation of 3.1% under a 1 MA/m (~1.2 T) field, the full rearrangement between cubic and tetragonal variants.[39] The parent austenite phase is highly symmetric, and temperature cooling or a magnetic field induces a slight shift, producing a twin phase with a single symmetric boundary perpendicular to the direction of the magnetic moment.[38] This has minimal shear stress and experiences no volume change until the phase deformation to martensite is complete, as the magnetic moments in each unit cell align with the external field, moving the domain walls. This is expected due to the higher saturation magnetization of martensite than austenite. When the temperature increases again or the magnetic field is removed, the material returns to its original austenite phase. Its pseudoelasticity enables the stretching of the atomic bonds during reconfiguration without permanent deformation, resulting in reversal of changes in domains as the strain disappears. The most significant strain derives from this martensite variant reorientation. Magnetostriction from coupling of electron spin orbits occurs but does not contribute as much strain.[38] Ni_2MnGa also exhibits this shape memory alloy effect, with ferromagnetism as a Heusler compound linked to the ferroelastic domain walls.[40], [41] It however is too brittle for use as an actuator, and nickel may cause a variety of health issues.[42] $Fe_{70}Pd_{30}$ is known to be biocompatible and usable for medical applications.[43]

In Chapter 2, we investigate a route for synthesis of this iron alloyed with palladium that would exhibit the ferromagnetic shape memory alloy effect. While it is well described at the

macro-scale, the characteristics of the nano-sized alloy are not as defined. We sought to understand the relationship between the austenite–martensite phase transition and its initiators in the context of nanomaterials for potential use as biomedical actuators. The transition temperature is suppressed in the produced nanowires, but it could not be determined during our experiments, which were cut short by the passing of our principal investigator.

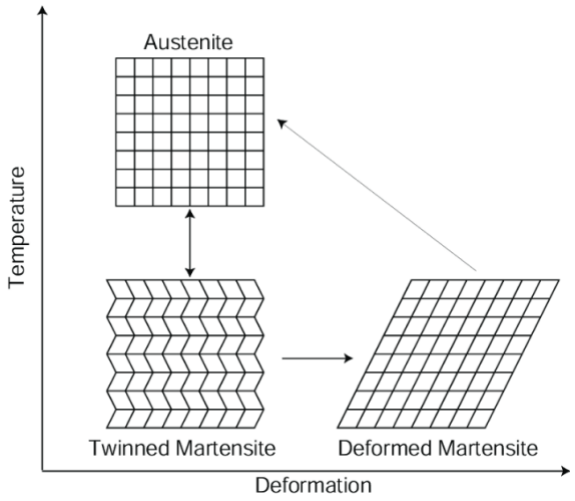

Figure 1. Shape memory alloy cycle between austenite, twinned martensite, and deformed martensite lattices.[44] Magnetic moments in mirrored twinned cells are angled, while in deformed martensite they are parallel.

1.3 Oxidation

Oxidation of FePd alloy diminishes the SMA effect. Oxygen can react with iron on the surface and diffuse into the bulk via grain boundaries, creating non-magnetic structures in the alloy that will not undergo phase transformation.[45] Gradual exposure to oxygen in the air or rapid exposure during heat treatment leads to destabilization of the martensite phase: In NiMnGa, high temperature annealing resulted in growth of oxide nanorods and grains in the microstructure, resulting in decreased magnetic saturation and less intense martensite XRD peaks.[46] In the SMA NiTi, a titanium oxide layer forms on the surface at high temperature

changing the stoichiometry in adjacent regions. This inhibits martensitic transformation as phase change temperature decreases significantly, and slip deformation at the new grain boundaries causes greater plastic strain.[47] Undesired oxidation can be prevented by annealing in vacuum or reducing environment without oxygen.

For iron and nickel, like all other elements except the noble gases and noble metals, ionic bonding with oxygen is more thermodynamically stable than the metallic bond with itself. This lends to the formation of oxides. Because iron and nickel have relatively low electronegativity in the *d* block and do not stabilize their valence electrons well, oxygen, being the second-most electronegative element, will preferentially accept two valence electrons to form a stable compound. Iron typically oxidizes to FeO, Fe_2O_3, and Fe_3O_4, in the ferrous (II), ferric (III), and mixed (II, III) oxidation states, respectively. In iron oxides, the valence band is primarily the 2p band of oxygen, and the conduction band consists of iron's 4s band. The metallic 3d band is partially filled between the 4s and 2p bands. This is more complicated with the Fe(III) ions, where charge can transfer from the 3d band to that of a neighboring ion or to the 4s band. With an octahedral structure, there is a bandgap of 2 eV, making it a semiconductor useful in catalysis and photocatalysis using both the iron cation and oxygen anion as active sites depending on whether electrons are transferred from the *d* band or holes from the p band.[48] Oxidation can occur both by reaction with molecular oxygen and by the adsorption and splitting of water. On clean Fe(100) and Fe(110) surfaces, H_2O dissociates into hydrogen and hydroxyl groups, but as surface coverage increases, water does not spontaneously split due to an increased energy barrier. With adsorbed oxygen the magnetic surface causes a spin-up–spin-down splitting.[49]

Nickel oxidizes to NiO and rarely Ni_2O_3. When a Ni(111) surface oxidizes, it undergoes

three stages of reaction: chemisorption, NiO island growth, and NiO thickening: *d* band valence electrons shift in energy +1 eV above the Fermi level during oxidation as ionic bond form.[50] As oxygen exposure increases, nickel's *d* band gradually disappears so there is little electron density at the Fermi level, with oxide growth occurring logarithmically.[51] While nickel is ferromagnetic with parallel aligned magnetic moments, NiO (as well as FeO and α-Fe_2O_3) is antiferromagnetic with antiparallel neighboring moments, as the nickel ions have alternating up and down spins and different exchange interaction with neighbors and next-nearest neighbors. The *d* orbitals are split between the higher energy e_g and lower energy t_{2g} orbitals with a wide gap inhibiting $d \rightarrow d$ transitions but allowing $p \rightarrow d$ hybrid transitions.[52]

Because the O_{2-} anions are larger than the M_{n+} cations, the surface metal atoms have lower coordination to the bulk and are less accessible to catalyzed reacting molecules.[53] It serves as a catalyst for reactions such as N_2O decomposition and CO_2 formation as the material facilitates election flow by accepting electrons at nickel sites as well as supplying electrons at oxygen sites, acting as acid-base pairs. In Chapter 4, we measure the energetics of the formic acid adsorbate on the (111) surface of nickel oxide as it dissociates, with the heat of adsorption decreasing as coverage increases to saturation. Formic acid adsorbs as formate on nickel sites and hydrogen adsorbs as a hydroxyl group with an oxygen site. While NiO has an octahedral structure, it often occurs non-stoichiometrically with cation vacancies.[54] This makes it a p-type semiconductor, which react more readily with reducing elements. Adding dopants further affects catalytic activity as they shift the Fermi level of the oxide: Lithium doping decreases it, while indium doping increases it; a mixture of the two rearranges the electron arrangement at the interface of crystals to balance it as they transfer from the indium- to lithium-doped oxides.[55] The delocalized electrons result in the oxide having similar catalytic properties as base metals.

Chapter 2: Synthesis and Characterization of $Fe_{70}Pd_{30}$ Shape Memory Alloy Nanomaterials

2.1 Introduction

Many researchers are seeking new approaches toward treatment of cancers, including targeted attacking of tumor cells by mechanical force instead of or in conjunction with certain specific and non-specific chemotherapy drugs. A possible method of inducing mechanical stress on cells is by use of nanorobots (NRs), mechanical devices on the scale of nanometers in dimension. Design of these nanorobots may be based on scaling down micro-sized robots so that they may be more precisely controlled and have more versatility during *in vivo* use for performance on the subcellular level. Control of NRs requires a method of actuation, which can include thermal,[56] piezoelectric,[57], electrostrictive, and magnetostrictive methods.[58] Another possible method is actuation from the volume change in the phase transformation of shape memory alloys,[59] which must be better understood at the nanoscale for practical biomedical use.

Spring-shaped microrobots inspired by bacterial flagella is one guidable design that has been investigated, using an applied magnetic field for propulsion,[60] and these magnetic devices have been demonstrated for use as carriers of drugs for targeted delivery to cancer sites.[61] A helical design that is small enough to have flexibility could respond elastically to an applied magnetic field, allowing the NRs to not only transport drugs to specific sites but also perform treatment there. The NRs could actuate to apply mechanical stress to cells they touch, provoking apoptosis. The mechanism of actuation is associated with the proposed NRs' composition as a ferromagnetic shape memory alloy (FSMA), $Fe_{70}Pd_{30}$. FePd is a nontoxic alloy

whose composition and crystal structure provide it distinctive structural and magnetic properties that can give it applications for sensing or actuation.[62]

Under an applied magnetic field, bulk $Fe_{70}Pd_{30}$ can undergo a phase transformation between the martensite phase and austensite phase, dependent on the stress (σ), temperature (T), and magnetic field (H). The FSMA transforms and may cause a temporary deformation along the spring axis due to a field-induced phase transformation, a martensite variant rearrangement of crystals, or a combination of both.[63] This hybrid mechanism results in rapid actuation and displacement following phase change from applied magnetic flux. This process has been demonstrated at the macroscale,[59] and we aim to produce nanorobotic actuators that will behave with similar properties in a biological environment. 1-D nanowires' high aspect ratio provides for high shape anisotropy, allowing for enhanced orientation of magnetic moments along the axis and high magnetic density. Molecular dynamics simulations have modeled FePd nanohelices, determining the shrinkage from an applied H field.[64] However, the nanoscale alloy exhibits FSMA transitions under different conditions from the macroscale, so the relationship between the stimuli of the phase transformation must be understood.

2.2 Background

2.2.1 FePd shape memory alloy

$Fe_{70}Pd_{30}$ is an example of a shape memory alloy (SMA), a material that when subjected to thermal, stress, or magnetic forces responds with strain that is reversible when the loading is removed. This property makes FePd and other SMAs materials of interest as devices for actuation and sensing. A ferromagnetic SMA (FSMA) like FePd can actuate at much greater frequency due to the ability to rapidly switch a magnetic field than a thermal gradient, and it can

also be controlled at a greater range without affecting nearby materials. The reversible phase transformation from austenite phase to martensite phase is what enables this shape memory effect, as the crystal structure shifts from a highly symmetric to less symmetric pattern.

For temperature change-induced shape memory effect, cooling the SMA beyond the martensite start temperature shifts the positions of atoms in the original austenite lattice, deforming the shape while retaining the volume. When heating the SMA back up, it returns to the original austenite phase in its 'memory'. Applied stress can have the same effect, stabilizing the martensite phase, though at higher temperature higher stress is needed to begin the martensite phase shift.[65] The magnetic-field induction of shape change is due to the alignment of the magnetic moment of Fe atoms in the crystal structure. With applied magnetic field the unit cells will strain and shift to match their moment to the direction of the magnetic field.[65] $Fe_{70}Pd_{30}$ can display up to 0.6% magnetic field-induced strain (the strain in an axial field), one of the largest among FSMAs, in response to a 1 T field,[38] which makes it a desirable material for such actuation applications. The ability of this material to demonstrate this behavior is however dependent on its lattice structure, which is highly determined by composition.

The high temperature alloy (above 1043 K) will form the austenite face-centered cubic (γ) phase, which is only maintained at room temperature when quickly quenched, as shown in Figure 1.[66] The fcc phase will decompose to $Fe_{50}Pd_{50}$ and α-Fe,Pd bcc phases if cooled slowly as iron can diffuse in a high-temperature lattice.[67] The metastable fcc phase of $Fe_{70}Pd_{30}$ must be maintained to exhibit ferromagnetic shape memory alloy properties. In bulk FePd (30 at% Pd), transformation to the martensite face-centered tetragonal (γ') phase was found by Matsui to begin to occur just below room temperature, with the martensite transition starting temperature (Ms) at 250 K and martensite transition finishing temperature (Mf) between 197 K and 37 K.

Transition was also observed for 32 and 33% Pd bulk alloy, but at significantly lower temperatures, 184 and 84 K, too low to easily observe and not useful for FSMA applications. At much lower Pd at% (24% and 26%) only α bcc phase is present. At a slightly lower Pd at% (28%) the alloy begins with the γ phase at high temperature, but quenching speed will influence the room temperature composition. With a fast quenching, there was an irreversibly mixed α + γ′ bct, favoring the fct, but for slower quenching, the fraction of fct was much lower.[66] Another study of bulk $Fe_{70.3}Pd_{29.7}$ found Ms at 290 K, with bct phase appearing below 183 K.[68]

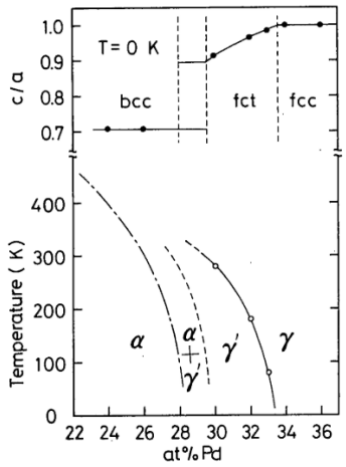

Figure 1. Phase diagram of quenched $Fe_{70}Pd_{30}$ at lower temperatures with austenite–martensite transformation shown as solid curve on right.[66]

In a thin film experiment (produced by pulsed laser deposition and annealed)[69] $Fe_{72}Pd_{28}$ saw transformation from fcc (200) peaks to fct (200) at 175 K (Ms), with peak shift and broadening representing a slight decrease in the *c*/*a* lattice constant ratio as temperature decreased to 125 K. The primary cause for the peak broadening is inhomogeneity in the tetragonal phase due to less transformation at the interface of the film with the MgO substrate. However, residual austenite phase remained present at these temperatures. With 33% Pd, no phase transformation was observed above 125 K.

As evident in the change in Ms temperature from bulk to film, size-dependence of the transformation temperature is expected to result in a colder transition due to a larger surface area to volume ratio. In a study[70] of FePd nanoparticles (formed by gas evaporation from annealed and quenched ingots) with an average diameter of 24 nm, room temperature nanoparticles with both 30.8% Pd and 27.5% Pd exhibited XRD peaks for both fcc and bcc phases, indicating variation in the distribution of composition among the nanoparticles. XRD of the nanoparticles did not display changes between room temperature and 77 K: there was no martensite transformation, although it was expected for 27<Pd%<31.5.[71] The phase transformation temperature for these samples would be lower than 77 K, if occurring at all. The cause of the lack of observed transition in nanoparticles, if not below this, could not be explained by the authors. Additional bulk polycrystalline samples with 30.1% Pd had volume-weighted average grain sizes of 2.6–9.9 μm and were broken into powdered samples with size 10s–100s of μm. The original bulk sample with grain size 266 μm underwent Ms at 289 K, and the polycrystalline samples with grain size 9.9, 6.1, and 2.6 μm did so at 253, 231, and 195 K, respectively.[70]

Finally, nanowires reported to be $Fe_{69\pm3}Pd_{31\pm3}$ in alumina template were measured with XRD at room temperature and at 73 K.[72] These had a 200 nm diameter and 2 μm length, with similar synthesis procedures as presented here. While there was a slight shift in the (111) and (200) peaks to indicate a mixture of fcc and fct phases at the low temperature, just beginning martensite at the nanoscale-adjusted transition start temperature Ms′, it was not the full peak splitting as seen in the above polycrystalline samples, showing that the nanoscale transition finishing temperature Mf′ is much lower. The small grain sizes make it harder for martensite nucleation to propagate without further temperature or stress changes.

These results show that the ability for a sample to undergo a phase transition is highly

dependent on composition, with Pd content above 30% suppressing it to lower temperatures and content slightly below 30% possible but dependent on other parameters for the extent of it. Excessive variation or incorrect quenching will suppress the single fcc austenite phase needed for a FSMA transition.

2.2.2 Electrodeposition of FePd

Nanowires can be patterned using a variety of techniques, including vapor–solid deposition, focused ion beam etching, and electron-beam lithography, but these are not suited for efficient mass production. A cheaper and higher-yield method is electrodeposition in an ordered nanotemplate, such as porous anodic aluminum (PAA). A PAA template with hexagonal packed pores can be fabricated with controllable pore sizes and depths, in which nanowires of a variety of materials can be produced by electrodeposition.

The FePd alloy is electrodeposited from metals ions in solution to become a solid on the surface of the electrode. The system is an electrochemical cell with an applied external potential which drives electron exchange between electrode and ions. Electrodeposition occurs as metal cations in solution ($M_{z+solution}$) undergo reduction at the surface of the cathode to grow the metal solid, according to the generalized reaction:[73]

$$M_{z+solution} + ze^{-} \rightarrow M_{0solid} \qquad \text{RXN (1)}$$

As this is a surface-based reaction it is heterogeneous and occurs at the rate

$$Rate\ [mol^{-1}\ sec^{-1}\ cm^{-2}] = i/zFA = j/zF$$

Where A is electrode area, i is current, and j is current density. This reaction rate is determined by the slower of mass transport to the surface of the electrode or electron transfer kinetics.

Mass transport inside the high aspect ratio nanopores of PAA is mainly controlled by

diffusion, as a concentration gradient induces movement of species to balance out their distribution in the system and maximize entropy, and convection external to the template. As the electrochemical reaction proceeds, the metal ion concentration is lower in the vicinity of the reaction site, resulting in a concentration gradient. In the immediate diffusion layer, metal ions flux from the bulk toward the electrode surface, as governed by Fick's first law:

$$-J_M(x,t) = D_M \cdot \delta C_M(x,t)/\delta x$$

where J_M is the flux of species M and D_M is its coefficient of diffusion. To minimize mass transfer limitations in the bulk electrolyte outside of the PAA template, stirring with a magnetic bar provides forced convection that keeps the concentration of ions throughout the solution constant. The kinetics of electron transfer are driven by the applied voltage that provides a negative overpotential on the working electrode, a deviation from the equilibrium interfacial potential, that allows electron transfer and reduction of the ion as given in RXN (I).[73]

For FePd alloys, a stable electrolyte that will reproduce the desired compositions is required. Ideally, both ions in the plating bath have similar electrode potentials to enable optimal simultaneous co-deposition. Because Fe(II) will spontaneously reduce Pd(II) ions due to the large difference in their standard potentials, complexed Fe(III) and Pd(II) ions are preferred, which will adjust the reversible potentials. Sulfosalicylic acid is one electrolyte that has been shown to complex Fe to allow codeposition of FePd.[74] Varying the voltage and with that current density will adjust the deposited Fe at% in the alloy. Because of the rather negative deposition potential of the complexed species, and use of water as the electrolyte solvent, deposition is not 100% efficient, and we get the side reaction:

$$2H_2O + 2\ e^- \rightarrow H_2 + 2OH^- \qquad \text{RXN (2)}$$

A pulse-plating method of deposition is used due to the high aspect ratio of the PAA

template, which slows diffusion of metal ions to the reaction surface and allows build-up of hydrogen and hydroxide within the pores. Each pulse of voltage E_1 for length t_1 is followed by a relaxation time t_2 with no applied current. The relaxation period allows for the depleted metal ion concentration gradient at the surface to recover toward equilibrium, allowing better compositional control of the deposited metal. Relaxation also allows secondary products H_2 and OH^- to diffuse out of the pores prior to deleterious effects such as gas bubble formation or a pH rise that causes metal hydroxide precipitation, either of which can block pores or lead to other nanowire defects.[75]

2.2.3 Stress-induced austenite–martensite phase transformation shift

To develop NRs for useful applications, the phase transformation characteristics must be understood to guide the NRs by driving stimuli, two of which are temperature (T) and stress (σ), as shown in Figure 2 as the horizontal and vertical axes. For bulk-phase $Fe_{70}Pd_{30}$, the boundary line between martensite and austenite phases, with respect to temperature and stress, is shown as the lower line, labeled $\Delta G\#(T) = 0$, where the friction energy required to overcome martensite variant growth is zero. Here with $\sigma=0$, the martensite phase begins to appear when the temperature decreases from room temperature (RT) to the martensite start temperature (Ms), where the line intersects with the temperature axis. For bulk $Fe_{70}Pd_{30}$, Ms is 281 K, and Mf, the temperature when the martensite phase transformation is finished (not shown) is 273 K;[69] the austenite transition temperatures on warming are As =283 K and Af =289 K.[63] Due to the larger surface area to volume ratio at the nanoscale allowing for relatively more nucleation sites,[76] this characteristic is expected to be shifted for nano-sized FePd. Tadaki et al. investigated transition temperatures of three dual-phase SMAs, Fe-Ni[77], Au-Cd[76] and Fe-

Pt[78]. Matsuoka et al.[79] studied the size effect on SMA properties of Au-Cd-Ag alloy and concluded that, since the ratio between surface area and volume is greatly increased in nano-sized SMAs, the effect of surface energy is responsible for the reduction of phase transformation temperatures in nano-sized SMAs. Seki et al.[70] reported the absence of phase transformation from austenite to martensite phases in spherical FePd nanoparticles even at lower temperature. This shift is depicted with the line labeled ΔG##(T) = 0, which has the new martensite start temperature at Ms′ at a decreased temperature.

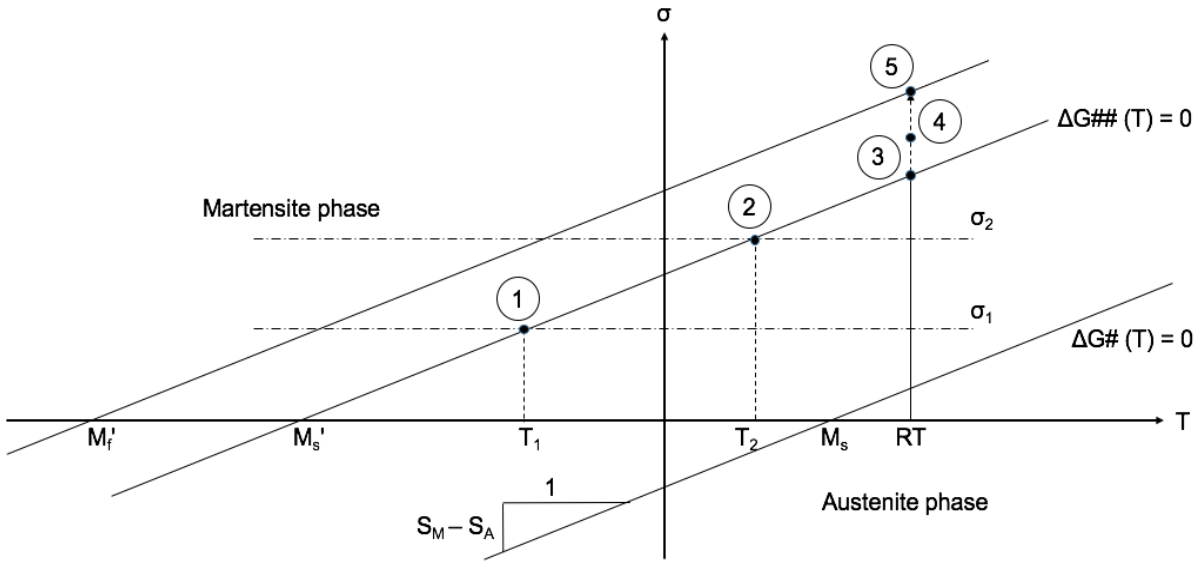

Figure 2. Phase transformation diagram of bulk and nano-sized $Fe_{70}Pd_{30}$. The boundary lines of the phase transformation diagram of bulk (ΔG#(T) = 0) and nano-sized FePd (ΔG##(T) = 0) under stress (σ) and temperature (T) intersect with the temperature axis at Ms and Ms′, respectively. The effects of nano-size are expected to shift Ms to Ms′ at a lower temperature. Also shown is the stress-induced martensite (SIM) phase transformation in vertical solid/dashed line at room temperature (RT).

For biomedical uses, cryogenic temperatures are not feasible, and the nanomaterials must be tuned to have a Ms′ closer to room temperature or body temperature. This may be able to be achieved by moving along the martensite–austenite boundary in the direction of increasing

stress. Residual stress may be induced in the NRs through high-temperature annealing as the structure is homogenized. After processing the NRs by electrodeposition in an alumina template of hexagonally ordered holes with diameter approximately 50 nm, the embedded NRs can be heated to 900°C, recrystallizing the lattice structure. While the coefficient of thermal expansion of alumina is $8.4 \cdot 10^{-6}$/°C,[80] that of FePd is $11.8 \cdot 10^{-6}$/°C. This mismatch will result in stress build-up in the NRs, which is not relieved as the sample is quickly quenched in water after annealing.[64]

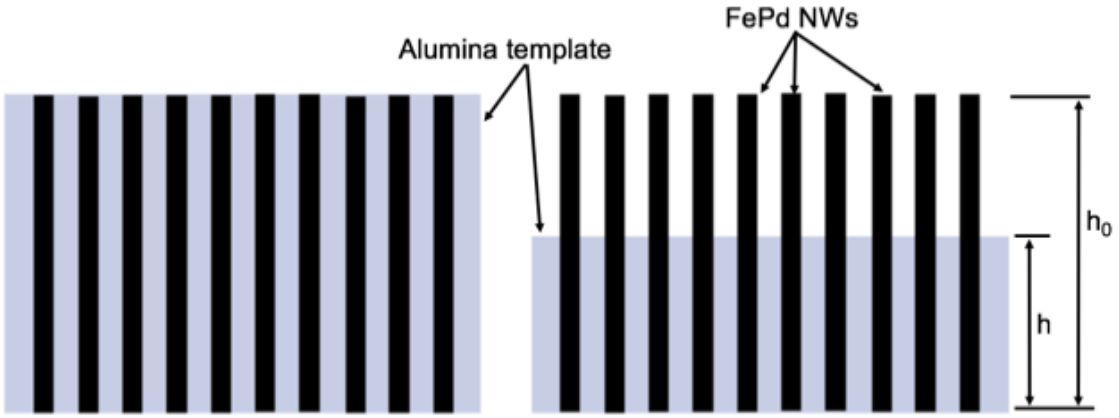

Figure 3. FePd nanowires embedded in alumina template, which can be reduced in thickness from h_0 to h

The resultant residual stress is dependent on the portion of the NR that is embedded in the alumina. The initial thickness of the alumina template, denoted as h_0 in Figure 3, will produce the maximum residual stress. Etching away the alumina to a thickness of h will produce a smaller average residual stress following annealing, as it is confined to a smaller portion of the NRs. σ_1 and σ_2 are expected to proportionally correspond to the residual stress from templates with thicknesses h_1 and h_2, where $h_1 < h_2$. Stress-induced martensite phase transformation then occurs, as shown by the vertical dotted lines to ① and ②, with the line passing through them indicating the martensite–austenite boundary. T_1 and T_2 indicate the new shifted Ms′ temperature

values for the stressed materials. Analysis by XRD can provide the temperatures of these points by detecting the onset and completion of shifts in XRD spectra from fcc to fct peaks.

Surface residual stress σ can be measured by XRD, as it results in a different d spacing from that of unstressed FePd. The residual stress can also be predicted from a dislocation model of punching at the interface between FePd and alumina. Measuring the residual stress at room temperature yields the point marked at ③, which would be compared to the predicted value. The uppermost line in the diagram is drawn from Mf′, measured from XRD data, parallel to the previous line; the slope S_M–S_A is the change of entropy during austenite–martensite phase transformation and is assumed to be the same at both nano and macro sizes. The dotted line between ③ and ⑤ indicates the stress-induced martensite transformation. As the bottom of this line represents a fully austenitic sample and the top a fully martensitic sample, the volume fraction of each phase can be calculated when the FePd nanomaterial is in this transition region. From this the shear modulus of the overall sample may also be approximated from the weighted shear moduli of pure austenite and martensite phases.

2.3 Models of thermodynamics and residual stress in martensite phase transformation

This section adapted with permission from [81]. These theoretical models were developed by Professor Minoru Taya.

2.3.1 Thermodynamic model for phase transformation of FePd

Here we discuss the effects of nano-sized FePd on the stress-induced martensite from the thermodynamic viewpoint. The Gibbs free energy change, ΔG, is given by

$$\Delta G = \Delta F - \sigma \Delta \varepsilon \quad (1)$$

where ΔF is Helmholtz free energy change and σ and Δε are the stress and strain change.[82] In

order to realize the phase transformation from austenite to martensite, the following inequality must be satisfied:

$$\{\Delta G\}_{A\rightarrow M} = \{\Delta G\}_M - \{\Delta G\}_A = \{\Delta F\}_M - \{\Delta F\}_A - [\{\sigma\Delta\varepsilon\}_M - \{\sigma\Delta\varepsilon\}_A] \leq 0 \quad (2)$$

where subscripts A and M denote austenite and martensite phase, respectively. The change in the Helmholtz free energy from austenite to martensite is given by

$$\Delta F_{A\rightarrow M} = F_M - F_A = \Delta H_{A\rightarrow M} - T(S_M - S_A) \quad (3)$$

where $\Delta H_{A\rightarrow M}$ is enthalpy change from austenite to martensite phases, S_i (i = A or M) is the entropy of the i-th phase, and T is absolute temperature. Substituting eq. (3) to the first term on the right side of inequality (2), we obtain

$$[\{\sigma\Delta\varepsilon\}_M - \{\sigma\Delta\varepsilon\}_A - \Delta H_{A\rightarrow M} + T(S_M - S_A) \geq 0 \quad (4)$$

The second and third terms on the left side of this inequality are redefined as friction energy, $\Delta G^{\#}(T)$:

$$\Delta G^{\#}(T) = -\Delta H_{A\rightarrow M} + (S_M - S_A)\, T \quad (5)$$

This friction energy is the energy required to overcome the growth of martensite variants, which indicates the boundary line between austenite and martensite phases shown in Figure 2; its slope is the change of entropy during austenite-martensite phase transformation, $S_M - S_A$. Therefore inequality (4) becomes

$$\{\sigma\Delta\varepsilon\}_M - \{\sigma\Delta\varepsilon\}_A + \Delta G^{\#} \geq 0 \quad (6)$$

When the surface energy effect of nano-sized FePd is considered, inequality (6) is rewritten as

$$[\{\sigma\Delta\varepsilon\}_M - \{\sigma\Delta\varepsilon\}_A]\, V + \Delta G^{\#} V + \{\gamma_M - \gamma_A\} S \geq 0 \quad (7)$$

where γ is the surface energy per unit area, and V and S are the volume and surface area of nano-sized FePd, respectively.

To simplify the thermodynamic model, in the case of a spherical nanoparticle (NP) with radius r

($V = 3\pi r^3/4$, $S = 4\pi r^2$), equation (7) is reduced to

$$[\{\sigma\Delta\varepsilon\}_M - \{\sigma\Delta\varepsilon\}_A] + \Delta G^{\#} + (3/r)\{\gamma_M - \gamma_A\} \geq 0 \quad (8)$$

By combining the second and third terms of the left side of eq. (8) as the modified friction energy $\Delta G^{\#\#}(T)$, inequality (8) is rewritten as

$$[\{\sigma\Delta\varepsilon\}_M - \{\sigma\Delta\varepsilon\}_A] + G^{\#\#}(T) \geq 0 \quad (9)$$

where

$$\Delta G^{\#\#}(T) = \Delta G^{\#} + (3/r)\{\gamma_M - \gamma_A\} \quad (10)$$

By setting eqs. (5) and (10) to zero, the martensite and austenite phase boundaries for bulk and nano-sized FePd are given as shown in Figure 2, respectively, where hypothetical residual stress levels are represented as σ_1 and σ_2.

It is suggested in Figure 2 that the effect of residual stress in FePd NWs and NHs is a major impact on the stress-induced martensite (SIM) phase transformation, as indicated by the vertical dashed line at the points ① (at T1 under σ_2), ② (at T2 under σ_1) and ③-④-⑤ (at RT). Therefore, the suppression of the martensitic transformation in nanosized FePd could be overcome by existence of residual stress even at RT (③, ④, ⑤). The values of the residual stress introduced in FePd NWs and NHs are discussed in terms of Eshelby models and dislocation models in following sections.

2.3.2 Eshelby's model for residual stress in FePd nanomaterials

Based on Eshelby's model with Mori-Tanaka mean field theory[83]–[86] residual stress of FePd nanowires (NWs) and nanohelices (NHs) in alumina template can be mentioned in terms of inhomogeneity problem as follows:

$$\boldsymbol{\sigma = C_f \bullet (e + \hat{e} - e_p) = C_m \bullet (e + \hat{e} - e_p - e^*) = C_m \bullet (e + \hat{e} - e^{**})} \quad (11)$$

$$\boldsymbol{e^{**} = e_p + e^*} \quad (12)$$

$$\boldsymbol{e = S \bullet e^{**}} \quad (13)$$

where bold face symbols $\boldsymbol{\sigma}$ and **e** are stress and strain tensors, **e** is average matrix strain, $\hat{\mathbf{e}}$ is the local strain disturbance, $\mathbf{C_f}$ and $\mathbf{C_m}$ are stiffness tensors for inclusion and matrix phases, **S** is Eshelby's tensor, $\mathbf{e^*}$ is equivalent eigenstrain, $\mathbf{e^{**}}$ is total eigenstrain in equivalent inclusion system, and $\mathbf{e_p}$ is the prescribed eigenstrain (or coefficient of thermal expansion (CTE) mismatch strain) given by

$$\boldsymbol{e_p} = \Delta T \, \Delta\alpha \, (1, 1, 1) \quad (14)$$

where ΔT is the temperature change during the cooling stage and $\Delta\alpha$ is the difference between the CTE of FePd (α_{FePd}) and alumina template ($\alpha_{alumina}$), i.e., $\Delta\alpha = \alpha_{FePd} - \alpha_{alumina}$. $\mathbf{C_f}$ and $\mathbf{C_m}$ in eq. (11) are the stiffness tensors of FePd and alumina matrix, respectively.

Accounting for the fact that the volume average of the internal stress in the whole body should be zero, Mori-Tanaka mean field theory[84] provides that

$$\boldsymbol{\hat{e} = -f (e - e^{**})} \quad (15)$$

where f is the volume fraction of inhomogeneities. From eq. (11) along with eqs. (13) and (15), fictitious eigenstrain e** for a certain volume fraction of equivalent inclusion is solved as

$$\boldsymbol{e^{**} = [(1-f) (C_f - C_m) \bullet (S - I) + C_f \bullet I]^{-1} \bullet C_f \bullet e_p} \quad (16)$$

where **I** is the identity tensor. Residual stress in FePd NWs, $\boldsymbol{\sigma}$, is then calculated from

$$\boldsymbol{\sigma} = (1 - f) \, \mathbf{C_m} \bullet (\mathbf{S} - \mathbf{I}) \bullet \mathbf{e^{**}} \quad (17)$$

The material constants for the residual stress calculation of Fe-Pd embedded in alumina are listed in Table 1. The volume fraction of FePd NWs $\mathbf{f = 0.028}$

Table 1. Thermo-mechanical properties of FePd and alumina

Material	E [GPa]	G [GPa]	ν	α (CTE)[1/°C]
$Fe_{70}Pd_{30}$	90	32	0.4	30 x 10^{-6}
Alumina	400	163	0.23	8 x 10^{-6}

The residual stress in FePd NWs in alumina with $\Delta T = -800°C$ are given in Table 2 and in Figure 4 where the effects of volume fraction of FePd NWs (f) are plotted.

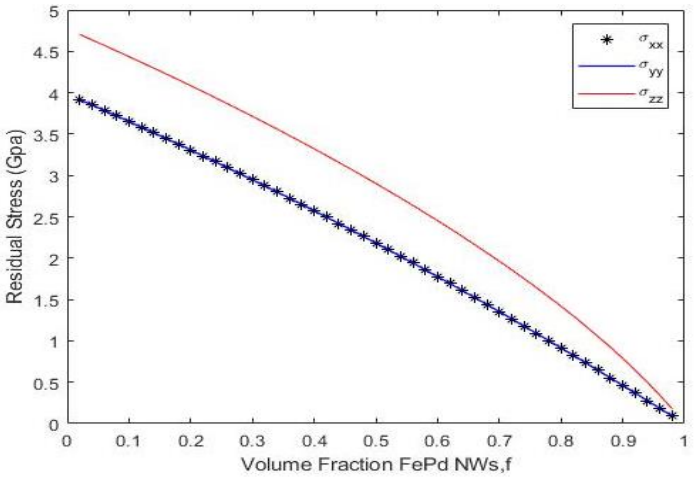

Figure 4: Residual stresses. FePd NWs residual stress prediction for multiple vs. volume fraction of NWs (f), predicted by Eshelby's model using Mori Tanaka mean field theory.

Table 2: Residual stress predicted for FePd NWs for f=0.028.

Residual Stress Components	Stress values (GPa)
σ_{xx}	3.8916
σ_{yy}	3.8916
σ_{zz}	4.6785

In Figure 4 and Table 1, the cross-section of cylindrical long fiber is on the xy-plane and the fiber longitudinal direction is along the z-direction defined.

The equivalent stress σ_{eqv} (Von Mises stress, σ_{MV}) is calculated from Table 2 as

$$\sigma_{eqv} = \sigma_{MV} = | \sigma_{zz} - \sigma_{xx} | = 4.6785 \text{ GPa} - 3.8916 \text{ GPa} = 787 \text{ MPa} \quad (18)$$

2.3.3 Eshelby's model for helical inclusion of FePd NHs

The stress inside the ellipsoidal inclusion can be easily computed as in the case of FePd NWs and it is uniform inside the ellipsoidal inclusion for uniform eigenstrain[85], [86]. The residual stress in helical inclusions, however, cannot be obtained using the standard Eshelby's model. A new Eshelby's model for helical inclusion[87] involve a helix where the shape is not ellipsoidal. The new model is termed as Average Eshelby Tensors for Helix (AETH).

Accounting the temperature drop of quenching treatment, $\Delta T = -800$ [K], eigenstrain of helical inclusion becomes $\alpha_{11}^* = \alpha_{22}^* = \alpha_{33}^* = -0.0176$, therefore the residual stress of $Fe_{0.7}Pd_{0.3}$ nano-helix is amounted to be $\sigma_{11} = \sigma_{22} = 4.65,\ \sigma_{33} = 4.77,\ \sigma_{12} = 8.73 \times 10^{-6}, \sigma_{23} = 3.14 \times 10^{-3}, \sigma_{31} = -1.92 \times 10^{-4}$ [GPa], and corresponding equivalent stress yields

$$\sigma_{eqv} = 0.121 \text{ GPa} = 121 \text{ MPa} \quad (19)$$

Comparing the equivalent stress by Eshelby's model in FePd NWs expressed by eq. (18) and that by FePd NHs expressed by eq. (19), we can conclude that eq. (18) gives us the upper bound of the residual stress while eq. (19) gives us the lower bound. It is noted that the Eshelby's model for the residual stress of eq. (18) is based on the assumption of FePd NWs embedded in alumina matrix while that of eq. (19) is based on the assumption of a single FePd NH embedded in infinite alumina matrix. We speculate that the real residual stress in FePd NWs and NHs lies between these two cases. To study this stress relaxation, we considered dislocation punching, shown below.

The difference in residual stress estimates between AETH by eq. (18) and standard Eshelby's model by eq. (19) reflects shape-dependent elastic field of NHs and NWs surrounded by alumina. Although distribution of local stress for NHs is magnified on helical cross-section,

which is cancelled by average treatment. In this sense, upper bound of residual stress is given by a longitudinal straight cylinder whereas lower bound is defined by AETH.

2.3.4 Stress relaxation by dislocation punching

Taya and co-workers developed the dislocation punching model for metal matrix composites when the fillers are assumed by spherical,[88] short fibers[89] and continuous fiber.[90] The dislocation punching model for Fe-Pd NWs embedded in alumina matrix is similar to the previous work,[90] however, the direction of dislocation motion would be different in current model. This new dislocation punching model for Fe-Pd NWs in alumina matrix is illustrated in Figure 5.

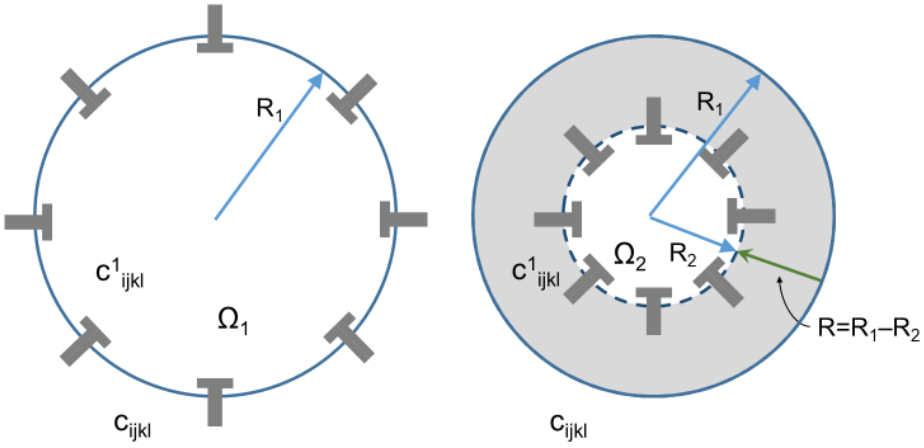

Figure 5. Dislocation punching model for FePd NWs (stiffness is C_{1ijkl}, radius is R_1) embedded in alumina matrix (C_{ijkl}) where edge dislocation loops at the FePd NW surface (a) are punched out inward (b) and dark donut area is the area swept by motions of the edge dislocation loops over the punching distance of R (= $R_1 - R_2$).

For the plastic work associated with the dislocation motion inside the domain Ω_1 with radius R_1 in Figure 5, the prescribed eigenstrain associated with CTE mismatch is canceled by

dislocations arranged at the boundary $|\Omega_1|$, while the region of the CTE mismatch is newly created at $|\Omega_2|$ by inward motion of the same number of dislocations with opposite sign. The resolved shear stress necessary for the glide motion of dislocations (friction stress) is assumed as τ_c, then the equivalent flow stress (normal stress, σ_y) is mentioned as $\sigma_y = 2\ \tau_c$.

Then the plastic work (or dissipation energy for the dislocation punching) per unit volume, W, is the product of σ_y and plastic strain, ε_p.

$$W = 1/V \int \sigma_y \varepsilon_p \, dV \quad (20)$$

where ε_p for the donut domain, $\Omega 1 - \Omega 2$, is given by[90]

$$\varepsilon_p = \alpha^* R_{12}/R_2 \quad (\text{for } R_2 < R < R_1) \quad (21)$$

By integration over the punched-out domain, $\Omega 1 - \Omega 2$, in cylindrical coordinates over $R_1 < R < R_2$, $0 < \theta < 2\pi$, $0 < z < L$, we obtain the energy dissipation of a single FePd NW per unit volume as

$$W=1/V \int \sigma_y \varepsilon_p \, R \, dRd\theta dz = 4\tau_c \alpha^* \ln(R_1/R_2) \quad (22)$$

where L is the dislocation line length of the NW. Since the present model assumes inward motion of dislocations, stress accumulation takes place inside Ω_2 unless the number of crystal dislocations would be decreased in view of geometrically necessary dislocations. This is marked difference from the previous work by Shibata et al.[90] However, if dislocation annihilation mechanism is operated by attractive dislocation interactions in NW, prescribed eigenstrain due to CTE mismatch can be vanished by existence of interfacial dislocations at $|\Omega_1|$. The residual stress associated with dislocation density is discussed in the following section.

2.3.5 Calculation of dislocation density and residual stress

Thermal residual stress of NWs embedded in alumina can be demonstrated by

geometrically necessary dislocations. Figure 6 represents arrangement of prismatic dislocation loops surrounding a NW, where misfit strains are assumed by burgers vector of dislocation loops. First, average strain associated with numbers of dislocation loops in considering volume V is

$$\langle \varepsilon_{ij} \rangle = \int \frac{b_i n_j}{V} dS \qquad (23)$$

where b_i is Burgers vector in i-th direction, n_j is outward normal vector of the plane on which the dislocation lies. Therefore, thermal mismatch strain of NW α_{ij} can be assumed by prismatic loops on the plane normal to longitudinal and transverse directions, N_L and N_T:

$$\langle \alpha_{11}^* \rangle = \langle \alpha_{22}^* \rangle \cong N_L \frac{b_1 2RL}{\pi\ R^2 L} = N_L \frac{2b_1}{\pi\ \mathrm{R}} \qquad (24)$$

$$\langle \alpha_{33}^* \rangle \cong N_T \frac{b_3 2\,\pi\, R}{\pi\ R^2 L} = N_T \frac{b_3}{\mathrm{L}} \qquad (25)$$

where R and L is radius and length of NW, respectively. CTE mismatch strain, α*, is the prescribed eigenstrain defined by eq. (14), i.e., $\boldsymbol{\alpha^* = e_p}$, so relationship of $\alpha^* = \langle \alpha_{11}^* \rangle = \langle \alpha_{22}^* \rangle = \langle \alpha_{33}^* \rangle$ holds when dilatational eigenstrain is assumed for CTE mismatch.

Since dislocation density is defined as the total length of dislocation in NW, average dislocation density, $\langle \rho \rangle$, would be

$$\langle \rho \rangle = \int_L \frac{dl}{V} = \rho_1 + \rho_2 + \rho_3 \qquad (26)$$

with

$$\rho_1 = \rho_2 \cong N_L \frac{2L}{\pi\ R^2 L} = \frac{\langle \alpha_{11}^* \rangle}{bR} \qquad (27)$$

$$\rho_3 \cong N_T \frac{2\,\pi\ \mathrm{R}}{\pi\ R^2 L} = \frac{2\langle \alpha_{33}^* \rangle}{bR} \qquad (28)$$

where ρ_i is dislocation density on the plane normal to x_i .

Taking into account that the stress necessary for the dislocation motion is proportionally changed with the square root of dislocation density, increase in the flow stress, or equivalently, the residual stress as a result of CTE mismatch that remains in the FePd NWs , σ_{CTE} is given by

$$\sigma_{\mathrm{CTE}} = c\mu b\sqrt{\langle\rho\rangle} = \mu\sqrt{\langle\alpha_{11}^{*}\rangle\frac{b}{R}} \qquad (29)$$

where c is a constant assumed as 0.5, μ is shear modulus of FePd, b is magnitude of Burgers vector of FePd (a/2[110], a = 0.3750 nm)

By substituting shear modulus, magnitude of Burgers vector, thermal mismatch and radius of NW for fcc-$Fe_{70}Pd_{30}$ (μ= 32.13 GPa, b = 0.1875 nm, α* = – 0.0176, 30 nm) into eq.(31), σ_{CTE} is amounted to be

$$\sigma_{\mathrm{CTE}} = 336\ \mathrm{MPa}\ ,\ (\ \langle\rho\rangle = 3.128 * 10^{15}\ \mathrm{m}^{-2}\ ). \qquad (30)$$

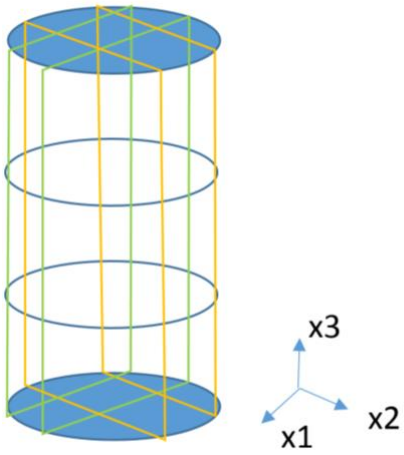

Figure 6. Arrangement of prismatic dislocation loops on FePd NW surrounded by alumina matrix. Rectangular loops are lying on the plane normal to x1 and x2 direction, circular loops on the plane normal to x3 direction.

Comparing the residual stress of NW predicted by dislocation model to that by Eshelby's model, the stress value given by Eshelby's model in eq. (18) is greater than that by the dislocation model, thus upper bound of the residual stress of NW is given by Eshelby's model,

while certain relaxation state is demonstrated by dislocation model in eq.(30).

On the other hand, the Equivalent stress (or Von-Mises stress), σ_{VM}, predicted by the average Eshelby's tensor model for helical inclusion (AETH)[87] is

$$\sigma_{VM} = 121 \text{ MPa} \quad (31)$$

Comparing the residual stress of NW in eq. (30) to that of NH in eq. (31), residual stress of NH shows lower magnitude than that predicted by the standard Eshelby's model while higher than the residual dislocation models for NW. It should be noted that, basically, residual stress of cylinder predicted by Eshelby tensor shows higher magnitude than that of helix predicted by average Eshelby tensor as discussed in previous work.[87] Although the helical turns essentially reduces the constraint effect of the inclusion embedded in matrix phase, stress averaged by cross-section of helix is twice as large as that obtained by AETH with factor of 2.5 σ_{VM}, where σ_{VM} is given by eq. (31) (see Table 2 in [87]). Therefore, the average stress on the cross section of NH is estimated to be 309 MPa which is consistent with dislocation punching model as shown in Table 3. Moreover, since local stress concentration on the cross section helix is ranging from 1.5 to 6 σ_{VM} (see Figure 9 in [87]), the maximum stress on the cross section of NH is reduced to be 727 MPa. Hence, internal stress of NW and NH predicted by Eshelby's models are mutually consistent in maximum stress value.

Recalling the fact that internal stress field is exactly demonstrated by geometrically necessary dislocations (GNDs) through the line integration,[91] present dislocation model does not meet the maximum stress value of NW. This is because misfit strain in eq.(24) is assumed by dislocation density, and the stress field caused by exact arrangement of GNDs is not taken into account. In this point of view, the dislocation model provides intermediate stress value of residual stress, which reflects the relaxation stress state under the certain dislocation density.

Table 3 shows the summary of residual stress predicted by the three models.

Table 3. Summary of residual stress predicted by three models: Eshelby's model, Average Eshelby Tensor for Helix (AETH),[87] and dislocation punching model where Burgers vector is used, b = 0.265 nm. The Eshelby's model and dislocation punching model are based on assumption of FePd nanomaterial is continuous nano-cylinder (or nanowires) while AETH model is based on helical shaped geometry.

Model	σ_{rr}	σ_{zz}	σ_{VM}
Eshelby's model (Table 2)	3.892 GPa	4.679 GPa	787 MPa
AETH, eq.(20)	4.65 GPa	4.77 GPa	121 MPa (total avg.) 309 MPa (cross-sec. avg.) 727 MPa (local max.)
Dislocation punching, Based on eq. (39)	NA	NA	336 MPa

2.5 Procedures

2.5.1 Synthesis of porous anodic alumina template

In order to produce FePd nanowires with precise alloy composition and uniform shape, they are processed in a template with controllable pore diameter. A porous anodic alumina (PAA) or anodic aluminum oxide (AAO) membrane is synthesized by two-step anodization process.[92] A 0.13-mm thick foil of aluminum (99.9995%) is degreased in acetone to wash off residual organic material, then electrochemically polished in a solution of 95 vol% H_3PO_4 (85 wt%), 5 vol% H_2SO_4 (95 wt%), and 20g/L CrO_3 for 30 seconds at 85ºC and with 20 V applied. The surface is further cleaned by removing any oxide layer with 3.5 vol% H_3PO_4 and 45g/L CrO_3 at 95ºC for 3 minutes. The first anodization, which creates an oxide layer on the aluminum as well as indentations at

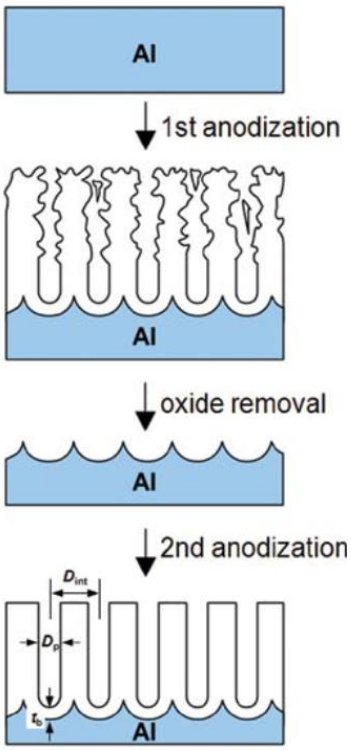

Figure 7: Schematic illustration for two-step anodization of aluminum. [175]

the pore sites from aluminum expansion, is performed with 0.3 M oxalic acid for 10 hours at 15ºC and with 40 V applied.[93] This oxide layer is then completely removed, leaving behind only the self-ordered pore bases, with 6 wt% phosphoric acid and 1.8 wt% chromic acid for 14 hours at 60ºC. A second anodization with oxalic acid in the same conditions for 10 minutes forms cleaner, more ordered pores as a thin layer of PAA. A third anodization step with 0.2 M H_3PO_4 at 15ºC and with 40 V applied for 10 minutes etches some of the thickness of the pore walls and bottom barrier layers; such thinning can be continued with additional exposure to H_3PO_4. 20 minutes in 5% H_3PO_4 will bring the pore diameters to approximately 50 nm and interpore distance to approximately 100 nm. The foil is rinsed with DI water after each step. This process produces a thin but brittle layer of PAA on the aluminum foil.

2.5.2 Nanowire electrodeposition

After formation of the PAA template, gold is sputtered (Lesker, Lab 18 Sputter) on top to a thickness of 200 nm to produce a conductive anode layer against the pores. The template is then cut into pieces approximately 1 cm x 0.5 cm and bonded to a glass slide support using a 60-µm thick layer of conductive silver epoxy (Ted Pella, cured at 120ºC for 30 min), with the gold side in contact with the epoxy and edges covered with nail polish to prevent leakage and short-circuiting of deposition current. The thicker aluminum foil layer on the backside is reacted with 1 M $CuCl_2$ and washed away by hand, leaving alumina template with a barrier layer approximately 50 µm thick. This is etched away with 5% phosphoric acid for 140 minutes to reveal the pores so the electrolyte can enter the template.

Samples were wetted in water and electrolyte for up to 48 hours prior to electrodeposition. The wetting ensures that the electrolyte ions are present at the cathode surface

and that the initial electrodeposition happens on the entire area of Au in the pore rather than only the uppermost available reaction sites.[94] Electrochemical deposition occurs with the gold PAA electrode and Pt foil counterelectrode with an Ag/AgCl(3M KCl) reference electrode (Metrohm), positioned vertically in a 50 mL beaker submerged in the electrolyte, with a 2 cm distance between the working electrodes; a stir bar agitates at 300 rpm. An electrolyte of 0.1 M $Fe_2(SO_4)_3$, 0.01 M $Pd(NH_3)_2Cl_2$, 0.2625 M $C_7H_6O_6S$, 0.3 M $(NH_4)_2SO_4$, with pH adjusted to 5 by H_2SO_4 is used.[62] Alternating potentiostatic and galvanostatic pulses are applied (Metrohm Autolab) so that as the alloy forms in the pore the concentration gradient is reduced, the pH is constant, and evolved gas does not block the pores.[62] Potential E_1 is applied for t_1=15 seconds, followed by a resting cycle of t_2=30 seconds with I_2=0 A. E_1 was in the range from –1.02 V to –1.35 V, as measured against an Ag/AgCl/3M KCl reference electrode at room temperature.

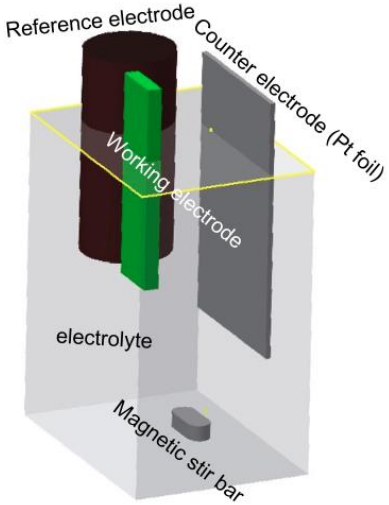

Figure 8: Schematic of electrodeposition set-up

To form nanohelices rather than nanowires, the pores are filled with a mold: Here sol-gel porous SiO_2 produces a template within the pores, beginning with hydrolysis using tetraethyl orthosilicate, HCl, and ethanol, gelled with triblock copolymer Pluronic P123. This solution is dip-coated into the pores of the PAA template which is then aged for 24 hours in 70% relative humidity at 25°C in an environment chamber, followed by calcination at 500ºC for 3 hours to remove the polymer.[95] The helix-shaped silica pore is formed by self-assembly of the polymer–SiO_2 complex, as the nanoconfinement by the narrow alumina pores induces the polymer to take a particular shape to minimize free energy. Calcination evaporates the residual

ethanol and TEOS to leave an open pore behind. The resultant mesostructure formed by the nanoconfinement may take such shapes as rods, donuts, helices, or double helices, depending on the degree of confinement, described as D/L_0, or the ratio of the alumina hole diameter to the period of the block copolymer (in bulk phase). The target D/L_0 to obtain helical pores is 2.37, based on experimental results, though simulated results showed singles helices at approximately 1.5.[96] Different polymer blends can adjust L_0 so the desired pore diameter may be adjusted to obtain a single helix-forming degree of confinement.

2.5.3 Nanowire synthesis in commercial template

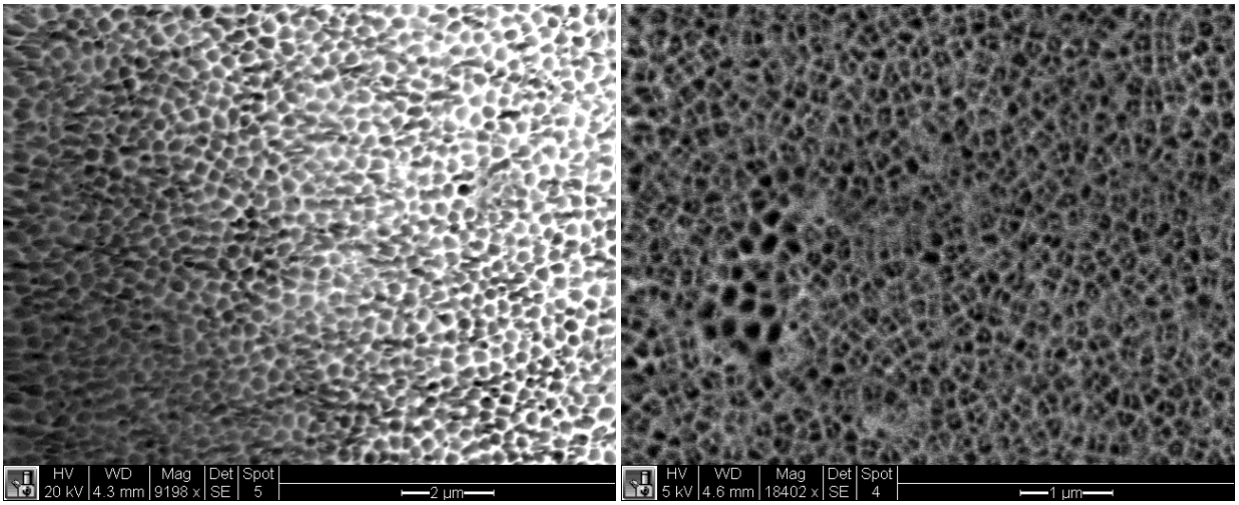

Figure 9: Top (left) and bottom (right) of commercial PAA template.

The PAA template from a commercial manufacturer may alternatively be used.[72] PAA membranes (Whatman Anodisc) with diameter 25 mm and pore size 200 nm were sputtered with 600 nm Au on the bottom side as an electrode. As shown in Figure 9, the bottom side of the template has an additional stability layer on it, while the top has open pores and is exposed to the electrolyte. Conductive copper tape was adhered to the gold side of the membrane to be a conduit to the Autolab power source, and the gold side is coated in protective nail polish before

dipping into the electrolyte. As explained later, gold nanowires are initially deposited from a solution of 20 mM $KAu(CN)_2$ (Sigma Aldrich) and 0.25 MNa_2CO_3 (Sigma Aldrich) at –1.2 V for 300 s.[97] FePd is then electrodeposited using the same plating bath as before and the pulse-plating method alternating galvanostatic and potentiostatic phases. Templates are wetted in electrolyte for 30 min before electrodeposition.

2.5.4 Annealing of nanowires

The nanowires are annealed in a tube furnace (Barnstead Thermolyne 21100) while still embedded in the alumina template. To minimize contamination and oxidation, samples are sealed in a glass ampule with an Ar/5% H_2 environment (or vacuum environment), also containing titanium sponge as a chemical getter. The ampule is placed inside the furnace near the internal thermocouple and it is heated to 830ºC for 5 minutes to reach homogenized crystal structure. To lock in the high-temperature γ structure, the ampules are removed by tongs and placed in cold water, where the glass breaks and the nanowires are quenched. Annealing samples in a large quartz tube slid into the furnace was also employed, but this required a slow cooling before samples could be accessed and quenched.

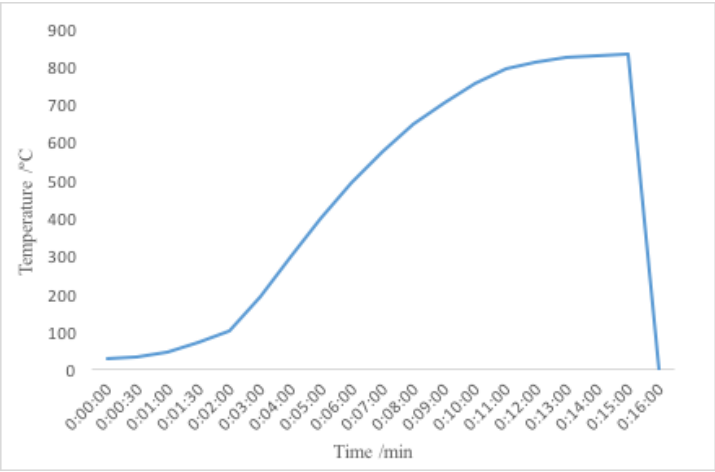

Figure 10. Representative annealing temperature pattern reaching 830°C in furnace, followed by quenching in ice water

2.5.5 Synthesis of FePd nanoparticles

$Fe_{70}Pd_{30}$ nanoparticles (NPs) were synthesized as nanosized FSMA materials that are a model for nanowires. Following the polyol method,[98] 63 mg (0.21 mmol) palladium acetylacetonate (II) ($Pd(acac)_2$), 1.1 mL PEG-600, 0.16 mL (0.5 mmol) oleic acid, and 0.16 mL (0.5 mmol) oleylamine were mixed in 20 ml diphenyl ether and heated to 140°C under argon. 40 µL (0.30 mmol) iron pentacarbonyl ($Fe(CO)_5$) was injected before heating further to 260°C for 30 minutes. The resulting reaction product was allowed to cool before purification and isolation by rinsing with ethanol and centrifugation.

The FePd NPs were annealed to 770°C for 5 minutes in argon with 5% hydrogen.

2.5.6 Surface modification of nanoparticles

Nanoparticles (Fe nanoparticles [Aldrich, 40-60 nm diameter] and synthesized FePd nanoparticles) were ozonated to allow for later surface coating with PEG, silane, or other ligands. The ozonation was performed in a round-bottom flask containing 50 mL DI water and the nanoparticles, connected to a reflux condenser. The flask was placed in a sand bath heated by a hot plate at 400ºC. When the water temperature reached 100ºC, oxygen was flowed through an ozonator (A2Z Ozone, Lab Benchtop) at 3 NL/min producing a flow with 6% ozone concentration. The ozonation time was approximately one minute to achieve an oxide shell thickness of 2-3 nm, and then the oxygen cylinder was closed, and the flask contents were poured into a beaker, which was placed on a magnet to collect the nanoparticles. The supernatant is removed, and nanoparticles are briefly sonicated in and magnetically collected from ethanol four times to clean them.

2.5.7 Characterization methods

Before electrodeposition the PAA templates were examined under SEM (FEI Sirion XL30) to ensure pores formed correctly with appropriate size and spacing and without excessive debris.

Nanoparticles were measured by a vibrating sample magnetometer (Quantum Design VersaLab) following ozonation to determine the samples' magnetic moment and magnetization. These values were compared to known measurements for pure chemicals to estimate the composition and, assuming an oxide layer forms evenly on the outside, the oxide shell thickness.

Nanowires were examined with SEM and energy-dispersive X-ray spectroscopy for morphology and size and to measure atomic composition of the synthesized FePd. EDS analysis was conducted with 20 kV accelerating voltage for 300,000 counts. The overvoltage ratio for both Fe and Pd was kept >2 as recommended for EDS analysis.

X-ray diffraction can determine the crystal structure and geometry of the NRs. Preliminary XRD spectra were measured at the UW Molecular Analysis Facility with a Bruker D8 Discover Microfocus (Cu-Kα source), while higher-energy data was measured with 1D MYTHEN detectors of beamline BL02B2 of SPring-8 synchrotron.[99]

2.6 Results and discussion

2.6.1 Surface modification of representative nanoparticles

Ozonation of Fe nanoparticles resulted in the formation of iron oxide on the surface of the nanoparticles, with calculated thicknesses shown in Table 4. Even the unozonated nanoparticles had an oxide thickness of 2–3 nm, indicating they may have been oxidized in the air. As the shell thickness does not need to be any larger than 3 nm, the optimal ozonation time

may be less than 1 minute or not at all, though this may be different for FePd NWs, which have a greater surface area-to-volume ratio and a lower fraction of Fe atoms to oxidize. Ozonation leads to the possibility of surface silanization, as the silane coupling reaction occurs with a metal oxide. An SBSi linker can be added to solution with ozonated NRs, then analyzed by FT-IR spectroscopy to determine the presence of SBSi on the final product. Our group demonstrated that $Fe_{70}Pd_{30}$ nanoparticles, once oxidized, could be coated with zwitterionic SBSi linker, which stabilizes a hydrophilic surface and prevents fouling by proteins. This surface modification was more biocompatible with breast cancer cells than bare FePd nanoparticles.[100]

Table 4: Oxide shell produced from each ozonation

NP diameter (nm)	**Ozonation time (mm:ss)**	**Magnetization (emu/g)**	**Oxide shell thickness (nm)**
50	00:00	192.0	3.03
50	00:00	165.8	2.75
40	00:00	197.0	2.14
40	00:31	124.4	4.91
50	01:12	122.2	6.35
50	05:00	98.2	9.15

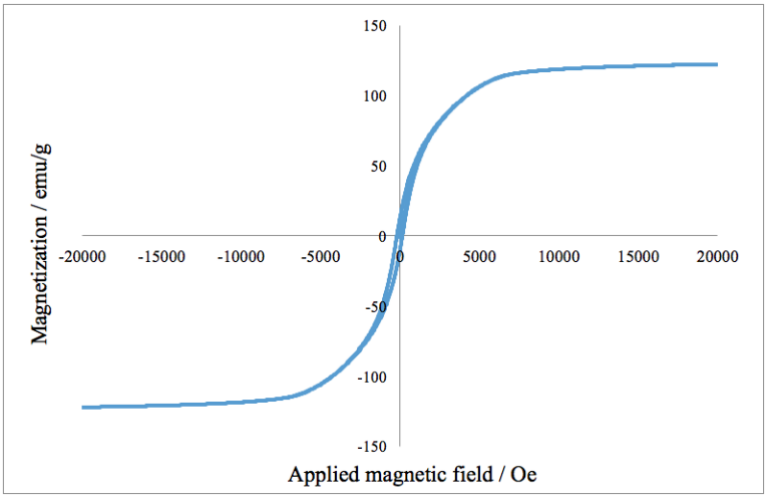

Figure 11: Magnetization vs. magnetic field (M–H curve) of Fe nanoparticles with average diameter of 50 nm, ozonated for 1 minute, 12 seconds.

2.6.2 PAA synthesis

From the PAA synthesis process we were able to fabricate a template in anodic aluminum oxide. The pores have diameters of approximately 50 nm and are spaced approximately *a*=100 nm from center to center and are arranged in hexagonal pattern. Duration of the second anodization step controls the PAA layer thickness. An angled view in the SEM along cracks made in the PAA shows the pores are between 500 nm and 1 µm deep. Spacing between pores is determined in the first anodization step, controlled by temperature, applied voltage, and anodization time. The most determinative of these is the voltage, which influences the volume expansion of aluminum during oxidation. Mechanical stress between metal and oxide promote formation of the hexagonal pore arrays due to repulsive forces between pores.[101] One sixth of each of three pores make up a unit cell of an equilateral triangle, which has an area of $A = \frac{\sqrt{3}}{4}a^2 = 4330\ \text{nm}^2$.

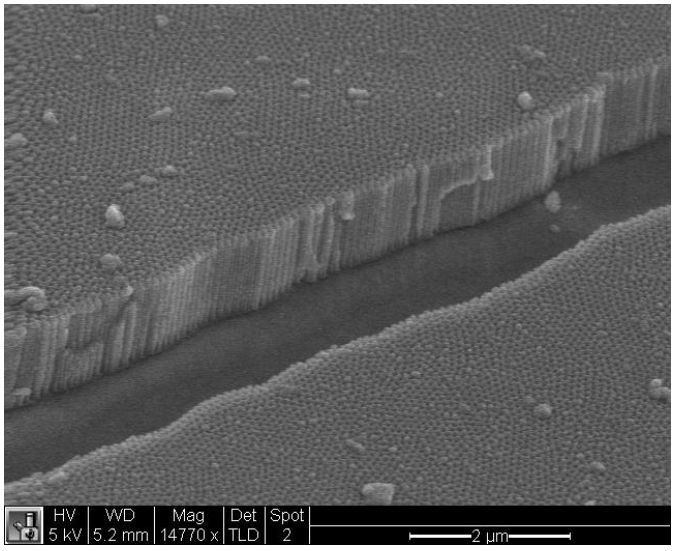

Figure 12: SEM image of PAA template showing hexagonal pore arrangement and pore depth

The pore density of synthesized PAA is therefore $1.15 \cdot 10_{10}$ holes/cm_2, with each pore having an area of 1963 nm_2. Under an assumption that each pore is 100% filled by deposition,

the volume of a single 1-μm-long rod is $V = \pi r^2 h = 1.96 \cdot 10^6$ nm^3, with a mass of $1.8 \cdot 10^{-14}$ g for $Fe_{70}Pd_{30}$ (ρ=9.12 g/cm^3, assuming the volumes of Fe and Pd are addable when forming an alloy). In a 0.5-cm^2 template, the optimal total volume of nanowires yielded is 1.13×10^{-5} cm^3 with a mass of 103 μg. The pores however are not synthesized in a perfect pattern unobstructed across the whole template, part of the template is covered by nail polish, and the average filling rate is less than 100%.

Following PAA synthesis, the template was sputtered with gold: 200 nm for homemade templates and 600 nm for the thicker commercial membranes.

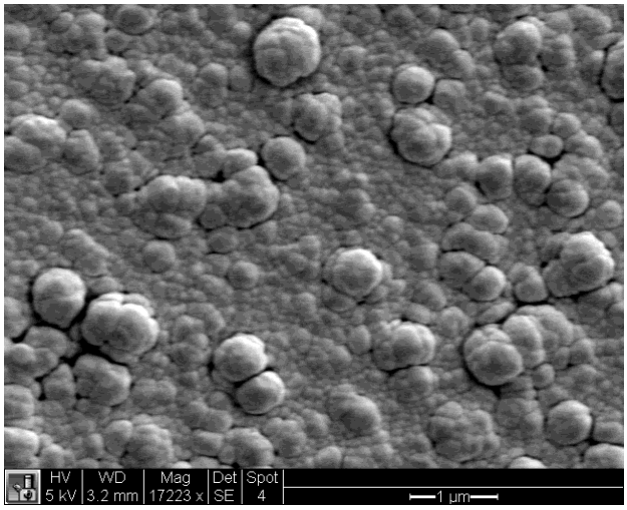

Figure 13: Morphology of 600 nm Au sputtered on commercial PAA template with pores completely covered

2.6.3 Electrodeposition of FePd in synthesized PAA templates

FePd was electrodeposited from the electrolyte into the pores of the PAA template prepared on substrate. SEM–EDS analysis showed that most samples had some deposition of FePd, though some deposition occurred at uncovered sites that were along the path of least resistance rather than in the pores.

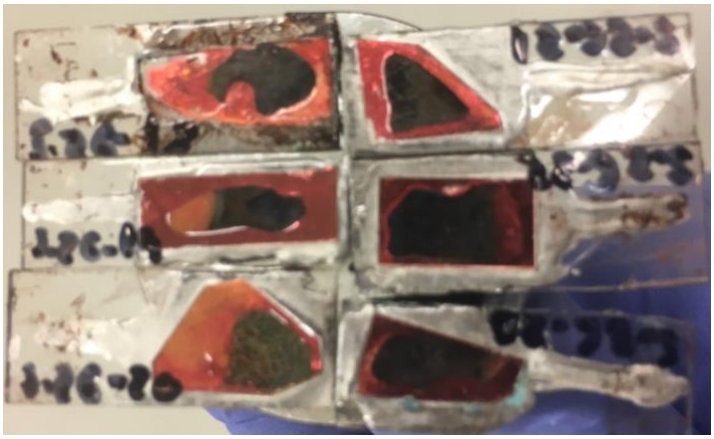

Figure 14: Templates after deposition showing darkened areas of nanowires

We sought to optimize a consistent deposition of FePd into the alumina pores with the desired composition of 70% Fe and 30% Pd, but each template was slightly different, and the application of given voltages did not produce identical atomic composition. FePd was electrodeposited at voltages from –1.05 to –1.35 V, and some nanowires subsequently had a Fe percentage as low as 10% to as high as 80%. The 70% Fe was obtained in the –1.25 to –1.32 V range, though there was not perfectly consistent replication when deposited under the same conditions. Among samples deposited at –1.28 V the average Fe content was 70.2% with a standard deviation of 8.6%, while the at –1.30 V it was 67.8% ± 5.7%. This conforms with work by Rozman, whose optimal $Fe_{70}Pd_{30}$ nanowires were found at –1.27 to –1.325 V;[72] these data only had one deposited sample at each voltage, however, except at –1.325. The individual samples have narrower distributions, with measurements at different points on the template having a standard deviation of less than 4%. To provide a check on the deposition process, voltage was also applied to gold-sputtered glass substrates in the electrolyte. Across a voltage range of –1.18 to –1.35 V, the Fe percentage was consistently at 80% or higher, consistently greater than the Fe percentage in FePd deposited in the alumina templates. This may be due to exposure to Au in bulk, rather than the smaller exposed areas at the bottom of the alumina pores;

the EDS measurements of nanowires were taken at the exposed top of the template, so there may be a spatial variance from the bottom to the top of the pores.

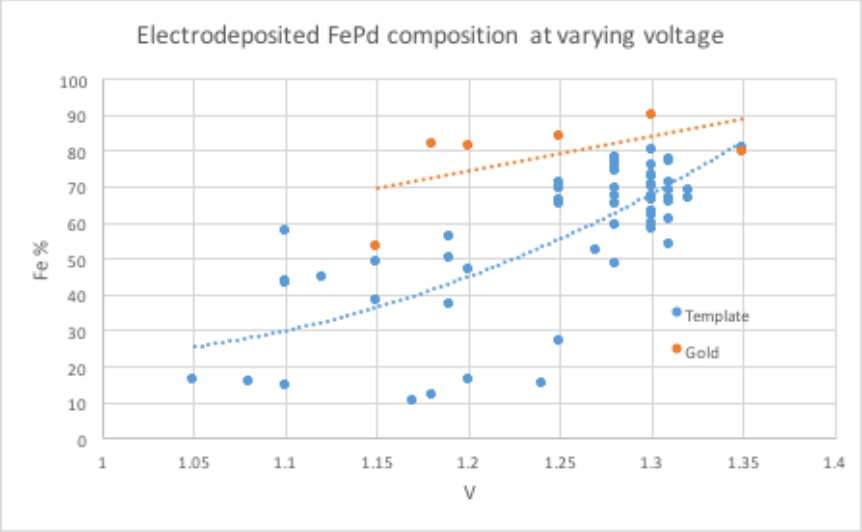

Figure 15: Relationship between applied electrodeposition voltage and resulting Fe content

The morphology of the nanowires was examined from the top of the template by SEM. Successfully deposited NRs appeared as gray spots in the pores, as shown in Figure 16. On the left side of the image, NRs slightly underfill the pores, while in the right side the NRs appear to slightly overfill the pores but do not merge together. NRs in this sample had composition $Fe_{70\pm3.6}Pd_{30\pm3.6}$. Also shown are cauliflower- or popcorn-shaped deposited, which are localized overgrowths of FePd; NRs in certain pores may have deposited faster and when above the surface of the template acted a preferential deposition sites due to their size and shape. In some templates they covered a substantial portion of the surface area, with the surrounding pores not necessarily filled with FePd. The extent of this surface deposition can be minimized by limiting the number of electrodeposition pulses to 10.

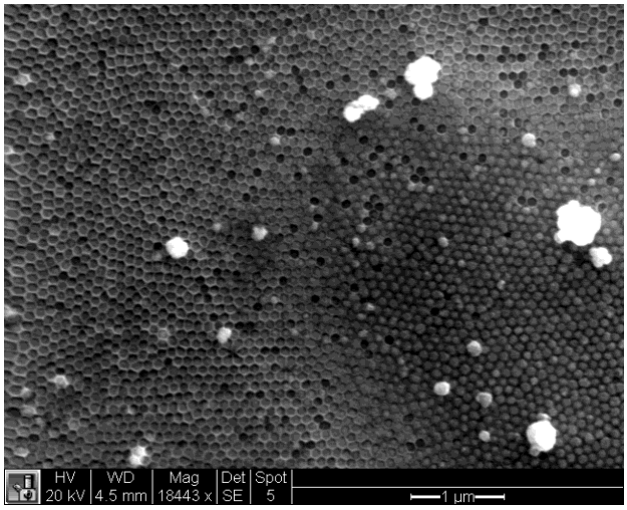

Figure 16: $Fe_{70}Pd_{30}$ NRs deposited in homemade alumina template

2.6.4 Electrodeposition of FePd in commercial PAA templates

Fabrication of FePd nanowires in commercial PAA templates would show greater success for consistent morphology. The pulse-plating electrodeposition method however did not initially result in the production of nanowires, with FePd largely undetected in the pores. Initially an alternate electrolyte using differently complexed metals was made using a recipe from Rozman using 300mM $FeCl_3$, 3mM $PdCl_2$, and 0.4M $(NH_4)_2C_6H_6O_7$, with NH_4OH(aq) bringing the pH to 9.[72] Voltage of E_1 = –1.25, –1.28, and –1.30 V was applied to templates with pulses of t_1=30 seconds and t_2=50 seconds, over ten cycles. There were no changes in the appearance of the templates, nor did EDS provide evidence of FePd deposition in the pores. Electrodeposition using the prior electrolyte as described above at –1.25 V resulted in a reddish color on the templates, and EDS showed one sample with nanowires with composition $Fe_{80}Pd_{20}$ in at least some areas of the template, deposition was likewise incomplete and inconsistent.

With the larger pore size, it was likely the sputtering of a 200 nm gold layer resulted in some gold depositing within the pore and did not fully cover the back opening. This meant that the electroplating would uncontrollably occur on the underside of the sputtered layer. The

sputtered gold reaching into the walls of the pore also meant that FePd could preferentially deposit on those higher-up segments along the pore walls rather than at the full depth, potentially forming a tubular shape with a void at the bottom.[102] A thicker 600 nm gold layer was sputtered to ensure full covering but FePd nanowires could still not be produced in the template.

To ensure growth of nanowires and repeatable results, an even surface at the base of the pores is necessary. Therefore, subsequent to Au sputtering and covering the backside with nail polish, short Au nanowires were electrodeposited at the base. A pulse-deposition method of 50 mM $KAu(CN)_2$ (98%, Sigma Aldrich) alternating between 0.6 V and –0.5 V[103] failed to produce any gold deposits. Following another recipe, Au was deposited from the top side in a solution of 20 mM $KAu(CN)_2$ and 0.25 M Na_2CO_3 at –1.2 V.[97] After 30 min of wetting in solution to ensure Au ions in electrolyte are present at the cathode, deposition for 300 s produces base Au nanowires of about 1 μm in length, as desired. This method was effective with Whatman Anodisc templates, but it did not work with membranes from InRedox (pore diameter 80 nm), which did not have the stability layer.

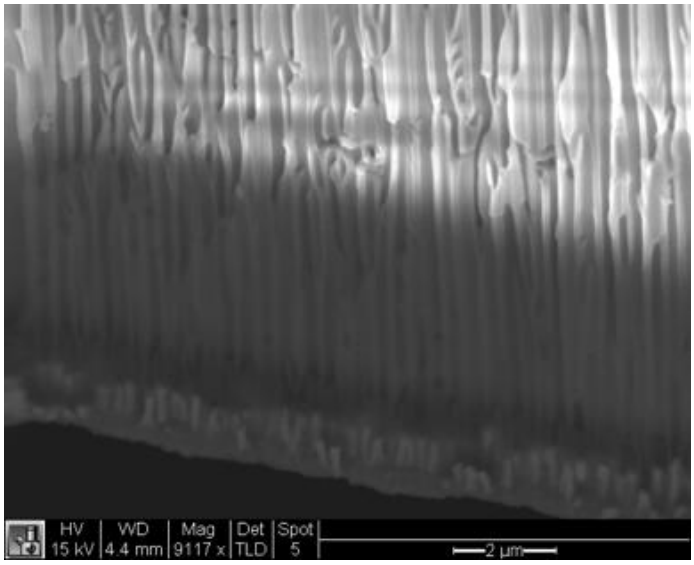

Figure 17. Template nanopores with Au nanowires at base

With the larger holes and longer pores, potentiostatic and galvanostatic phases were extended to t_1=10 seconds and t_2=20 seconds to ensure sufficient diffusion and convection of Fe and Pd ions to the gold surface and H_2 away from the surface out of the pores. Use of the $Fe_2(SO_4)_3$ and $Pd(NH_3)_2Cl_2$ electrolyte successfully resulted in the deposition of FePd nanowires in the template pores. The longer pores however also requires a lower current to ensure nanowires are homogeneous, as the diffusion layer is thicker and limiting mass transport as the effect of forced convection is reduced.[94] The diffusion limiting current is inversely proportional to the nanopore length, and when the external current is larger than the limiting current, the electrode potential changes and reduction does not happen.[104] For the Anodisc template, the optimal deposition potential to produce $Fe_{70}Pd_{30}$ was found to be –1.03 to –1.04 V. Length of resulting nanowires could be tuned with the number of electrodeposition cycles, with a typical length of 2–3 μm with 40 pulses.

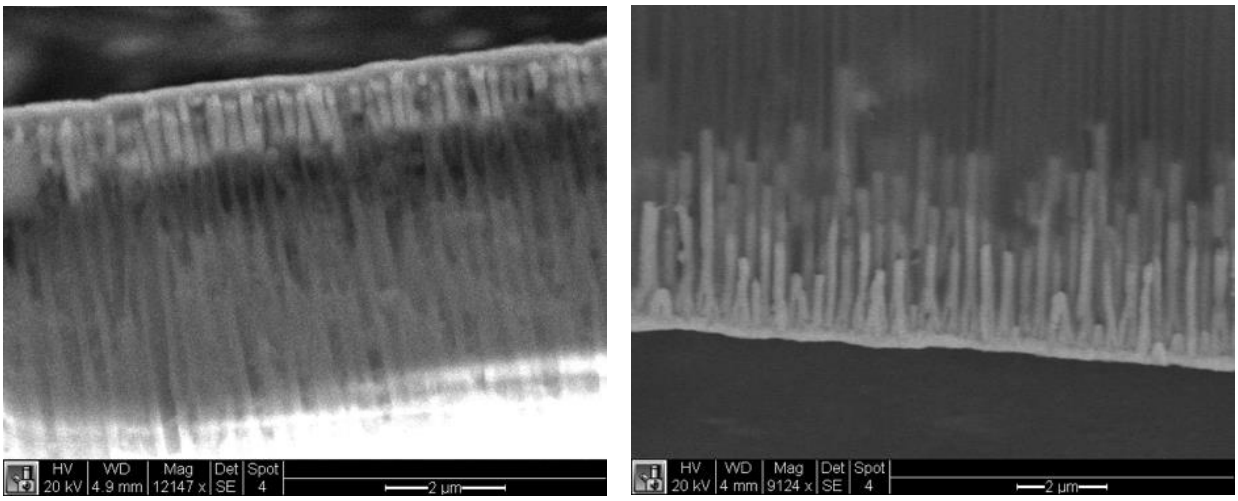

Figure 18. FePd nanowires electrodeposited on Au base

2.6.5 Extraction and annealing of nanowires

Nanowires can be isolated for TEM analysis by two methods. The first is to adhere tape (such as copper tape) to the surface of the sample and then rapidly pull off. If the attachment to

the adhesive is stronger than that to the silver epoxy, the alumina template and gold layers will be removed. Gold etchant will dissolve the gold, and the nanowires will be released from the template by weakening the tape adhesive with acetone and etching the alumina with phosphoric acid. The second is to scrape the template off the epoxy with a razor blade followed by etching.

Both of these methods however result in the destruction of the alumina template, and its thinness (~1 μm) makes it fragile and difficult to manipulate. Neither the tape nor silver epoxy can withstand the high temperature of annealing, so annealing the nanowires while still embedded in alumina in order to induce residual stress is not feasible with this method. One attempted alternative is to replace the silver epoxy with conductive silver paint, which is dissolvable in acetone. This however remains difficult to remove in its entirety without breaking the template; the unexposed paint underneath the template does not dissolve and a blade remains necessary to remove it.

Use of stand-alone alumina templates, which do not need to be adhered to glass for support and which can be wired to an electrode without an epoxy lead, is preferred. The as-purchased membranes, while still brittle, are substantially thicker (~60 μm) and wider (25 mm diameter), can be sputtered with gold and directly attached to the electrode clamp via copper tape. Following electrodeposition and removal of the gold layer by gold etchant, the nanowires can be directly annealed while embedded in the template.

Nanowires in alumina template were originally annealed under vacuum at 900°C for 20 minutes. Samples were sealed in glass ampules with a pressure of 0.00013 mbar and titanium sponge before placing the ampule inside the furnace. SEM analysis revealed that the template no longer contained nanowires, but nanoparticles, ranging in size from 75 nm to 250 nm in diameter. This may be attributed to Rayleigh instability, as perturbations in the metal cause

fragmentation from loss of thermal stability. Other types of metal nanowires have been observed to break into spheres at temperatures, even well below but related to their melting point, due to atomic surface diffusion.[105] The smaller the diameter of a nanowire, the greater the gradient of curvature, causing proportional diffusion of atoms to minimize surface energy.[106], [107]

The Rayleigh instability can be prevented by reducing annealing durations and temperatures. Subsequent anneals were performed at 830°C and for only 1 min. Ampules were also filled with Ar/5%H_2 gas as a reducing atmosphere, further limiting the possibility for oxidation. Nanowires then retained their shapes after annealing and quenching.

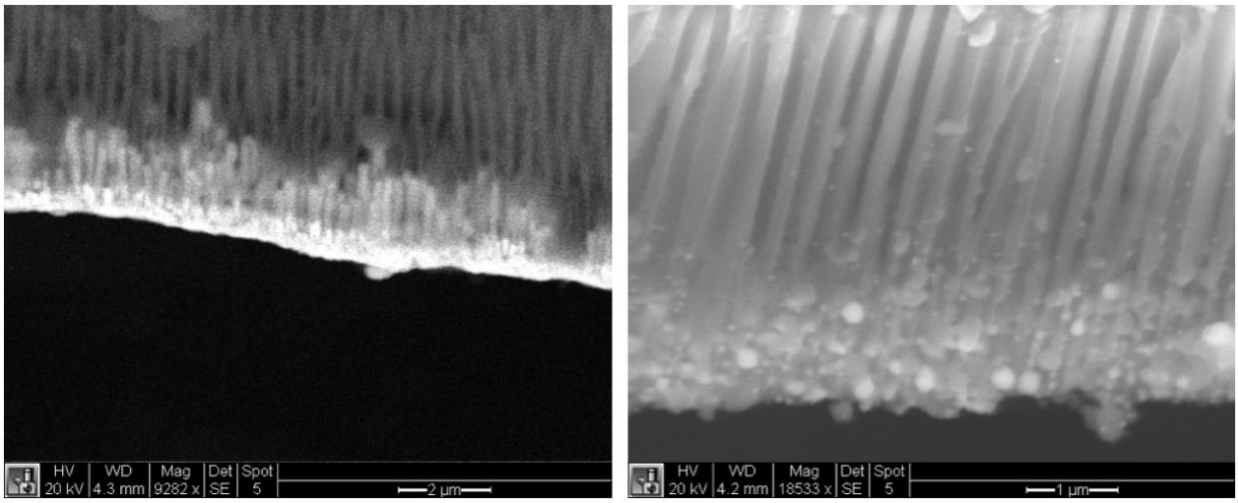

Figure 19. (Left) Electrodeposited FePd nanowires on Au base. (Right) Nanowires after annealing at 900°C in vacuum, having fractured into nanoparticles

2.6.6 Crystallography of FePd nanomaterials

To determine the martensite transformation temperature, X-ray diffraction spectra were measured using the high-energy beamline BL02B2 at SPring-8, Japan, which provided the functionality to record the sample spectra at low temperatures. Measurements were taken of FePd nanoparticles, nanowires, and nanohelices in 20-K increments, first cooling from room temperature (300 K) to 40 K, then 30 K, then warming from 40 K back to 300 K, to determine

the differences in phase shift characteristics of the materials with varying sizes. The synchrotron beam has a wavelength of 0.517 Å, whereas previously measured data and chemical libraries use a Cu source with wavelength 1.54 Å. To compare the two, the corresponding Cu wavelength to the synchrotron wavelength is calculated by determining the Cu XRD wavelength that produces the same scattering vector Q ([Å^{-1}]):

$$Q = \left(\frac{4\pi}{\lambda}\right)\sin\left(\frac{2\theta}{2}\right)$$

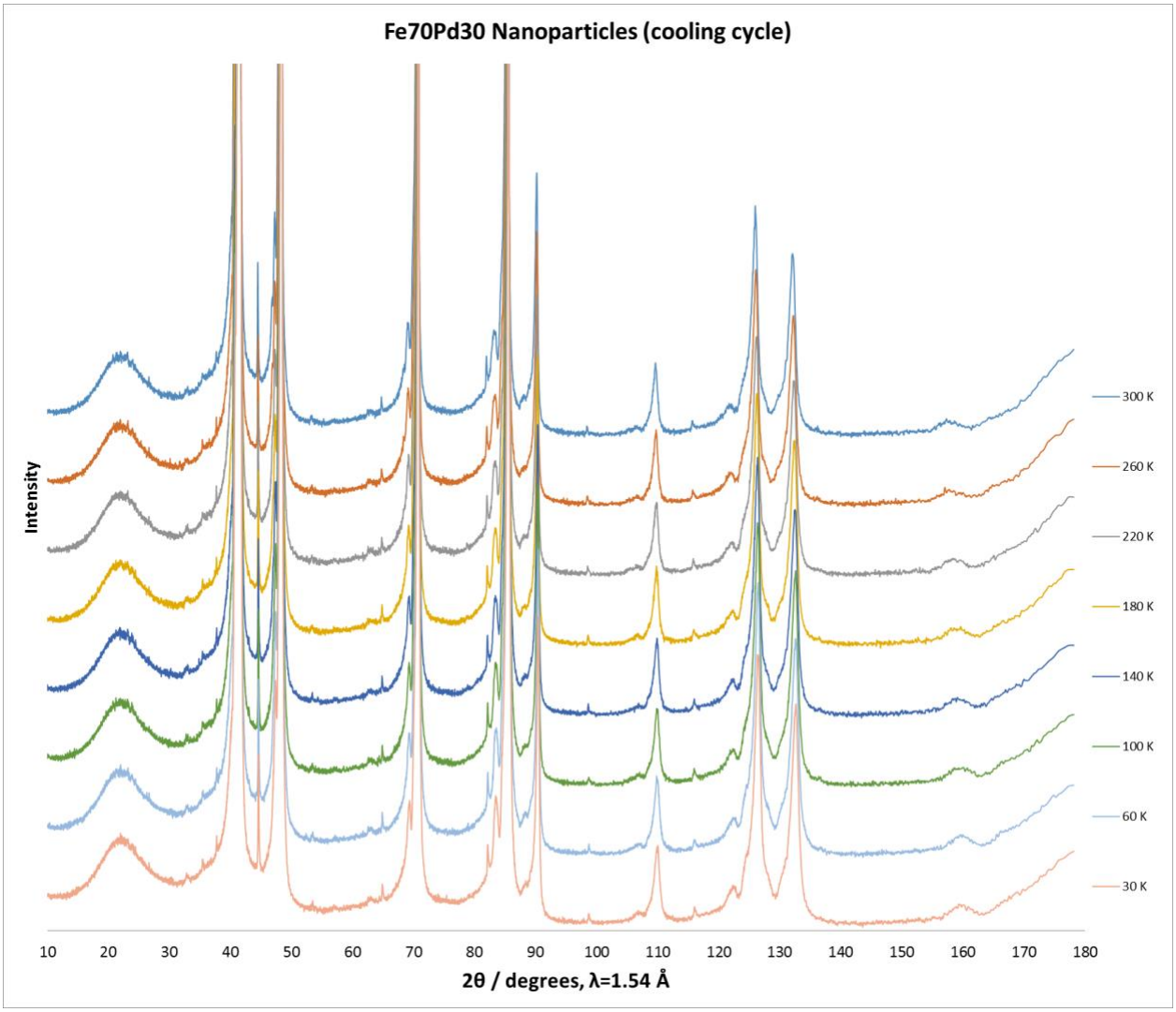

Figure 20: Synchrotron XRD spectra of FePd nanoparticles, as cooled from 300 K to 30 K

The XRD spectra for synthesized as-annealed $Fe_{70}Pd_{30}$ nanoparticles (Figure 20) had characteristic peaks that corresponded to disordered fcc (111) at $2\theta = 41.7°$, fcc (200) at 48.6°, fcc (220) at 71.1°, and fcc (311) at 85.9°. As the temperature of the nanoparticles decreased, there was no change in the spectrum peaks, indicating that no martensite phase shift occurred. This can be likely attributed to the peak at 44.5°, indicting a small presence of precipitates of the α-Fe body-centered cubic phase. This is corroborated by smaller peaks for bcc (200) at 65° and bcc (211) at 82°. The nanoparticles' composition was likely poor in palladium as indicated by the binary alloy phase diagram.[66]

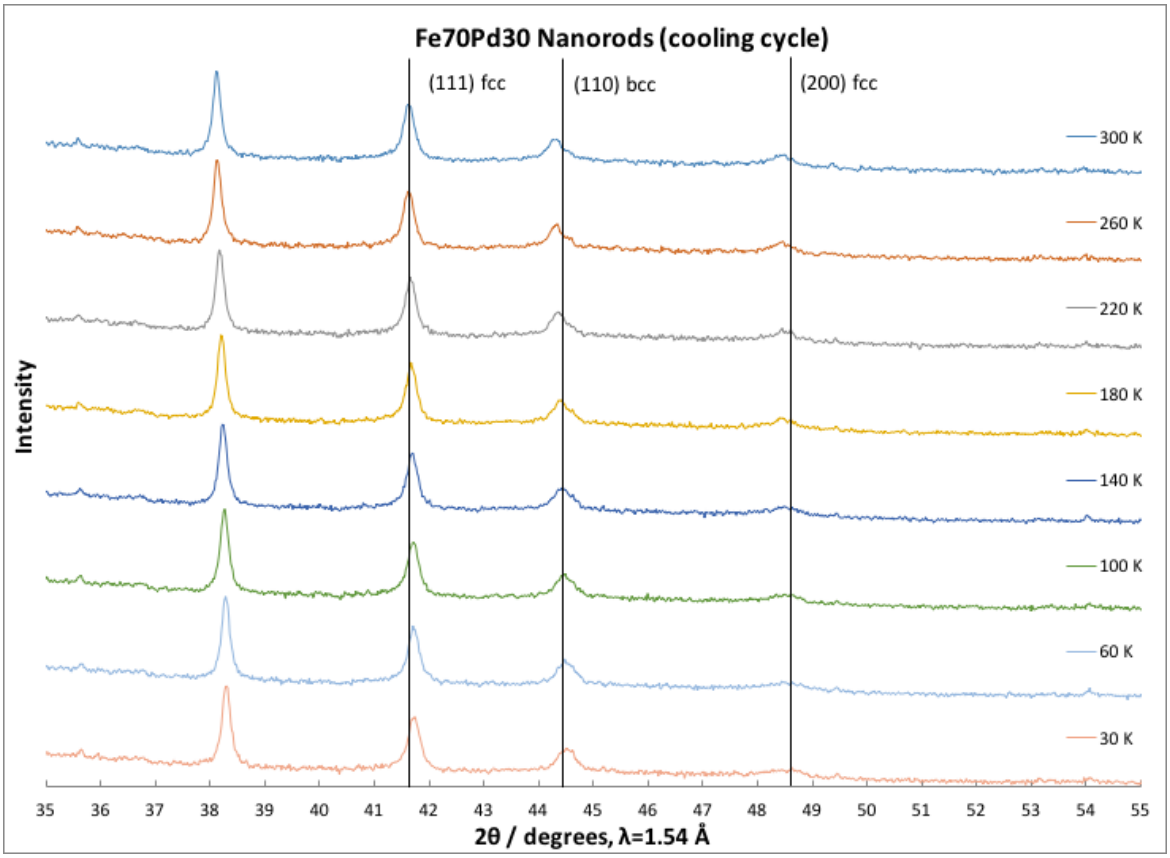

Figure 21: Synchrotron XRD spectra of FePd nanowires, as cooled from 300 K to 30 K

Figure 21 depicts the crystal structure for the FePd nanowires that had been synthesized in homemade PAA templates and extracted by etching. The peaks are wider than those of the

nanoparticles, indicating they have smaller crystallites that make up multiple phases, which is not optimal for FMSA behavior. More fine crystallites result in more stress at grain boundaries, inhibiting martensitic transition. The slight shift in peak location as the temperature dropped indicates the crystallites experienced contraction, but there was not a shift from austensite to martensite phase, as explained by the presence of bcc phase. Evidence for a phase change would rather be the disappearance of the fcc peaks at the Ms′ temperature and reappearance of an fct peak at the Mf′ temperature: fct (111) at 41.5° and fct (200) at 47.3°. The sharper peak at 38.1° is gold, indicating that it was not fully etched away from the nanowires before analysis.

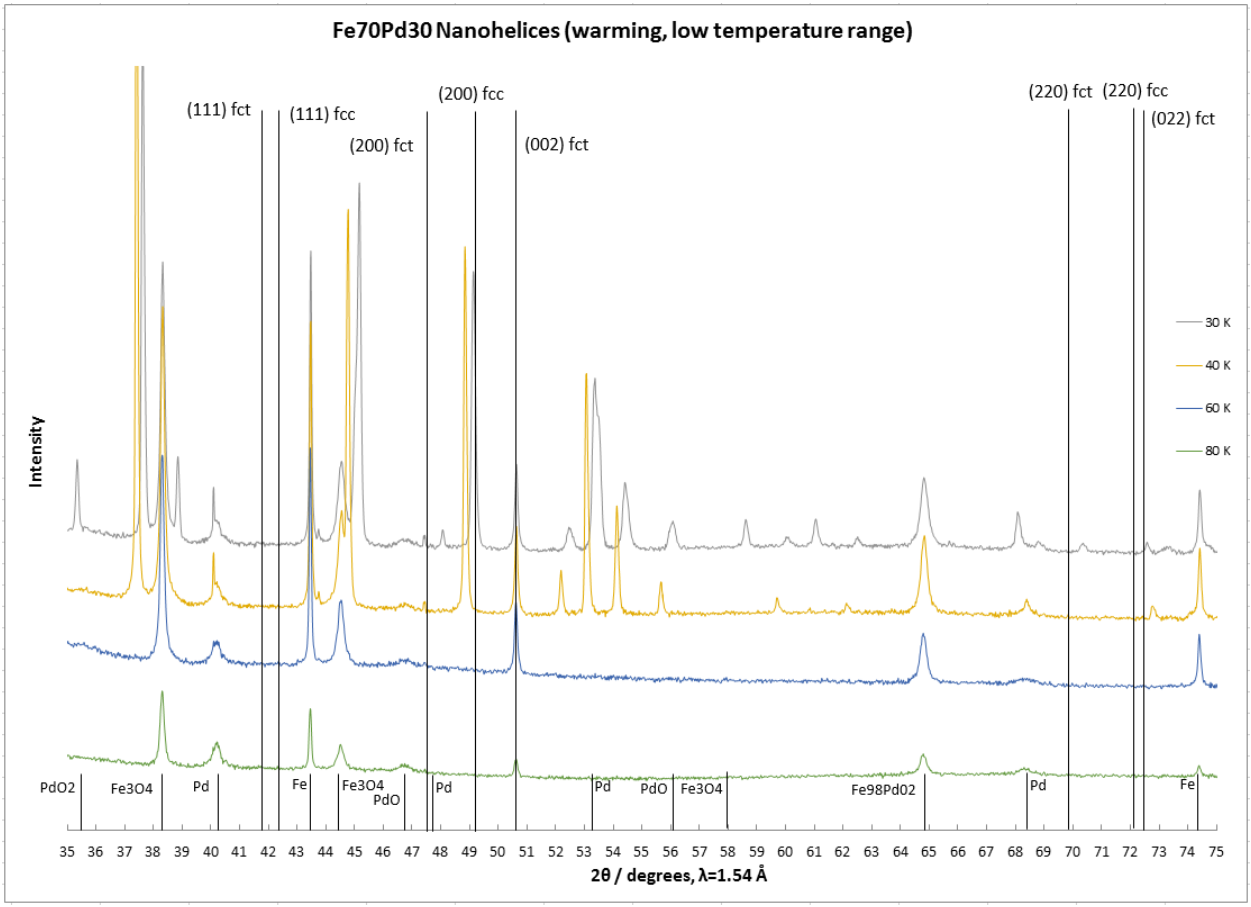

Figure 22: Synchrotron XRD spectra of FePd nanohelices, as cooled from 300 K to 30 K

Unlike the nanowires and nanoparticles, the nanohelix sample experienced changes in

structure at lower temperatures (Figure 22). The spectrum was identical from 300 K to 80 K (green), but at 60–30 K a variety of peak changes occurred. Because there was not a peak for fcc (111), the sample was likely not actually $Fe_{70}Pd_{30}$, but contained other contaminants. Spectral analysis software (DIFFRAC.EVA, Bruker) could not clearly identify specific crystal structures at the low temperatures but the sample had peaks that may signify an amorphous mixture of Fe, Pd, and Fe_3O_4.

Subsequent characterization at SPring-8 attempted to examine the residual stress of the nanowires annealed in commercial template by measuring spectra of samples with differing amounts of strain from coefficient of thermal expansion mismatch. Samples were either annealed as-deposited leaving $h/h_0=1$ so that the full length of the nanowires experienced CTE mismatch or annealed after partial etching of the template leaving $h/h_0<1$ so that some of the nanowires' length was free to expand unconstrained by the surrounding template. Etching of the template in 5% phosphoric acid revealed about 0.5 nm/min. After annealing at 830°C for 5 min, followed by rapid quenching, templates were broken into small pieces (<0.5mm) for powder diffraction in capillary tubes.

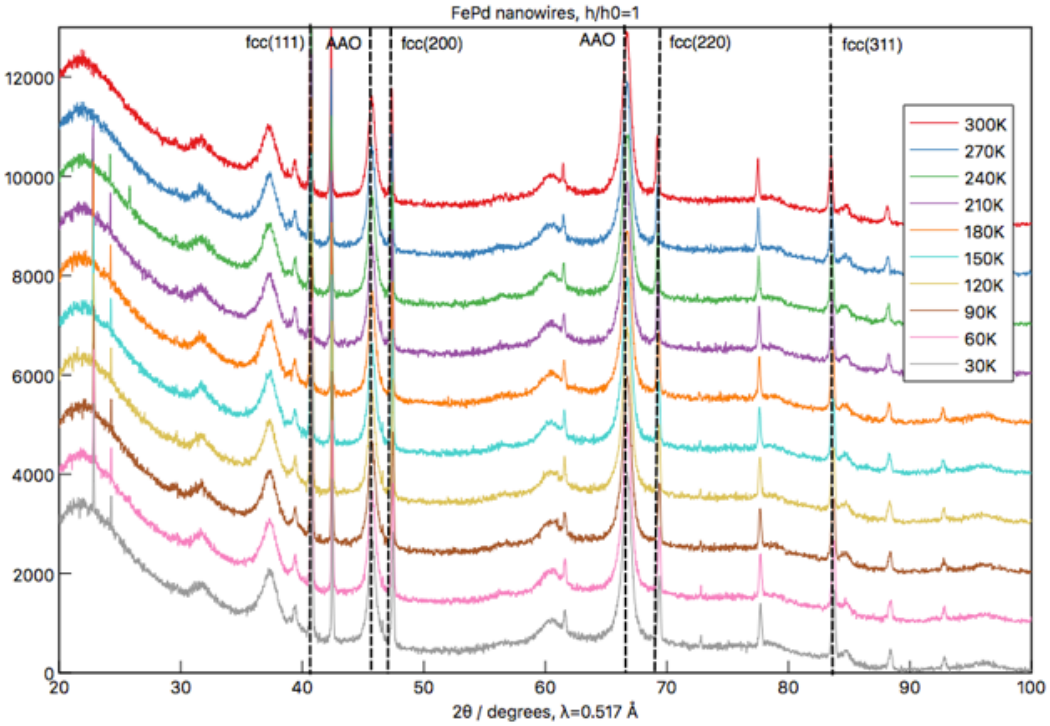

Figure 23: XRD spectra of nanowires embedded in alumina template without etching

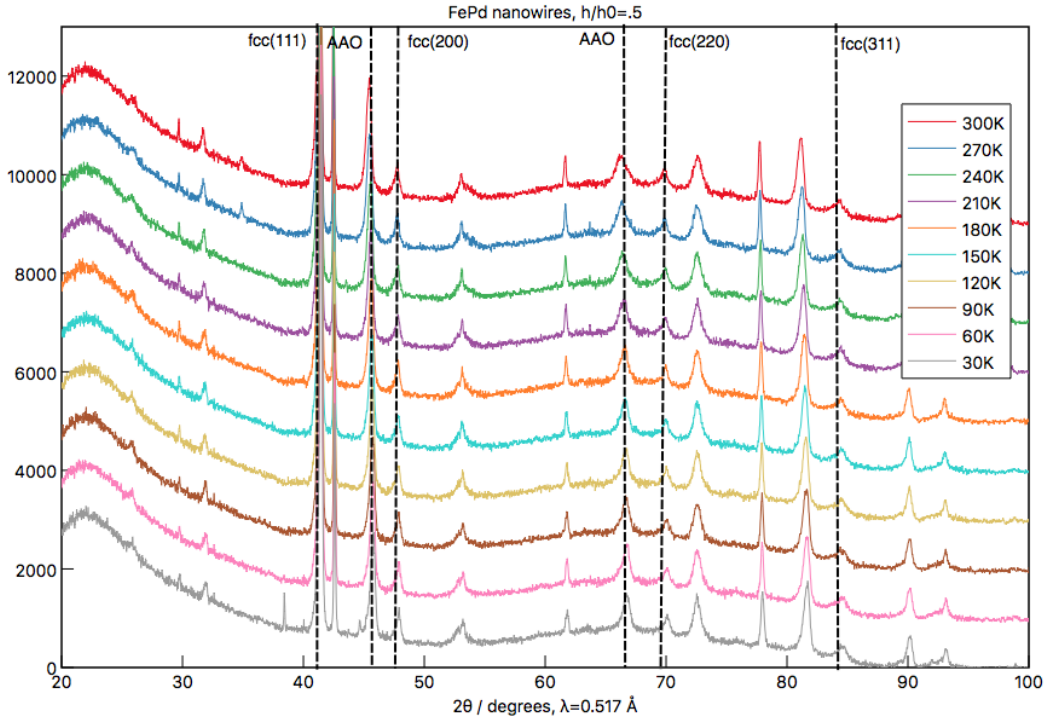

Figure 24. XRD spectra of nanowires embedded in alumina template partially etched

For the nanowires that were fully embedded in the alumina template (h/h0=1), sharp characteristic peaks for the austenite phase were observed, namely fcc (111) at 40.7°, fcc (200) at 47.4°, fcc (220) at 69.4°, and fcc (311) at 83.7°. Amorphous PAA background was at 45.8° and 66.8°. Similar peaks appeared for nanowires for fcc and PAA.

However, these patterns were unchanged across the range of 300K to 30K, indicating there was no martensitic transformation to this temperature. While it is possible that the small size of the samples resulted in an Ms′ below 30 K, the presence of a peak at 44.5° indicates that bcc (110) may be present, inhibiting the martensitic phase transformation. Peaks for bcc (200) at 65° and bcc (211) at 82° are however absent. While nanowire samples were measured to average Pd composition at 30%, there is likely wider spatial variation resulting in excessive bcc phase or pure fcc phase that would not exhibit transition to fct. Bcc presence disrupts the reorganization of atoms as a discontinuity in the lattice constant across the volume of the nanowire. As grain sizes also influence the transformation, these samples, with a diameter of ~100 nm, would be expected to have much lower transition temperatures than observed in polycrystalline materials.[70]

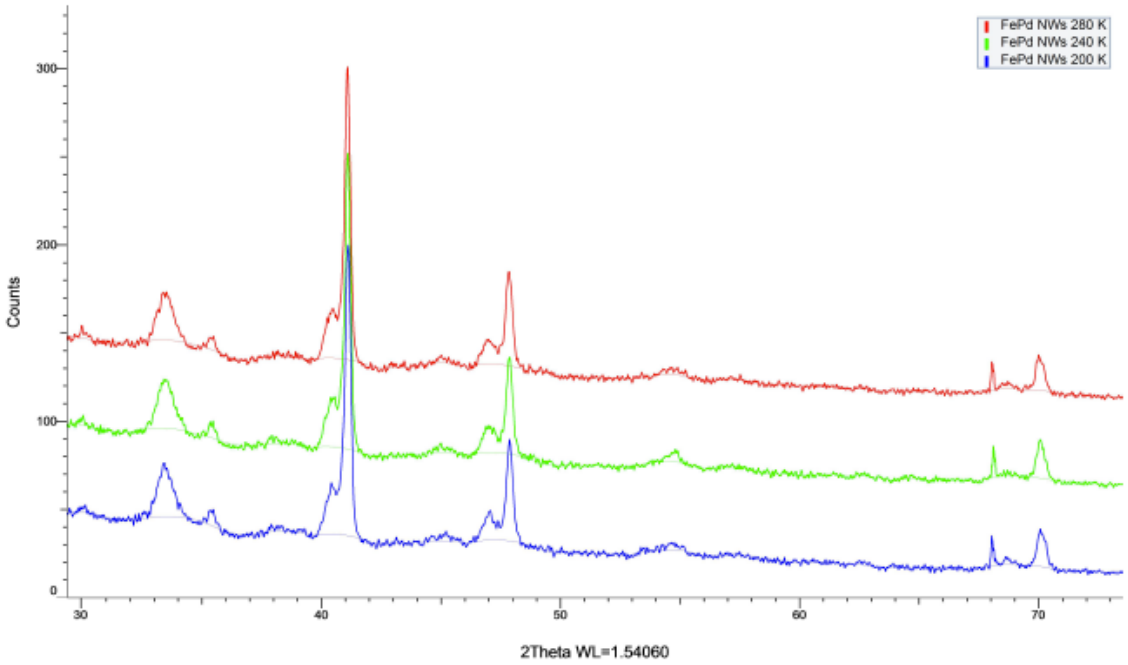

Figure 25. XRD spectra of FePd nanowires at 280 K, 240 K, and 200 K

Without easy access to SPring-8, additional XRD analysis was performed at UW's Molecular Analysis Facility. The sample in Figure 25 has characteristic peaks for fcc FePd and lacks the bcc peak seen previously, indicating greater purity in the γ phase. However, with this instrument only reaching 200 K in its cryogenic operation, no shift in peaks was observed. The steep dependence of transition temperature on grain size in Seki, 2008[70] projects an Ms′ well below 100 K. This explains the lack of change observed in low-temperature experiments using the UW XRD, though not necessarily in the SPring-8 experiments, which reached 30 K. The likely cause of SPring-8 data not showing transformation is presence of bcc phase. Post-annealing nanowires were not observed by SEM to have distinct grains that would influence transition temperature; even the smallest in the study of bulk pieces[70] are larger than these samples, and this would likely require TEM to detect.

The primary mechanism that inhibits the martensite transformation is surface free energy,

related to surface area to volume ratio. For smaller nanoparticles, there is a greater nucleation barrier to phase transformation, as the nucleation site initiating a γ to α transition would be embedded in a grain that must be large enough to distance the nucleation site from interface stress at the grain boundary.[108] While Meng et al. examined the fcc to bcc transformation in Fe and FeNi nanoparticles, it is applicable to FePd samples, with grain diameter under 100 nm being particularly relevant. Another concern is the relaxation of the embedded strain subsequent to quenching. While pressurizing Fe nanoparticles up to 4.0 GPa would induce martensite transformation, as-prepared quenched samples would not.[109] Free nanomaterials may relax the strain that should be internally stored during quenching. While the nanowires embedded in alumina template during annealing and quenching should have embedded residual strain due to mismatch of coefficient of thermal expansion, it is possible that the open pore tops and bottoms allow for release of some strain, that the thermal expansion does not induce as much strain as expected due to the morphology of the nanowires, or that the nanowires contract at the point of quenching and not all of the pressure-induced strain locks in rapidly enough. The breaking of the template for powder diffraction may also release the strain in nanowires in pores along the fracture sites, but that is only a small fraction of pores, with small size relative to the broken PAA pieces.

2.7 Summary and outlook

In this work we demonstrated the synthesis of FePd nanowires in both homemade and commercial PAA templates by electrochemical deposition for the purpose of developing a ferromagnetic shape memory alloy nanoactuator. Homemade templates are produced by a two-step method of anodization of aluminum with a pore diameter of 50 nm and thickness of 1 μm,

while commercial templates are 200 nm wide and 50 μm thick, requiring different electrodeposition techniques. FePd nanowires are electrodeposited on Au base nanowires using a pulse-plating potential pattern, followed by annealing to homogenize the material. Low-temperature X-ray diffraction was conducted to determine crystal structure and observe phase transformation. Processed samples, while measured to have $Fe_{70}Pd_{30}$ composition, were not observed to exhibit the austenite–martensite phase transformation expected for the shape memory alloy at low temperatures. Grain size in the nanoscale suppresses martensite phase starting temperature, but the presence of bcc phase also inhibits the deformation of the fcc lattice, preventing a change in volume. Further helium-cooled XRD experiments are suggested to study additional samples produced and shown not to contain bcc but which do not reach Ms′ under nitrogen cooling. Repeated annealing of bcc-containing nanowires may result in recrystallization of samples into only the desired fcc phase, provided accurate composition. Spatial distribution changes in the nanowire composition may be present, resulting in high-Fe or high-Pd regions with mismatched lattice boundaries. Unfortunately, due to the death of the principal investigator Minoru Taya and disruptions caused by COVID-19, additional investigations could not be conducted.

In addition to nanowires, nanohelices produced via a nanoconfinement template, with even smaller grain size, did not exhibit martensite transformation. Nanohelix templates are split between left- and right-handed chirality, which will respond differently as magnetic field-guided nanorobots. Future work can involve synthesis of nanowires and nanohelices of various diameters to better understand size effects on the ferromagnetic shape memory alloy effect. Comprehension of these mechanics and dynamics can lead to using an electromagnetic Helmholtz coil, such as that designed in our group,[110] to control propulsive swimming

motions and actuation of the materials as nanorobots. Making use of surface modification like that we conducted on nanoparticles with a biocompatible SBSi membrane[100] allows for *in vivo* testing for effectiveness at causing mechanical stress-induced cell death. Development of nanorobots may yet prove to be a promising pathway for cancer treatment.[68]

Chapter 3: Energetics of adsorbed formate and formic acid on Ni(111) by calorimetry

This chapter adapted with permission from: Zhao W, Carey SJ, Morgan SE, Campbell CT. Energetics of adsorbed formate and formic acid on Ni(111) by calorimetry. *J Catal*. 2017; 352:300-304. doi: 10.1016/j.jcat.2017.05.023

3.1 Introduction

Adsorbed formate is considered an important intermediate on catalyst surfaces for many catalytic reactions on late transition metal surfaces, including steam reforming of methane, methanol synthesis, and water-gas shift.[19], [20], [112] It is a likely intermediate whenever CO_2 with H_2 or water are present above a catalyst, as is true in all oxidation and steam reforming reactions of organic molecules. More complex carbonates (e.g., acetate and longer alkyl carbonates, and various functionalized versions of these) are also frequently suggested as intermediates in catalytic reactions, and since formate is the simplest example of this class of adsorbates, it serves as a prototype for understanding the bonding of this whole class of adsorbates. Moreover, the interactions of organic molecules containing $-COO^-$ and $-COOH$ groups with surfaces, such as amino acid residues, peptides, and proteins, are also important for the organo-functionalization of surfaces,[113] and their use in medical applications,[114] medical implants,[115] and many other areas. Thus, characterization of the energetics of adsorbed formate on surfaces is obviously crucial for the fundamental understanding of a wide variety of surface reactions and catalytic processes. However, the heat of formation for surface formate has only been previously measured on one surface, Pt(111), as previously reported by this group.[116] Here we report calorimetric measurements of the heat of formation of adsorbed formate on Ni(111) and find it to be bound 54 kJ/mol more strongly than to Pt(111). Since this is

the first experimental measurement of the heat of formation of any adsorbed molecular fragment on any Ni surface whereby it is linked to the surface through O-Ni bonds, this result for bidentate formate will serve as a benchmark for validating the energy accuracy of theoretical estimates of the stability of many oxygenates bound to Ni catalyst surfaces. One of the simplest ways to produce formate is dissociative adsorption of formic acid on the surface as reported on Pt(111),[117] O/Pt(111),[116], [118] Ni(111),[119]–[121] Rh(111),[122] and O/Mo(110).[123] That is the method used here to produce this formate species. We also report the adsorption enthalpy of molecularly adsorbed formic acid on Ni(111) at 120–155 K.

As noted in Chapter 1, nickel can take on several oxidation states, making it an important metal catalyst in many chemical applications including those where formate is an adsorbed intermediate, e.g., steam reforming of hydrocarbons and water-gas shift.[124], [125] It also benefits from its high heat conductivity, as its valence d electrons can transfer energy easily, facilitating heat control in exothermic reactions.[125] The (111) surface is the most thermodynamically-stable Ni facet and thus it has been widely studied as a well-defined model for Ni-related catalysts.

Previously, the adsorption and dissociation of formic acid on Ni(111) were experimentally studied by temperature-programmed desorption (TPD),[126], [127] infrared reflection adsorption spectroscopy (IRAS)[126], [128] and time-resolved sum-frequency generation (SFG) spectroscopy.[120], [121], [128] It has been agreed that formic acid molecularly adsorbs on Ni(111) at low temperatures (< 190 K) and that gaseous formic acid monomers dissociatively absorb to form adsorbed formate and adsorbed hydrogen at elevated temperatures above 225 K. Formate was found stably bonding to the Ni(111) surface in the bidentate configuration (i.e., the two oxygen atoms separately bond to two neighboring Ni

atoms) at 250 K, and the monodentate form has not been reported except in one unusual case. Adsorbed bidentate formate was reported to transform transiently into unstable monodentate formate by the rapid laser-induced temperature jump of ~300 K, which was well studied by the time-resolved SFG studies.[120], [121], [128]

Here, we directly measure the heat of molecular adsorption and dissociative adsorption of formic acid monomers onto clean Ni(111) at different temperatures (120 – 240 K) by calorimetry under ultrahigh vacuum conditions, and extract the enthalpy of formation and the bonding enthalpy of adsorbed bidentate formate on Ni(111). These energetic values not only serve as benchmarks for theoretical studies to improve the accuracy of calculation methods such as DFT, but they also help clarify the energetics of important elementary reaction steps that occur in catalysis on nickel surfaces.

3.2 Experimental methods

Experimental work was performed by Wei Zhao, Spencer Carey, and Sawyer Morgan in the Campbell lab and is adapted here with permission from [111]. The experiments were performed in an ultrahigh vacuum (UHV) chamber (base pressure $<2 \times 10^{-10}$ mbar), designed for single-crystal adsorption calorimetry (SCAC) and surface analysis, as described previously.[129], [130] Briefly, the chamber is equipped with low-energy electron diffraction (LEED), Auger electron spectroscopy (AES), X-ray photoelectron spectroscopy (XPS), low-energy ion scattering spectroscopy (LEIS), a quadrupole mass spectrometer (QMS) and a liquid-nitrogen-cooled quartz crystal microbalance (QCM).

The Ni(111) sample used here is a 1 μm thick single-crystal foil, supplied by Jacques Chevallier at Aarhus University in Denmark and the surface was cleaned by cycles of Ar^+ ion

sputtering and annealing. A detailed description of the experimental principles and implementation of the molecular beam flux, sticking probability, and heat measurements can be found elsewhere.[129]–[131] Briefly, the Ni(111) surface, held at different temperatures, was exposed to a pulsed molecular beam of formic acid and the heat of adsorption and sticking probability were recorded simultaneously. The heat of adsorption was detected using a pyroelectric heat detector pressed against the back of the Ni(111) crystal, and the sticking probability was measured with the QMS. The beam was created by expanding ~2 mbar of formic acid through a microchannel array and then collimated through a series of five liquid nitrogen cooled orifices, and chopped into 102 ms pulses every 5 s with a rotating chopper blade. The microchannel array was heated and kept at 360 K to reduce gas-phase dimerization to less than 1%.[132] We define the coverage of formic acid molecules which adsorb onto the surface irreversibly in units of monolayers (ML) where 1 ML = 1.86×10^{19} atoms/m^2, which is the surface atom density of Ni(111). A typical dose is 0.007 ML (~1.2×10^{12} molecules within the beam diameter of ~4 mm) per formic acid pulse.

3.3 Results

3.3.1 Sticking Probability

The short-term (S_{102ms}) and long-term (S) sticking probabilities of formic acid on clean Ni(111) were measured at four temperatures, as shown in Figure 1. The coverage reported here and elsewhere represents the formic acid permanently adsorbed, regardless of the products produced. The long-term sticking probability is the probability that a gas molecule strikes the sample surface, sticks, and remains until the next gas pulse starts ~5 s later, which is used to calculate the adsorbate coverage remaining at the start of the next gas pulse. The short-term

sticking probability is the probability that a gas molecule strikes the sample surface, sticks, and remains at least throughout the time window of our heat measurement (i.e., the first 102 ms). This is used to calculate the number of moles of gas-phase reactant that contribute to the measured heat of adsorption. At all temperatures, the initial sticking probabilities are high (>0.8) and slightly increase as more formic acid molecules adsorbed, indicating a precursor-mediated adsorption mechanism. At 120 K, the formic acid molecularly adsorbs on the surface and forms a multilayer (see below), with both the long-term and short-term sticking probabilities almost unity even to multilayer coverages. At 155 K, the long-term sticking probability quickly decreases to zero between 0.35 and 0.45 ML, while the short-term sticking probability remains high (>0.85). This indicates that the first adlayer of formic acid on Ni(111) saturates at 0.45 ML, but that formic acid still transiently adsorbs with high probability on that saturated adlayer and desorbs again slowly (but before the next pulse arrives 5 s later). The formic acid is only molecularly adsorbed at 155 K, and does not yet dissociate (see below). For 210 K and 240 K, where formic acid dissociates to make formate and H_{ad} at low coverages (see below), the long-term sticking probabilities decline earlier than at 155 K, with saturation coverages of 0.20 ML for 210 K and 0.14 ML for 240 K, while the short-terms sticking probabilities stay high (> 0.85), similar to 155 K. Again, this indicates that the formic acid molecules transiently adsorb on the surface after saturation, but desorb again within 5 s before the next pulse.

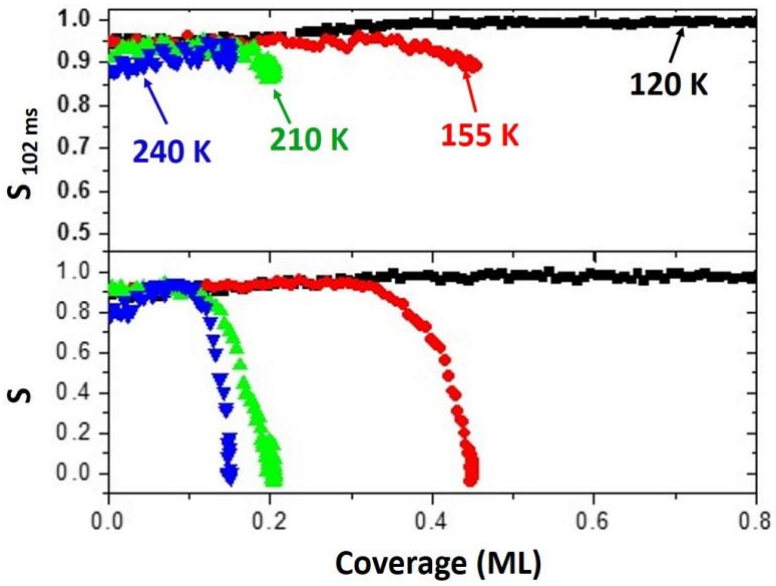

Figure 1: Short-term (top) and long-term (bottom) sticking probabilities of formic acid on clean Ni(111) at 120, 155, 210, and 240 K as a function of total formic acid coverage that adsorbed irreversibly, irrespective of whether it dissociated.

3.3.2 Heats of Adsorption

In this paper, the term heat of adsorption is defined as the negative of the differential standard molar enthalpy change for the adsorption reaction, with the gas and the sample surface being at the same temperature. As described previously, this requires a small enthalpy correction on the measured heat since the gas molecule's enthalpy at this temperature is slightly different from the actual experimental molecular beam conditions.[131] Figure 2 shows the evolution of this differential heat of adsorption of formic acid on Ni(111) as a function of the coverage of adsorbed formic acid at four representative temperatures.

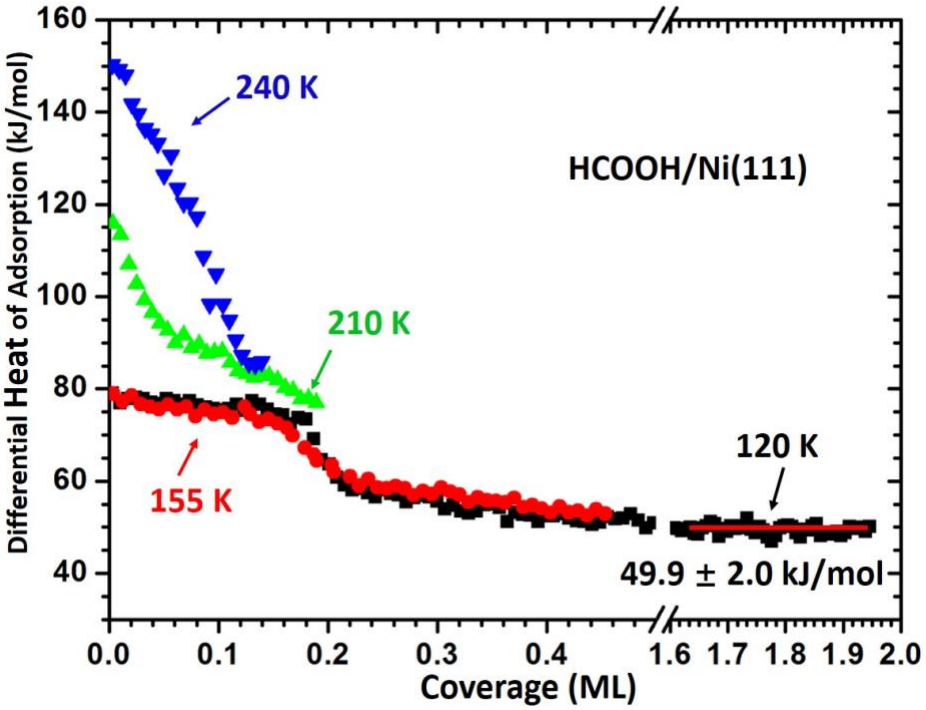

Figure 2: Heats of adsorption of HCOOH on clean Ni(111) at 120, 155, 210, and 240 K as a function of total formic acid coverage that permanently adsorbed. The average heat of adsorption reached at the thick multilayer limit is marked by a horizontal red line though the 120 K data.

As known from the literature, formic acid molecularly adsorbs on Ni(111) below 190 K,[126] Thus, the calorimetric measurements at 120 K and 155 K reflect the molecular adsorption of formic acid on Ni(111). The heat of adsorption at 120 K is initially 79.0 kJ/mol, dropping slightly to 71.5 kJ/mol by 0.16 ML, and the integral heat of molecular adsorption is 75.2 kJ/mol at 0.16 ML. After 0.16 ML, the heat decreases quickly to ~60 kJ/mol by 0.20 ML and more slowly to 51 kJ/mol at 0.45 ML, and finally remains constant beyond 0.45 ML as further multilayers of formic acid are created at 49.9 ± 2.0 kJ/mol (the error here is the run-to-run standard deviation). This final heat is consistent with the heat of adsorption of multilayer formic acid on Pt(111) reported by this group previously.[116] We can compare the measured multilayer heat to the multilayer desorption of formic acid from TPD in the literature.[126] To do this, we estimate that the prefactor for desorption is $10^{15.3}$ s^{-1} following the entropy method

developed by Campbell and Sellers[133], [134] using the gas-phase entropy of formic acid at 160 K of 248.7 J/(mol K).[135] The activation energy for desorption is estimated to be 48.9 kJ/mol from the reported temperature of desorption peak at 160 K[126] using simple first-order Redhead analysis.[134] In comparison to the calorimetric multilayer heat of adsorption, 1/2 RT has to be added to the TPD value, giving 49.6 kJ/mol, showing essentially perfect agreement. This confirms the absolute accuracy of our calorimetric heats.

The heat of molecular adsorption versus coverage at 155 K simply reproduces the same features of adsorption at 120 K until 0.45 ML, where the first adlayer of molecular formic acid is completed. This confirms the saturated coverage for formic acid molecularly adsorbed on Ni(111) is 0.45 ML ($8.3\times10_{18}$ molecules/m_2). In comparison to the saturated coverage of 0.5 ML ($7.5\times10_{18}$ molecules/m_2) for formic acid on Pt(111),[116] the higher packing density can be explained as the stronger binding for formic acid to Ni(111), as the integral heat of molecular adsorption on Ni(111) is ~12.7 kJ/mol higher than that on Pt(111) (the integral heat of molecular adsorption on Pt(111) is 62.5 kJ/mol at 0.25 ML).[116]

The step-like decrease in heat seen at ~1/6 ML at both 120 and 155 K indicates that the repulsions between adsorbates suddenly become stronger at packing densities higher than 1/6 ML. One structural model that is consistent with this 1/6 ML packing has rows of hydrogen-bonded HCOOHs separated by $\sqrt{3}$ but with a distance of $2\sqrt{3}$ between these rows along the other lattice direction from the rows. The H-O hydrogen bonds between HCOOH molecules inside these rows leaves the C-H groups on the outside of these rows. These C-H groups will repel the C-H groups from the nearest-neighbor rows, such that the repulse gets big as the rows get closer together than $2\sqrt{3}$. A similar situation is seen in STM and DFT studies of methanol on Cu(111) and Au(111).[136], [137] On both surfaces, the methanol molecules lie sideways on the surface

and cluster together into hydrogen-bonded rows, with the methyl groups pointing outwards from the rows and evidence that the rows repel each other. Molecularly adsorbed formic acid has been studied with STM on Cu(111) at 145 K,[138] where indeed it was seen that they also form hydrogen-bonded rows with the C-H groups point outwards. However, there is no evidence for repulsive interactions between these rows up to the saturation coverage of ~1/3 ML.

At 210 K, the differential heat starts from a higher value of 115.8 kJ/mol, then deceases to 76.9 kJ/mol at the saturation coverage of 0.20 ML. The adsorption at 240 K even releases higher differential heats, starting with 150.3 kJ/mol, and saturating at 0.14 ML with a differential heat of 85.8 kJ/mol. The saturated layer coverage of 0.14 ML suggests a ($\sqrt{7} \times \sqrt{7}$) structure, with an ideal coverage of 1/7 ML. The heats of adsorption at 210 K and 240 K are significantly higher than molecular adsorption at 155 K and 120 K, and it is more exothermic for 240 K. According to the literature, formic acid dissociatively adsorbs on Ni(111) to form adsorbed bidentate formate and adsorbed hydrogen above 225 K, and the adsorbed bidentate formate is stable up to ~350 K.[120], [127], [128], [139] Therefore, the measured heat at 240 K in our calorimetry experiment is assigned to the heat of dissociative adsorption of formic acid leading to adsorbed bidentate formate and adsorbed hydrogen with an integral heat of 117.1 kJ/mol at 1/7 ML, reaction shown as the equation (1). This coverage of 1/7 ML suggests that coadsorbed bidentate formate and hydrogen form a ($\sqrt{7} \times \sqrt{7}$) coadsorbed structure with 1/7 ML of each:

$$HCOOH_g \rightarrow HCOO_{bi,\,ad} + H_{ad} \qquad (1)$$

We also studied the adsorption of formic acid on Ni(111) at 250 and 300 K. It is found that water desorbs from the surface (as monitored by QMS) during each dosing pulse, indicating that formic acid starts to partially dissociate into adsorbed OH plus CO on Ni(111) above 250 K, and two OHs react to produce water, which desorbs. The heat of adsorption was consequently

lower than that at 240 K.

Interpretation of the heat of adsorption measured at 210 K in terms of an adsorbed structure is less clear, due to the lack of previous structural studies at this temperature. According to the literature, formic acid molecularly adsorbs on Ni(111) below 190 K and dissociates into adsorbed bidentate formate above 225 K.[120], [126], [128], [139] However, there have been no experimental studies of the surface reaction of formic acid on Ni(111) or characterization the nature of the adsorbed product(s) at 190 – 225 K. Here for the calorimetric data, the adsorption at 210 K is more exothermic than molecular adsorption at 120 – 155 K, but less exothermic than the dissociative adsorption making bidentate formate at 240 K. Therefore, it could be the dissociative adsorption making monodentate formate plus adsorbed hydrogen at 210 K in our experiments. But the assignment of monodentate formate is questionable since the adsorbed monodentate formate has not been experimentally observed on Ni(111) as a stable species. In contrast, monodentate formate has been found on O/Pt(111) at relative low temperatures and converts to bridged bidentate formate upon heating to 190 – 200 K.[118] Our group previously measured the heat of dissociative adsorption of formic acid on O/Pt(111) at 100 K forming monodentate formate plus adsorbed hydrogen, finding it to be less exothermic than when making bidentate formate at slightly higher temperature.[116] It was found that monodentate formate is a stable species on O/Mo(110) at 190 K.[123] Bowker et al. found monodentate formate on Cu(110) at 200 K.[140] Hirose's group observed the transformation from bidentate formate on Ni(111) at 250 K to the unstable monodentate formate by the rapid laser-induced temperature jump of ~300 K, but monodentate formate decays in ~100 ps and transforms back to bidentate formate at ~550 K.[120], [121][128] Furthermore, these SFG spectroscopy studies from Hirose's group concluded that the monodentate formate is the

intermediate state before bidentate formate decomposes on Ni(111). Here at 210 K, a larger activation energy could make the decay of monodentate formate much slower than at ~550 K, whereas we could capture it in the short heat measurement period. Instead of making monodentate formate, the measured heat at 210 K could also be due to the formation of a coadsorbed mixture of bidentate formate and molecularly adsorbed formic acid, since Dubois et al. found the coexistence of molecular formic acid and the bidentate formate species on Cu(100) at 120 K.[141]

3.4 Discussion

3.4.1 Enthalpies of Formation of Adsorbed Bidentate Formate on Ni(111)

Our calorimetric measurements represent the heats of formic acid adsorption onto Ni(111), molecularly and dissociatively. Using available literature values for the heats of formation of various gas-phase and adsorbed molecules, we can determine the enthalpies of formation of adsorbed bidentate formate and the HCOO=Ni(111) bond enthalpy with the measured heat at 240 K, shown as the thermodynamic cycles in Figure 3.

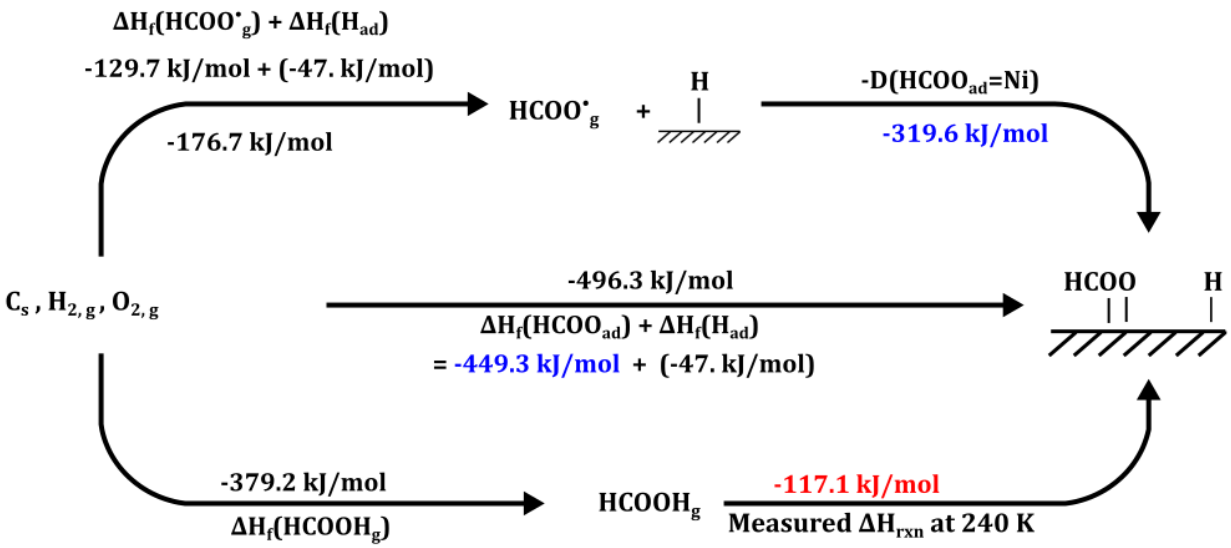

Figure 3: Thermodynamic cycles used to determine the heat of formation of bidentate formate adsorbed on Ni(111) from the calorimetric *integral* heat of dissociative formic acid adsorption at 240 K and 1/7 ML (shown in red). The top right-hand step shows the enthalpy to form bidentate formate from gas-phase formate radical, which provides an estimate of the total bond enthalpy of bidentate formate to Ni(111), from both its O-Ni bonds. Enthalpies in black are literature values as referenced in the text.

The bottom route in the cycle begins with carbon, hydrogen, and oxygen all as elements in their standard states, with the bottom-left arrow forming gas-phase formic acid with the standard heat of formation $\Delta H_f(HCOOH_g) = -379.2$ kJ/mol.[141] The bottom-right arrow then represents the dissociative adsorption process, which we measured by calorimetry. This is the *integral* enthalpy of dissociative adsorption of formic acid resulting in bidentate formate and a hydrogen adatom at 240 K, −117.1 kJ/mol at 1/7 ML. While this heat of adsorption represents an exothermic process and thus has negative reaction enthalpy in the thermodynamic cycle, the heats were shown as positive values in Figure 2 to represent the corresponding heat release (and thus they represent the negative of reaction enthalpies there).

The middle route in the cycle of Figure 3 is the direct conversion of standard-state elements to the adsorbed products, which is energetically equivalent to the bottom route.

Subtracting the known enthalpy of formation of adsorbed hydrogen on Ni(111) at 1/7 ML coverage ($\Delta H_f(H_{ad})$) of −47 kJ/mol,[142] we calculate the standard enthalpy of formation of adsorbed bidentate formate, $\Delta H_f(HCOO_{bi,ad})$, to be −449.3 kJ/mol.

The top route of the thermodynamic cycle allows for a similar calculation of the bond enthalpy between adsorbed bidentate formate and the Ni(111) surface. The top left arrow takes the standard-state elements to a gas-phase formate radical and adsorbed hydrogen (H_{ad}) by means of their enthalpies of formation, −129.7 kJ/mol[143] and −47 kJ/mol,[142] respectively. This allows for the calculation of the unknown top right arrow energy change, representing the negative of the adiabatic total bond dissociation enthalpy between bidentate formate and Ni(111), to be −319.6 kJ/mol. Thus, +319.6 kJ/mol is the total enthalpy arising from breaking both of the O-Ni bonds that link bidentate formate to the Ni(111) surface, or *D*(HCOO=Ni).

3.4.2 Comparison to DFT Calculations

The experimental results are valuable for the validation and improvement of computational models. The heats of molecular and dissociative adsorption of formic acid, heats of formation of $HCOOH_{ad}$, $HCOO_{bi,ad}$, and bond energy of formate to Ni(111) measured in this work are compared to theoretical calculations from the literature in Table 1, which provides the experimentally measured bond energy of bidentate formate to Ni(111) at 1/7 ML and 240 K (319.6 kJ/mol –RT = 317.6 kJ/mol) and five calculated bond energies by DFT at zero K. The experimental bond energy is 25.6 to 57.6 kJ/mol greater than those found by DFT methods. These differences are much larger than expected zero-point energy and heat-capacity corrections, which are not included in the comparison. This indicates that these DFT calculations systematically underestimated the bond strength of formate to Ni(111), possibly partly due to

their potential error in the DFT energy of gaseous formate radical.

Table 1. Comparison of Present Calorimetric Bond Energy of Bidentate Formate to the Ni(111) Surface with DFT Calculated Values. The calculations with zero-point energy (ZPE) corrections are marked with "with ZPE".

Coverage	Functional or Method	Bond energy (kJ/mol)	Ref
1/7 ML	Calorimetry	317.6	This paper
DFT Methods			
1/9 ML	PBE	273	[144]
1/9 ML	PW-91 (with ZPE)	270	[145]
¼ ML	PBE	260	[146]
¼ ML	PBE	291	[112]
1/9 ML	PW-91	292	[22]

3.4.3 Comparison to Pt(111)

Previous calorimetric measurements have determined the bond energy for bidentate formate to the Pt(111) to be 265.6 kJ/mol at the formate coverage of 1/7 ML.[116], [147] It is weaker than the bond strength of 319.6 kJ/mol for bidentate formate to Ni(111) by 54 kJ/mol at the same coverage of 1/7 ML. This difference is expected, since Ni is generally considered more oxophilic than Pt. This result agrees to within 11 kJ/mol with a theoretical study using DFT (PW-91), which determined the bond energy for bidentate formate to Pt(111) to be less than to Ni(111) by 43 kJ/mol.[145] From the literature,[147] the enthalpy of formation for adsorbed hydrogen on Pt(111) is -36 kJ/mol and that value for Ni(111) is -47kJ/mol, indicating that the bond strength of hydrogen to Pt(111) is also weaker than to Ni(111) by 11 kJ/mol. The fact that both of the products of the dissociative adsorption of formic acid are more stable on Ni(111) than on Pt(111) explains why the activation barrier for the dissociative adsorption of formic acid to $HCOO_{ad}$ plus H_{ad} is lower on Ni(111) than on Pt(111), since the activation barrier for a process is

lower on surfaces where it is more exothermic, according to the Brønsted−Evans Polanyi (BEP) relation. The larger barrier for Pt(111) is seen by the fact that formic acid dissociatively adsorbs on Ni(111) at 240 K but does not on Pt(111) even at higher temperatures, where oxygen adatoms are needed to extract the H from formic acid.[116] It has also been reported by others that the dehydrogenation of formic acid to formate is easier on Ni(111) than Pt(111).[144] Moreover, the greater stability of formate on Ni(111) compared to Pt(111) also explains that nickel is more active than platinum for hydrogenation of CO_2, as explained by theoretical studies with DFT which show that the energy barrier for adding an adsorbed hydrogen to physisorbed CO_2 to form adsorbed formate on Pt(111) is 1.39 eV,[20] while that value is only 0.6 eV on Ni(111).[22]

3.5 Conclusions

The enthalpy of formation of bidentate formate on Ni(111) is −449.3 kJ/mol at 1/7 ML. The bond dissociation enthalpy of bidentate formate on Ni(111) (i.e., including both Ni-O bonds) is 319.6 kJ/mol. The heat of adsorption of molecularly adsorbed formic acid on Ni(111) is 63.2 kJ/mol at 0.45 ML. Comparing the measured energies to several different DFT calculations indicates that DFT systematically underestimates the bond energy of bidentate formate to Ni(111). In comparison to previous calorimetric measurements, it is shown that bidentate formate binds to Ni(111) 54 kJ/mol more strongly than to Pt(111) at 1/7 ML, consistent with the expected greater oxophilicity of Ni versus Pt. This finding may help to explain catalytic activity differences between Ni and Pt in several important catalytic reactions involving adsorbed oxygenates. The energies reported here provide reliable experimental adsorption energy benchmarks for the long-term goal of improving the energy accuracy of computational methods like DFT.

Chapter 4: Formic Acid Dissociative Adsorption on NiO(111): Energetics and Structure of Adsorbed Formate

This chapter adapted with permission from: Zhao W, Doyle AD, Morgan SE, Bajdich M, Nørskov JK, Campbell CT. Formic Acid Dissociative Adsorption on NiO(111): Energetics and Structure of Adsorbed Formate. *J Phys Chem C*. 2017; 121(50):28001-28006. doi:10.1021/acs.jpcc.7b09405

4.1 Introduction

Formic acid is a very important feedstock for the modern chemical industry. It is a potential product of CO_2 hydrogenation, possessing a high hydrogen-storage capacity, which is considered as a source of hydrogen for various applications.[149], [150] In general, the activation of formic acid molecules to dissociate on metal or metal oxide catalysts is the first step for utilization of HCOOH, which typically forms the adsorbed formate ($HCOO_{ad}$) by breaking the O-H bond, with the abstracted H atom attaching to the surface. Formate itself is a very important intermediate in all oxidation and steam reforming reactions of organic molecules and likely exists whenever CO_2 with H_2 or water are present above a catalyst.[19], [20], [112] Larger carboxylic acids are also used for organo-functionalization of oxide surfaces, where they often bind via the deprotonated carboxylate functionality.[113] Therefore, characterization of the energetics of dissociative adsorption of formic acid and adsorbed formate on oxide surfaces is obviously crucial for the fundamental understanding of a wide variety of surface reactions and catalytic processes on oxide surfaces. Nevertheless, the heat of the dissociative adsorption has never been reported for formic acid nor any other a carboxylic acid on any single-crystalline oxide surface. Here we report the calorimetric heat of adsorption of the simplest carboxylic acid, HCOOH, on a NiO(111) surface and characterize the resulting formate and hydroxyl structures

using DFT. The heats of formic acid dissociative adsorption onto Pt(111)[116] or Ni(111)[111] have been directly measured using single crystal adsorption calorimetry (SCAC) by this group.

Compared to metal surfaces, much less is understood about the chemistry of oxide surfaces, though they play crucial roles in catalysis. As described in Chapter 1, the oxide surface provides a second type of site on which adsorbates can bind, making use of free election sites and hole sites, while different possible configurations have widely varying binding energies. While the adsorption energies are known for many species which are molecularly absorbed on well-defined, single-crystal oxide surfaces, only a few values have been reported for dissociatively adsorbed species, where the adsorption energy was estimated based on temperature programmed desorption (TPD) of the reverse process (associative desorption), and a pre-exponential factor was assumed for the desorption rate constant.[133] The heat of dissociative adsorption has only been directly measured by calorimetry on two systems involving well-defined, single-crystalline oxide surfaces, i.e., H_2O on Fe_3O_4[151] and H_2O on NiO(111).[152] This paper adds only the third such report for oxide surfaces, and the first to produce adsorbed formate on NiO(111) besides hydroxyls.

Catalysts based on nickel oxides are of great importance in many chemical and environmental applications, such as steam reforming of methane and biomass conversions.[153], [154] Previously, the adsorption and dissociation of HCOOH on (2×2)-NiO(111) thin films grown on Ni(111) were experimentally studied by TPD and infrared reflection adsorption spectroscopy (IRAS).[119], [120], [139], [155], [156] It was found that HCOOH dissociatively adsorbs above 160 K on (2×2)-NiO(111) to form adsorbed formate ($HCOO_{ad}$) and adsorbed H (which binds to a surface lattice O to make a surface hydroxyl, -OH), where the $HCOO_{ad}$ and -OH species were identified by IRAS. $HCOO_{ad}$ and -OH were found to be stable on (2×2)-

NiO(111)/Ni(111) surface until 320 K but undergo further reactions to form H_2 gas plus CO_2 gas (dehydrogenation path, TPD peaks at ~340, 390, and 520 K) and H_2O gas plus + CO gas (dehydration path, with TPD peaks at ~415 and 520 K).[156] We report here the first experimental measurement of the energy of the dissociative adsorption of formic acid on (2×2)-NiO(111) at 300 K by calorimetry. The differential heat of adsorption decreases with HCOOH coverage from 202 kJ/mol to 99 kJ/mol at saturation coverage (0.25 ML). The integral heat is 153 kJ/mol at saturation, which is ~36 kJ/mol higher than the integral heat of HCOOH dissociatively adsorbed on clean Ni(111) forming adsorbed bidentate formate and adsorbed hydrogen.[111] We also employed DFT to calculate the energies of the reaction and compare these to the calorimetric results to validate their energy accuracies. These results add substantially to our limited knowledge of the energy and structure of surface formate groups on oxide surfaces.

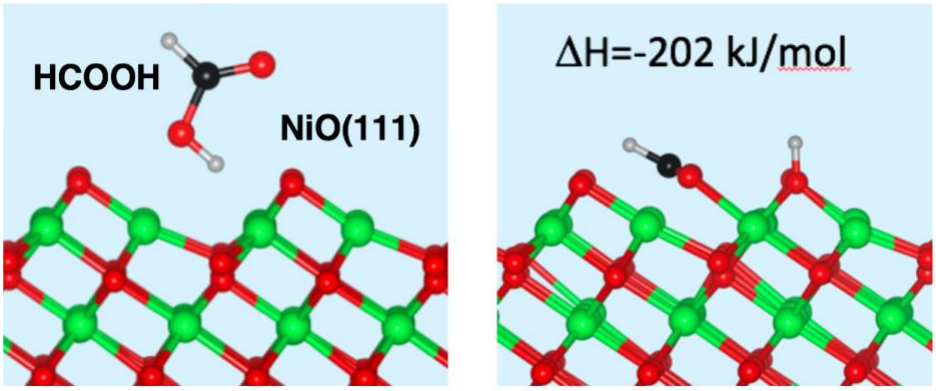

Figure 1. Schematic of formic acid dissociatively adsorbing onto NiO(111) as formate and hydroxyl

4.2 Experimental Methods

Experimental work was performed by Wei Zhao and Sawyer Morgan in the Campbell lab and is adapted here with permission from [148]. The experiments were performed in an ultrahigh vacuum (UHV) chamber (base pressure $<2 \times 10^{-10}$ mbar), designed for single-crystal adsorption

calorimetry (SCAC) and surface analysis, as described previously.[129], [130] Briefly, the chamber is equipped with low-energy electron diffraction (LEED), Auger electron spectroscopy (AES), X-ray photoelectron spectroscopy (XPS), low-energy ion scattering spectroscopy (LEIS), a quadrupole mass spectrometer (QMS) and a liquid-nitrogen-cooled quartz crystal microbalance (QCM). The Ni(111) sample used here is a 1 μm thick single-crystal foil, supplied by Jacques Chevallier at Aarhus University in Denmark and the surface was cleaned by cycles of Ar^+ ion sputtering and annealing. A detailed description of the experimental principles and implementation of the molecular beam flux, sticking probability, and heat measurements can be found elsewhere.[129]–[131] Before each calorimetry experiment, the clean Ni(111) was oxidized with a saturation exposure of O_2 (1×10^{-6} torr for 200 seconds) at 300 K, leading to an epitaxial NiO(111) film whose thickness is 3 or 4 bilayers.[157]–[160] As described before,[152] this gives a hydroxyl-free, octopolar reconstructed (2×2)-NiO(111) surface. Subsequently, the freshly prepared NiO(111) surface was exposed to a pulsed molecular beam of HCOOH at 300 K, and the adsorption heat and sticking probability were measured simultaneously. The beam was created by expanding ~2 mbar of HCOOH through a microchannel array and then collimated through a series of five liquid nitrogen cooled orifices, and chopped into 102 ms pulses every 5 s with a rotating chopper blade. The microchannel array was heated and kept at 360 K to reduce gas-phase dimerization to less than 1%.[132] The sticking probability was measured employing the King and Wells method,[161] whereby a QMS, non-line-of-sight to the sample, measured the transient increase in the background pressure of $HCOOH_g$ (m/e = 46) in the chamber versus time. We define the coverage of HCOOH molecules which adsorb onto the surface permanently in units of monolayers (ML) where 1 ML = 1.33×10^{19} atoms/m^2, the density of O atoms in a (hypothetically) unreconstructed NiO(111) surface.[159] A typical dose is 0.009

ML (~1.5×10^{12} molecules within the beam diameter of ~4 mm) per HCOOH pulse.

4.3 Theoretical Methods

Density functional theory (DFT) calculations to supplement and support our experiments were performed by our collaborator Andrew Doyle of the Nørskov group, with work here adapted from [148]. Using the Vienna *ab-initio* Software Package (VASP)[162]–[164] the dissociative adsorption of HCOOH on NiO(111) was simulated in six different configurations known from previous studies[152] as shown in Figure 4. Based on our previous study of dissociative adsorption of D_2O on this same NiO surface,[152] the HCOOH adsorption was studied on both the oxygen- and metal-terminated (2×2) octopolar surfaces of NiO(111), denoted as O-octo and M-octo, which are energetically most favored at preparation conditions of our experiment.[152] Only a single pair of O and Ni exposed sites are available within the (2×2) unit cell of each octopolar surface, which limits the saturated adsorption to a single HCOOH per (2×2) cell, which we refer to as 0.25 ML coverage. Subsequently, we have studied HCOOH adsorption under 1/16, 1/8, 3/16 and at 1/4 ML coverages using any the four equivalent adsorption sites within our (4×4) simulation cell.

The model systems are symmetric stoichiometric NiO slabs six layers of nickel atoms thick that are separated by at least 15Å of vacuum in the *z* direction and they are periodic in the *xy* plane (using a 2×2 supercell and 2x2 Γ-centered *k*-point mesh). We have used the spin-polarized PBE exchange-correlation functional[165] with a Hubbard U (+U) correction[166] of 6.45 eV on Ni atoms to account for on-site correlation effects, and we note that this level of theory has been used successfully for similar problems in the literature.[152], [167]–[169] We have also tested the effect of other exchange-correlation functionals commonly employed in catalysis such as

RPBE[170] and BEEF-vdW.[171]

The core electrons of carbon, nickel, and oxygen atoms are modeled with projector augmented wave (PAW) pseudopotentials from the VASP library, notably not using the "soft" option for C or O.[172] A plane wave basis was employed with a cutoff of 550 eV with a full FFT-grid setting to accurately describe valence electrons. The positions of all atoms within the unit cell were relaxed until the force on each atom was less than 0.02 eV*Å^{-1}. The surfaces, including for structures with adsorbed HCOOH, readily adopt the AFM-type II antiferromagnetic ordering along {111} direction, layers of Ni-ions with alternating sign and with absolute value of magnetic moments of ~1.7 μ_B per Ni atom.

The heat of adsorption q is defined for the experimental measurements as the negative of the enthalpy change upon adsorption (ΔH). We calculate the theoretical integral heat of adsorption as the sum of the changes in electronic energy at T=0 K (ΔE_{DFT}), zero-point energy (ΔE_{ZPE}), harmonic heat capacity energies $(C\Delta T)$ and change in the pressure-volume term $(\Delta(PV) = -PV_{gas} = -RT)$ when a formic acid molecule adsorbs (and dissociates in this case) on the catalyst surface:

$$q = -\Delta H = -[(E_{DFT} + ZPE + C\Delta T)_{Ads.+surf.} - E_{Clean} - (E_{DFT} + ZPE + C\Delta T)_{HCOOH}] + RT$$

Here "Ads.+surf." refers to the combined system of catalyst with bound adsorbate, "Clean" refers to the pristine catalyst surface, and "HCOOH" refers to the gas phase formic acid molecule. The sign convention here matches experiment. We assume that the vibrations within the catalyst surface itself are only perturbed slightly by the adsorbate, so we do not consider the contribution of atoms within the oxide surface towards the zero-point energy or harmonic heat capacity. The contributions from adsorbed and gas-phase vibrations almost exactly cancel in all cases, as shown in Table 1.

Table 1: Thermochemistry corrections used to convert between calculated electronic energies and binding energies at a coverage of 1/16 ML using PBE+U. Values are rounded to the nearest kJ/mol.

Termination	**Binding Site**	$(ZPE + C\Delta T)_{Ads} - (ZPE + C\Delta T)_{HCOOH}$ [kJ/mol]	-RT (300K) [kJ/mol]
O-Octo	Bridging	2.2	-2.5
	Hex-Bridging	2.5	-2.5
	Monodentate	1.9	-2.5
M-Octo	Bidentate	3.1	-2.5
	Bridging	2.3	-2.5

4.4 Experimental Results

4.4.1 Sticking Probability

The short-term and long-term sticking probabilities of HCOOH adsorbing on (2×2)-NiO(111) were measured at 300 K, as shown in Figure 1. The short-term sticking probability (S_{102ms}) is the probability that a gas molecule strikes the sample surface, sticks, and remains at least throughout the time window of our heat measurement (i.e., the first 102 ms). This is used to calculate the number of moles of gas-phase reactant that contribute to the measured heat of adsorption. The long-term sticking probability (S_∞) is the probability that a gas molecule strikes the sample surface, sticks, and remains until the next gas pulse starts ~5 s later, which is used to calculate the adsorbate coverage remaining at the start of the next gas pulse. The long-term sticking probability starts at ~0.86, then quickly increases to ~0.97 and keeps almost unity until ~0.23 ML, where it starts to drop sharply and reaches 0 at ~0.25 ML. The short-term sticking probability follows a very similar trend, but stops dropping at a value of ~0.5 for the saturated

adlayer at 0.25 ML. This indicates that ~50% of HCOOH gas molecules in each pulse transiently adsorb on the saturated surface, but desorb again slowly before the next pulse arrives. The saturation coverage of 0.25 ML is consistent with one HCOOH molecule adsorbing (dissociatively) per unit cell on the p(2×2) octopolar surface structure of NiO(111) studied here.

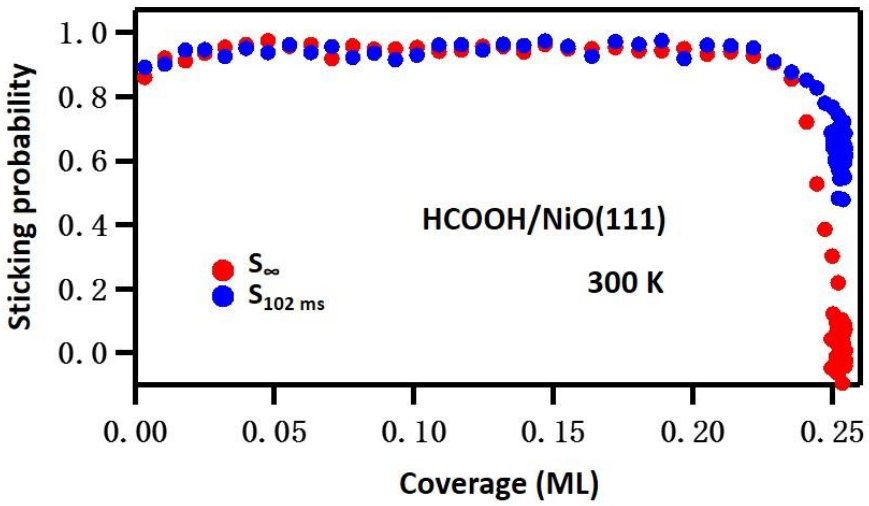

Figure 2. Long-term (S_{∞}: in red) and short-term ($S_{102\ ms}$: in blue) sticking probabilities of HCOOH on (2×2)-NiO(111) as a function of the total HCOOH coverage that adsorbed at 300 K. One ML is defined as 1.33×10^{19} adsorbed HCOOH molecules per m^2, in this case being dissociatively adsorbed.

4.4.2 Heat of Adsorption

In this paper, we define the term *heat of adsorption* as the negative of the differential standard molar enthalpy change for the adsorption reaction, with the gas and the sample surface being at the same temperature. As described previously, this requires a small correction on the gas temperature compared to the actual experimental molecular beam conditions.[131]

According to the literature,[119], [120], [139], [155], [156] HCOOH is known to dissociatively adsorb on (2×2)-NiO(111)/Ni(111) at 300 K, forming $HCOO_{ad}$ and H_{ad} (which binds to a lattice O, so it forms a surface –OH). Figure 3 shows the measured differential heat of

adsorption vs HCOOH coverage until saturation at ~0.25 ML. The differential heat drops almost linearly with coverage from an initial value of ~202 kJ/mol down to a final value of ~99 kJ/mol at the saturated coverage of 0.25 ML. The integral heat is 153 ± 3 kJ/mol at 0.25 ML (the error here is the run-to-run standard deviation, associated with run-to-run errors in the absolute heat-detector calibration factor). This integral heat is ~36 kJ/mol higher than that for HCOOH dissociative adsorption on clean Ni(111) forming adsorbed bidentate formate and adsorbed hydrogen.[111] After saturation, HCOOH molecules continue to adsorb with S_{102ms} = ~0.5, but desorb again before the next gas pulse (see Figure 1). The heat value for this transiently-adsorbed HCOOH after saturation is 99 ± 3 kJ/mol. The red line in Figure 3 is the best fit to the differential heat data points and has and y-intercept of 202 kJ/mol and a slope of –399 kJ/mol/ML.

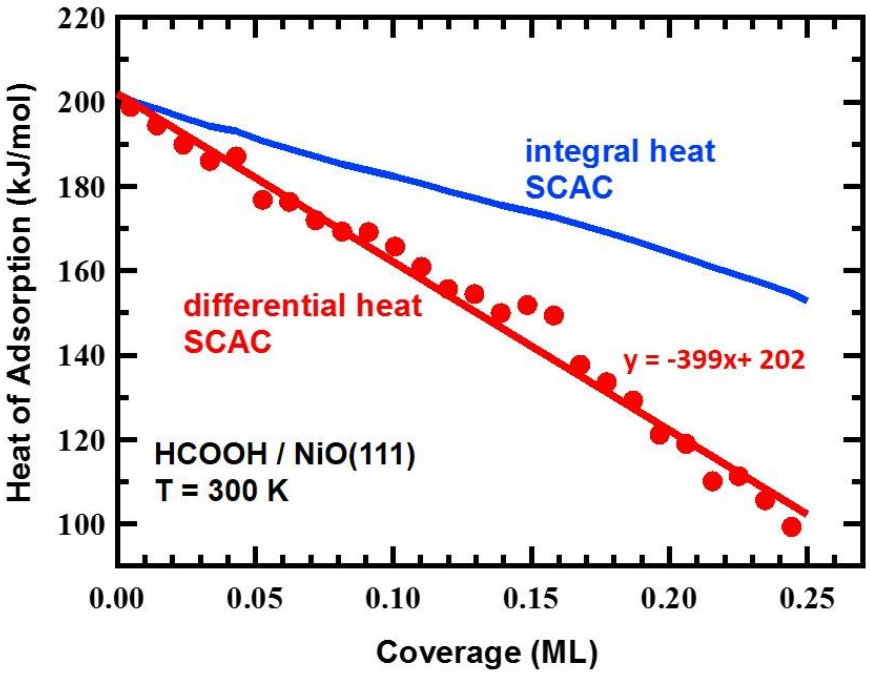

Figure 3. Differential heat of dissociative adsorption (-ΔH) of HCOOH on (2×2)-NiO(111) at 300 K versus the total coverage of dissociatively adsorbed HCOOH measured by calorimetry (SCAC, red data points). The red line shown is the best linear fit to the differential heat data points and has a y-intercept of 202 kJ/mol and a slope of -399 (kJ/mol)/ML. The integral heat for

the dissociatively adsorbed HCOOH is also plotted versus HCOOH coverage (the blue curve), giving 153 ± 3 kJ/mol at 0.25 ML.

We also measured the heat of adsorption at 100 K, shown as Figure 4, where HCOOH molecularly adsorbs on (2×2)-NiO(111)/Ni(111) according to the literature.[120], [155] The differential heat of adsorption is initially ~90 kJ/mol, and keeps almost constant until ~0.14 ML. That initial heat is ~11 kJ/mol higher than the initial heat of HCOOH molecularly adsorbed on Ni(111),[111] indicating that HCOOH molecularly adsorbs on NiO(111) more strongly than on Ni(111). After 0.14 ML, the heat decreases quickly to ~55 kJ/mol at ~0.25 ML and more slowly to ~51 kJ/mol at ~0.5 ML, and finally remains constant at 50.4 ± 2.3 kJ/mol beyond 0.5 ML, where the multilayers of formic acid are built up on surface. This final heat is consistent with the heat of adsorption of multilayer formic acid on Pt(111)[116] and Ni(111)[111] reported by this group previously. The sticking probability at 100 K was near unity at all coverages.

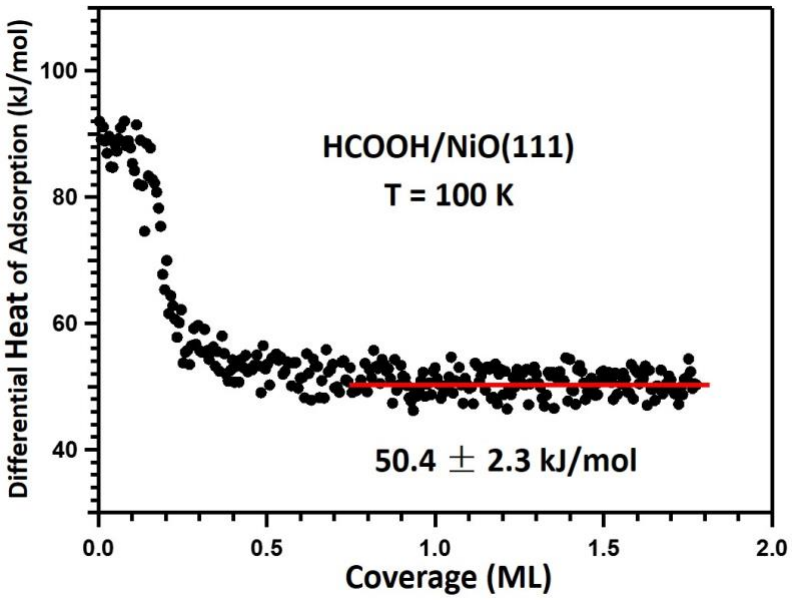

Figure 4: Differential heat of molecular adsorption of HCOOH on (2×2)-NiO(111) at 100 K versus the total coverage of molecularly adsorbed HCOOH measured by calorimetry.

4.5 Theoretical Results

4.5.1 Calculated Energetics of HCOOH Dissociative Adsorption

The DFT work by collaborator Andrew Doyle considered six different adsorption configurations for the formate and H products of HCOOH dissociation, spanning both O-octo and M-octo surface terminations using DFT+U method (see also Theoretical Methods), as shown in Figure 5. The final optimized structures of adsorbed $HCOO_{ad}$ were found to bind to the surface through one or both of its oxygens. We borrow terminology from Ref. [139]: in the "bidentate" configuration, both oxygens in $HCOO_{ad}$ bind to one nickel atom, in "monodentate" configurations one oxygen in $HCOO_{ad}$ binds to a nickel atom while the other forms a hydrogen bond to the dissociated hydrogen, and in "bridging" configurations each oxygen in $HCOO_{ad}$ binds to different nickel atoms. "Hex-bridging" follows the same principles as bridging, but binds to two upmost nickel atoms in a symmetric fashion. In all cases, the H product was found to form OH group at the nearby surface O^{2-} of the NiO lattice, confirming the basic character of the oxide surface's oxygen anion, as seen previously for MgO surfaces.[173]

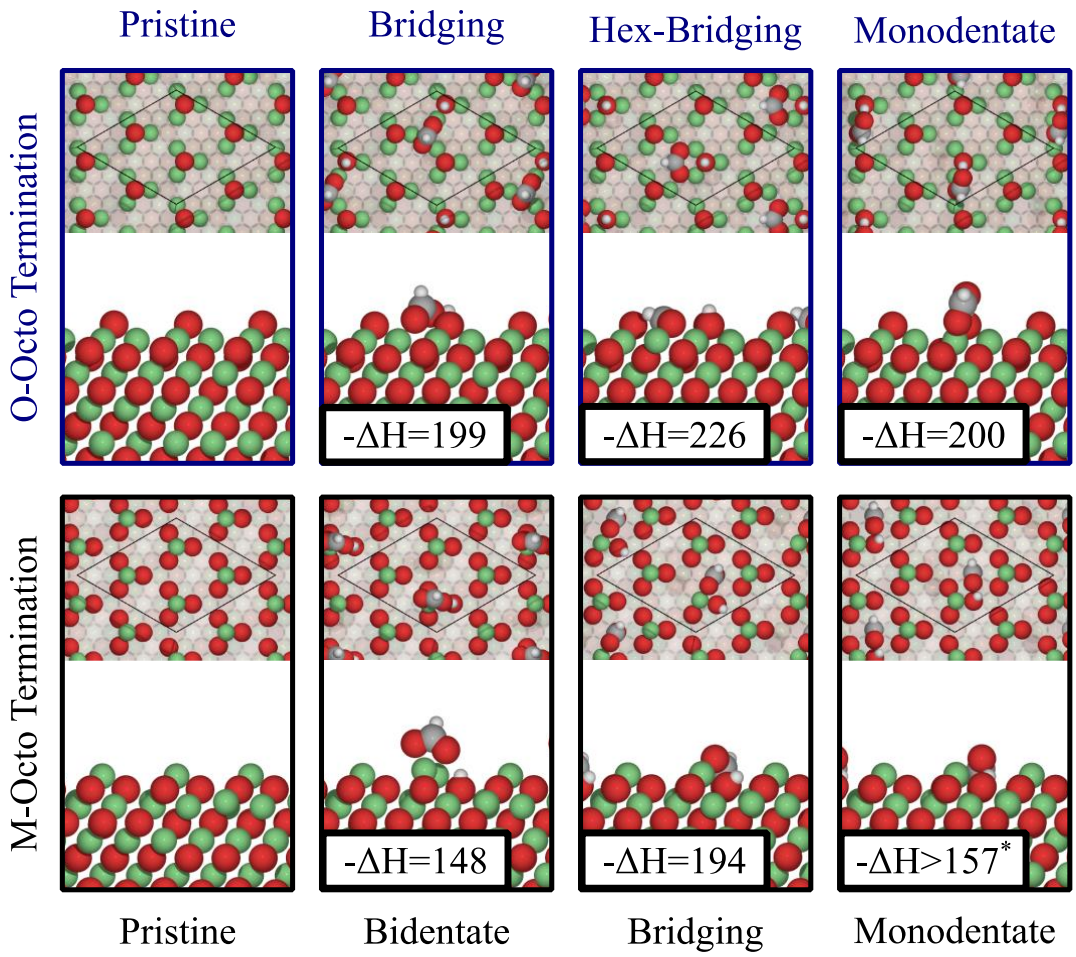

Figure 5. DFT calculated integral heats of dissociative adsorption of HCOOH (-ΔH, in kJ/mol) and resulting optimized surface structures for different adsorption configurations of formate (Bidentate, Bridging, Hex-Bridging, Monodentate) at low coverage. Calculated adsorption energies (in kJ/mol) shown in the lower-left for both the O- and M- terminated (O-octo and M-octo) (2×2)-NiO(111) surfaces, at 1/16 ML coverage, obtained using PBE+U DFT. In these calculations, the monodentate adsorption configuration on M-octo surfaces is only stable at 0.25 ML coverage. At lower coverages, it is metastable, and reverts to a bridging configuration.

First, we highlight the similarity between the most stable configurations' energetics from Figure 5 for each termination at the low-coverage limit: -226 kJ/mol (O-octo hex-bridging), -195 kJ/mol (M-octo bridging) and the experimentally measured value in the -202 kJ/mol. Both calculated values are relatively close to experimentally measured value, which suggests that we are describing the dominant interactions between the $HCOO_{ad}$, H_{ad}, and (2×2)-NiO(111)

appropriately. Additionally, both types of surface terminations have similar adsorption energetics and therefore their simultaneous presence in experimental samples cannot be eliminated as a possibility by comparison to the experimental heats. This is also a test of the calculated surface energies of these two surface terminations when clean (before adsorption), which we found to be identical within expected error bars of the calculation.[152] Another important finding from our calculations is that the bridging geometries for $HCOO_{ad}$ are always energetically preferred over monodentate and bidentate type bonding. Additionally, we also demonstrate in Table 2 that the calculated vibrational eigenmode frequencies of bridge-bonded formate structures for both terminations compare favorably to previous experimental values using infrared spectroscopy.[155]

Table 2: Vibrational eigenmodes observed in experiment (Ref. [155]) and calculated using DFT. Calculated results include IR-silent modes, and were determined by fits to harmonic potentials. Calculated modes with wavenumbers within 100 cm^{-1} of an experimentally observed peak are bolded.

Experiment (cm^{-1} ; Ref. [155])	M-Octo Bidentate (cm^{-1})	M-Octo Bridging (cm^{-1})	O-Octo Bridging (cm^{-1})	O-Octo Hex-Bridging (cm^{-1})	O-Octo Monodentate (cm^{-1})
778	61	119	40	134	72
1360	87	162	135	149	129
1570	106	226	171	219	147
2860	231	276	200	275	232
	270	321	246	314	244
	311	340	261	333	338
	733	595	524	544	**748**
	766	**739**	**709**	638	896
	782	**766**	**743**	**742**	990
	1005	1005	1010	1012	1015
	1281	1228	**1323**	**1313**	1249
	1343	**1344**	**1331**	**1332**	**1336**
	1540	**1567**	**1528**	**1521**	**1618**
	2959	**2935**	**2960**	**2937**	**2950**
	3552	3453	3647	3670	2992

Next, in Figure 6, we show the calculated integral adsorption enthalpy (ΔH) on both the O-octo and M-octo terminations as function to coverage up to ¼ ML. The O-octo surface (shown in red) clearly adsorbs $HCOO_{ad}$ and H_{ad} more strongly than the M-octo surface (shown in blue) for all bonding modes. For the O-octo surface, the calculated integral ΔH is constant or an increasing function of the coverage which is in contrast with the strong decrease seen in the experimental calorimetry results shown in Figure 3. The M-octo surface shows configurations where the calculated integral ΔH is a decreasing function of the coverage and generally much closer to the experimental line at all considered coverages. Introducing a metallic Ni(111) support below the oxide film or mixed adsorbate configurations at ¼ ML did not change the calculated trends for the O-octo surface (shown as Figure 7). Calculations at coverages up to ¼ ML are therefore essential in order to capture the adsorption energetics on NiO(111) surfaces. Furthermore, DFT also shows that dissociative adsorption is much less favorable at coverages above ¼ ML due to unavailability of free adsorption sites which also agrees with saturation observed in our experiment.

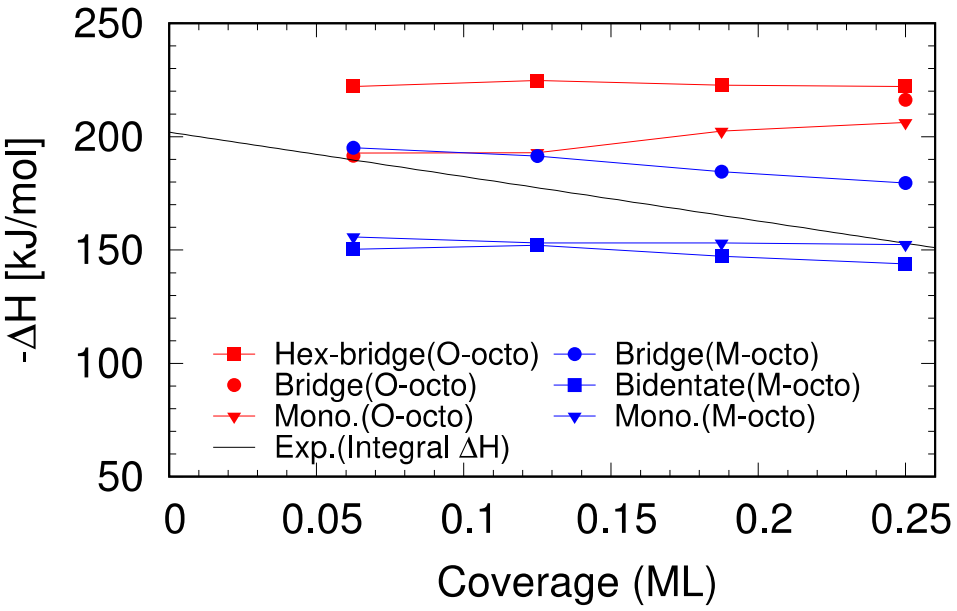

Figure 6: Calculated ΔH of adsorption at 0 K for all possible types of dissociative HCOOH adsorption as function of HCOOH coverage from 1/16 ML to 1/4 ML on O-octo (red symbols) and M-octo (blue symbols). The experimental measurement at 300 K is also shown for comparison (solid black line). Due to computational limitations, here we used a less expensive 400 eV cut-off for our plane wave basis together with softer potentials for oxygen and carbon. These results deviate less than 3 kJ/mol from more accurate values obtained at 550 eV plane wave cut off at low coverage.

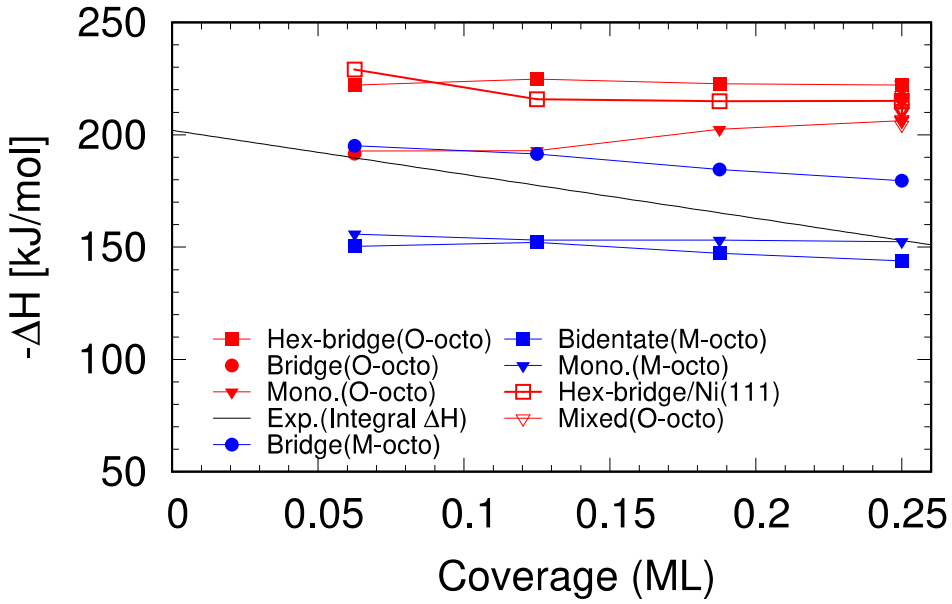

Figure 7: Same as Figure 6 with extra points considering Ni(111) metal supported O-octo surface (open squares) and mixing of various adsorbate modes on O-octo (open triangles).

Lastly, we have also tested the influence of changing the Hubbard (+U) parameter and the exchange-correlation functional on our results. We found no qualitative difference in the relative stabilities of structures for any of the cases tested, as shown in Figure 8. Increasing the value of the U-parameter leads to weaker adsorption, while decreasing the U-parameter leads to increasing the adsorption in agreement with our previous study for D_2O adsorption on this same surface.[152] We further show that changing the exchange-correlation functional does not substantially alter calculated adsorbate-adsorbate interactions in Figure 9.

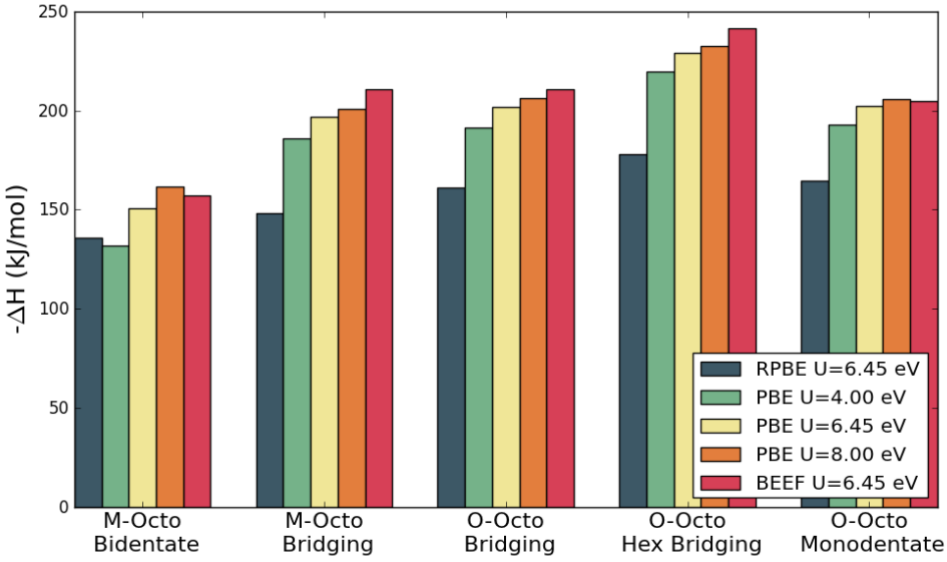

Figure 8: Comparison of calculated adsorption energies at 0 K and a coverage of 1/16 ML for each site using different exchange-correlation functionals and values of the Hubbard (+U) term on Ni 3d orbitals. All calculations use the PBE the lattice constant, zero point energies, and heat capacities found using PBE with U=6.45, though their atomic coordinates are relaxed independently.

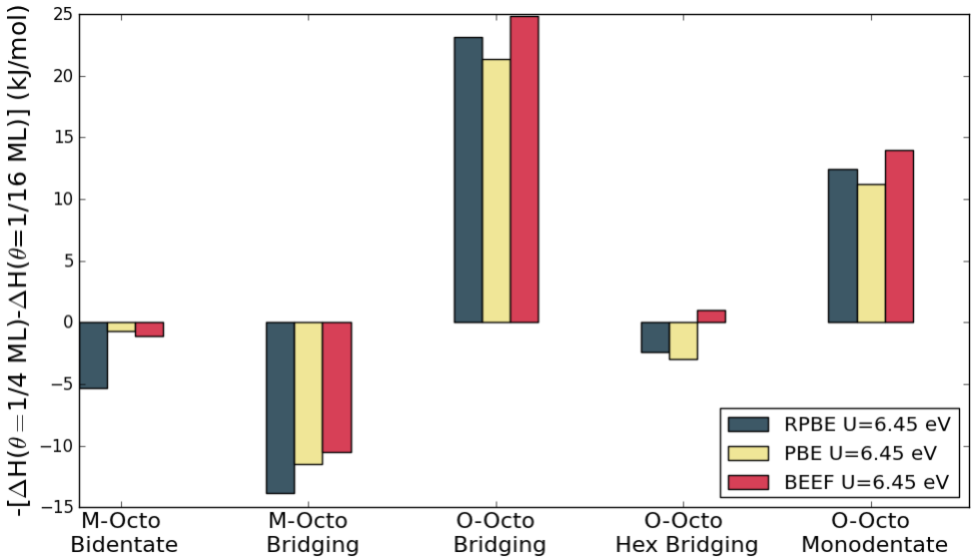

Figure 9: Comparison of the calculated integral heats of adsorption at two different coverages (1/4 ML and 1/16 ML) using different exchange-correlation functionals. All calculations use the PBE the lattice constant, zero point energies, and heat capacities found using PBE with U=6.45 and a coverage of 1/16 ML, though their atomic coordinates are relaxed independently.

4.5.2 Discussion of Theory vs. Experiment

We find good agreement between theory and experiment at low coverages of dissociatively adsorbed HCOOH, where the experimentally observed value for differential heat of adsorption is consistent with adsorption energetics calculated at either O-octo (2×2) or M-octo (2×2) surfaces. The largest decrease in heat of adsorption with coverage is observed for a bridge-bonded geometry of formate on the M-octo surface, where the integral heat drops from 195 kJ/mol at low coverage to 180 kJ/mol at 0.25 ML. This 15 kJ/mol decrease indicates that repulsive electronic adsorbate-adsorbate interactions are present in this system, but do not account for the full ~45 kJ/mol decrease shown in Figure 3. Adsorbate-adsorbate repulsion for these molecules typically arises either due to dipole-dipole interactions or substrate mediated interactions. For the O-octo surface, we have tested separately the effect of mixed adsorption modes and the effect of Ni(111) metallic support, both of which had only small effects on the

adsorption energy at high coverage (See Figure 7). Furthermore, the calculated trends were independent of the choice of exchange-correlation functional or choice of Hubbard-U (see Figure S3).

The discrepancy of DFT predictions with experimental measurement on the other hand can be more simply explained if we would allow for the presence of both types of terminations on the clean surface of our experimental sample. In this picture, the mixture of O-octo and M-octo surfaces would be exposed to the adsorption of HCOOH molecules. At low coverage, the most energetically favorable hex-bridging geometry on the O-octo surface (-ΔH=226 kJ/mol) would dominate the adsorption. This assumes that the un-dissociated HCOOH is mobile on the surface and finds sites with the lowest barrier and are also the most exothermic for dissociation assuming BEP scaling relations.[174] Only after all available O-octo sites are filled, the M-octo sites could adsorb preferentially in the bridge geometry (-ΔH=180 kJ/mol). For some fraction f of the surface area being O-octo (and thus 1-f as M-octo), the integral -ΔH at ¼ ML would therefore equal $f * 226 + (1 - f) * 180$ kJ/mol. For a 50/50 mixture of O-octo to M-octo, the final integral heat would drop from 226 to 203 kJ/mol, or 23 kJ/mol lower ΔH relative to low coverage. Higher area fractions of M-octo would therefore effectively lower the adsorption energetics at high coverage, closer to measured ~45 kJ/mol decrease.

4.6 Conclusions

In this study, we have used calorimetric measurements and density functional theory to examine the energetics of formic acid dissociatively adsorbed on a (2×2)-NiO(111) surface. They agree with each other quite well at the limit of low coverage of adsorbates. However, we find that experiments show a clear downward trend in adsorption energies at higher coverages,

while calculations suggest this is not a straightforward case of electronic adsorbate-adsorbate repulsion. We inferred that the decreased binding strength may be indicative of heterogeneous adsorption at the (2×2)-NiO(111) surface, with respect to oxygen- and metal-termination both being present on the starting surface, and/or binding site differences. We confirm that all calculated configurations considered show similar energetics and vibrational spectra at low coverage (see Table 1). These findings provide a more detailed understanding of the system studied, and underscore the importance of combined experimental and DFT-based approaches to understanding the catalysis of transition-metal oxides.

Chapter 5: Conclusions and implications

The preceding experiments showed improved understanding of the ferromagnetic metals iron and nickel, namely in iron's use as a shape memory alloy and nickel's use as a catalytic surface. Both materials' functionality derives from the valence *d* electrons which provide for reactivity and magnetostriction. Iron alloyed with 30% palladium has an electronic spin structure that allows for the alignment of magnetic moments in unit cells under a magnetic field, resulting in a shift in the lattice structure from austenite to martensite as magnetostrictive strain. This phase change can also be exhibited at low temperatures and in conjunction with stress. A synthesis pathway for electrodeposition and annealing of nanowires was developed that successfully produced $Fe_{70}Pd_{30}$ with length 2–3 μm and diameter 200 nm. X-ray diffraction showed the presence of multiple crystal phases present, so the initial samples had inhomogeneities that inhibited the low-temperature phase transition. Later samples were fully in the austenite phase, but sufficiently low temperatures were not achievable at the available X-ray facilities needed for nanoscale phase transitions. The transition temperature should also be able to be modulated with respect to changing levels of residual stress, but cryogenic x-ray capabilities such as those at SPring-8 in Japan may be necessary as well.

Successfully processed $Fe_{70}Pd_{30}$ nanowires in alumina template with pure austenite phase should be further investigated to more precisely determine the effect of nano-size on phase transition temperature and its interplay with residual stress. Additional access to helium-cooled XRD should provide useful data on constructing the phase diagram provided that the phase transition occurs above this temperature, following the literature. This would be followed by application of magnetic field from Helmholtz coil to understand the three-dimensional phase

diagram to determine how all three components relate for possible applied uses. This can then be applied to nanohelices formed in a polymer nanoconfinement template. For biomedical applications, a method of surface modification should be implemented with zwitterionic linker for compatibility and hydrophilicity.

As this dissertation has shown, it is extremely challenging to simultaneously control composition, stress, and phase purity of electrodeposited nanomaterials. This is especially true for ferromagnetic alloys, given their low deposition potentials where RXN (2) can interfere in many aspects of the processing. It is important to note, however, that technological examples exist in high-value manufacturing where this sort of precise control has been achieved using electrodeposition. For example, the most widely used electrodeposited ferromagnetic alloys are in the manufacture of write-heads for hard disk drive assemblies sold globally at the billion unit scale. Tailoring the electrolytes (additives, temperatures, deposition conditions, etc.) and deposition tools (control, mixing, testing) was a decades-long academic and corporate effort that has grown into a major global supply chain. Of course, the ferromagnetic shape memory alloy used here has an added complexity of requiring thermal annealing and quenching into a particular metastable phase. Thus, it remains an open theoretical and experimental question whether the combination of phase pure nanostructures and controlled residual stresses can be used to tune the ferromagnetic shape memory alloys transition temperature toward the required 37˚C needed for use as therapeutic nanorobots, but there is reason to continue pushing for the kinds of systematic materials advances presented here.

The (111) surface of nickel and nickel oxide was studied to better understand its energetics of adsorption. Our results explicate the reactivity with formic acid, showing the heat of adsorption on both surfaces at various temperatures. We find that at lower temperatures

formic acid adsorption is molecular, continuing to form multilayers after surface saturation is reached, while at higher temperatures, adsorption is dissociative, binding as hydrogen and formate in either bidentate or monodentate configurations. Formic acid binds more strongly to nickel oxide (111) than to nickel (111), which is likewise stronger than on Pt (111), as nickel's oxidation state and nickel oxide's acid-base sites allow for more efficient configurations.

This provides benchmarks for better DFT calculations and builds on previous experimental work with adsorption of water, methyl iodide, methanol, benzene, and phenol on nickel, nickel oxide, iron oxide, and platinum (111) surfaces. Future work should examine formic acid adsorption and dissociation on copper, cobalt, and other widely used catalytic transition metals with free *d* electrons. Although formic acid is representative of carboxylic acids, it may be informative to also study acetic acid and carbonic acid, which may have different likelihoods of dissociation and varied packing on the surface. It would also be beneficial to study adsorption on nickel and nickel oxide's other surfaces beyond (111), as they would also be present in the catalyst material.

References

[1] Y. Okamoto, “Surface state and catalytic activity and selectivity of nickel catalysts in hydrogenation reactions III. Electronic and catalytic properties of nickel catalysts,” *J. Catal.*, vol. 64, no. 2, pp. 397–404, Aug. 1980.

[2] C. H. Bartholomew and R. J. Farrauto, *Fundamentals of Industrial Catalytic Processes: Second Edition*, 2nd ed. Wiley, 2010.

[3] A. Fürstner, “Iron Catalysis in Organic Synthesis: A Critical Assessment of What It Takes To Make This Base Metal a Multitasking Champion,” *ACS Cent. Sci.*, vol. 2, pp. 778–789, 2016.

[4] C. Bolm, J. Legros, J. Le Paih, and L. Zani, “Iron-Catalyzed Reactions in Organic Synthesis,” 2004.

[5] J. Rossmeisl, G. S. Karlberg, T. Jaramillo, and J. K. Nørskov, “Steady state oxygen reduction and cyclic voltammetry,” *Faraday Discuss.*, vol. 140, no. 0, pp. 337–346, Oct. 2008.

[6] B. Hammer and J. K. Norskov, “Why gold is the noblest of all the metals,” *Nature*, vol. 376, no. 6537, pp. 238–240, Jul. 1995.

[7] J. K. Nørskov, T. Bligaard, J. Rossmeisl, and C. H. Christensen, “Towards the computational design of solid catalysts,” *Nature Chemistry*, vol. 1, no. 1. pp. 37–46, Apr-2009.

[8] J. R. Kitchin, J. K. Nørskov, M. A. Barteau, and J. G. Chen, “Role of strain and ligand effects in the modification of the electronic and chemical Properties of bimetallic surfaces,” *Phys. Rev. Lett.*, vol. 93, no. 15, p. 156801, Oct. 2004.

[9] X. Wang, Q. He, L. Song, M. Jaroniec, Y. Zheng, and S. Z. Qiao, “Breaking the volcano-plot limits for Pt-based electrocatalysts by selective tuning adsorption of multiple intermediates,” *J. Mater. Chem. A*, vol. 7, no. 22, pp. 13635–13640, Jun. 2019.

[10] P. Quaino, F. Juarez, E. Santos, and W. Schmickler, “Volcano plots in hydrogen electrocatalysis-uses and abuses,” *Beilstein J. Nanotechnol.*, vol. 5, no. 1, pp. 846–854, 2014.

[11] H. Toulhoat, P. Raybaud, V. Mendez, and E. Puzenat, “A universal relationship predicts optimal catalysts for a given chemical reaction,” 2018.

[12] E. Santos, P. Hindelang, P. Quaino, E. N. Schulz, G. Soldano, and W. Schmickler, “Hydrogen Electrocatalysis on Single Crystals and on Nanostructured Electrodes,” *ChemPhysChem*, vol. 12, no. 12, pp. 2274–2279, Aug. 2011.

[13] S. B. Simonsen, D. Chakraborty, I. Chorkendorff, and S. Dahl, “Alloyed Ni-Fe nanoparticles as catalysts for NH3 decomposition,” *Appl. Catal. A Gen.*, vol. 447–448, pp. 22–31, Dec. 2012.

[14] X. Duan *et al.*, “Ammonia decomposition on Fe(1 1 0), Co(1 1 1) and Ni(1 1 1) surfaces: A density functional theory study,” *J. Mol. Catal. A Chem.*, vol. 357, pp. 81–86, May 2012.

[15] G. S. Selwyn and M. C. Lin, “Production of the NH radical from the catalytic decomposition of NH3 on polycrystalline Pt and Fe surfaces at high temperatures,” *Chem. Phys.*, vol. 67, no. 2, pp. 213–220, May 1982.

[16] J. Zhang, H. Xu, and W. Li, “Kinetic study of NH3 decomposition over Ni nanoparticles: The role of la promoter, structure sensitivity and compensation effect,” *Appl. Catal. A*

Gen., vol. 296, no. 2, pp. 257–267, Dec. 2005.
[17] Z. Liu, S. Yao, A. Johnston-Peck, W. Xu, J. A. Rodriguez, and S. D. Senanayake, "Methanol steam reforming over Ni-CeO2 model and powder catalysts: Pathways to high stability and selectivity for H2/CO2 production," *Catal. Today*, vol. 311, pp. 74–80, Aug. 2018.
[18] K. Chuasiripattana, O. Warschkow, B. Delley, and C. Stampfl, "Reaction intermediates of methanol synthesis and the water-gas-shift reaction on the ZnO(0001) surface," *Surf. Sci.*, vol. 604, no. 19–20, pp. 1742–1751, Sep. 2010.
[19] D. W. Flaherty, W. Y. Yu, Z. D. Pozun, G. Henkelman, and C. B. Mullins, "Mechanism for the water-gas shift reaction on monofunctional platinum and cause of catalyst deactivation," *J. Catal.*, vol. 282, no. 2, pp. 278–288, Sep. 2011.
[20] L. C. Grabow, A. A. Gokhale, S. T. Evans, J. A. Dumesic, and M. Mavrikakis, "Mechanism of the water gas shift reaction on Pt: First principles, experiments, and microkinetic modeling," *J. Phys. Chem. C*, vol. 112, no. 12, pp. 4608–4617, Mar. 2008.
[21] A. Tullo, "Why Chemical Makers Have Their Eyes On Formic Acid," *Chemical & Engineering News*, 2015.
[22] G. Peng, S. J. Sibener, G. C. Schatz, S. T. Ceyer, and M. Mavrikakis, "CO 2 hydrogenation to formic acid on Ni(111)," *Journal of Physical Chemistry C*, vol. 116, no. 4. pp. 3001–3006, 02-Feb-2012.
[23] T. Devine, "Why don't magnets work on some stainless steels?," *Scientific American*, 2006.
[24] H. D. Arnold and G. W. Elmen, "Permalloy, A New Magnetic Material of Very High Permeability," *Bell Syst. Tech. J.*, vol. 2, no. 3, pp. 101–111, Jul. 1923.
[25] A. A. Chlenova, A. A. Moiseev, M. S. Derevyanko, A. V. Semirov, V. N. Lepalovsky, and G. V. Kurlyandskaya, "Permalloy-based thin film structures: Magnetic properties and the giant magnetoimpedance effect in the temperature range important for biomedical applications," *Sensors (Switzerland)*, vol. 17, no. 8, Aug. 2017.
[26] A. T. English and G. Y. Chin, "Metallurgy and magnetic properties control in permalloy," *J. Appl. Phys.*, vol. 38, no. 3, pp. 1183–1187, Mar. 1967.
[27] R. M. Bozorth, "The permalloy problem," *Rev. Mod. Phys.*, vol. 25, no. 1, pp. 42–48, Jan. 1953.
[28] E. Klokholm and J. A. Aboaf, "The saturation magnetostriction of permalloy films," *J. Appl. Phys.*, vol. 52, no. 3, pp. 2474–2476, Mar. 1981.
[29] P. James, O. Eriksson, O. Hjortstam, B. Johansson, and L. Nordström, "Calculated trends of the magnetostriction coefficient of 3 d alloys from first principles," *Appl. Phys. Lett.*, vol. 76, no. 7, pp. 915–917, Feb. 2000.
[30] J. H. Van Vleck, "On the anisotropy of cubic ferromagnetic crystals," *Phys. Rev.*, vol. 52, no. 11, pp. 1178–1198, Dec. 1937.
[31] I. A. Campbell, "The linear magnetostriction of ferromagnetic transition metals," *Solid State Commun.*, vol. 10, no. 10, pp. 953–955, May 1972.
[32] J. W. Brooks and P. J. Bridges, "Metallurgical Stability of Inconel Alloy 718," 1988, pp. 33–42.
[33] J. S. Smith and K. A. Heck, "Development of a Low Thermal Expansion Crack Growth Resistant Superalloy," *Superalloys*, p. 91, 1996.
[34] P. Hidnert, "Thermal Expansion of Some Nickel Alloys," *J. Res. Natl. Bur. Stand. (1934).*, vol. 58, no. 2, pp. 89–92, 1957.

[35] M. Sundararaman and P. Mukhopadhyay, “Overlapping of γ′′ precipitate variants in Inconel 718,” *Mater. Charact.*, vol. 31, no. 4, pp. 191–196, Dec. 1993.
[36] M. Shiga, “Invar alloys,” *Curr. Opin. Solid State Mater. Sci.*, vol. 1, no. 3, pp. 340–348, Jun. 1996.
[37] M. Van Schilfgaarde, I. A. Abrikosov, and B. Johansson, “Origin of the invar effect in iron-nickel alloys,” *Nature*, vol. 400, no. 6739, pp. 46–49, Jul. 1999.
[38] R. D. James and M. Wuttig, “Magnetostriction of martensite,” *Philos. Mag. A Phys. Condens. Matter, Struct. Defects Mech. Prop.*, vol. 77, no. 5, pp. 1273–1299, May 1998.
[39] T. Sakamoto, T. Fukuda, T. Kakeshita, T. Takeuchi, and K. Kishio, “Magnetic field-induced strain in iron-based ferromagnetic shape memory alloys,” in *Journal of Applied Physics*, 2003, vol. 93, no. 10 3, pp. 8647–8649.
[40] P. J. Webster, K. R. A. Ziebeck, S. L. Town, and M. S. Peak, “Magnetic order and phase transformation in Ni2MnGa,” *Philos. Mag. B Phys. Condens. Matter; Stat. Mech. Electron. Opt. Magn. Prop.*, vol. 49, no. 3, pp. 295–310, 1984.
[41] C. A. Jenkins *et al.*, “Growth and magnetic control of twinning structure in thin films of Heusler shape memory compound Ni2 MnGa,” *Appl. Phys. Lett.*, vol. 93, no. 23, p. 234101, Dec. 2008.
[42] E. Denkhaus and K. Salnikow, “Nickel essentiality, toxicity, and carcinogenicity,” *Critical Reviews in Oncology/Hematology*, vol. 42, no. 1. Elsevier, pp. 35–56, 01-Apr-2002.
[43] Y. Ma, M. Zink, and S. G. Mayr, “Biocompatibility of single crystalline Fe70Pd30 ferromagnetic shape memory films,” *Appl. Phys. Lett.*, vol. 96, no. 21, p. 213703, May 2010.
[44] D. R. Reynolds, “A Nonlinear Thermodynamic Model for Phase Transitions in Shape Memory Alloy Wires,” 2003.
[45] D. Vokoun, J. C. Shih, T. S. Chin, and C. T. Hu, “Magnetic properties of Fe-∼30 at% Pd films,” *J. Magn. Magn. Mater.*, vol. 281, no. 1, pp. 105–109, Oct. 2004.
[46] M. Kök, G. Pirge, and Y. Aydoğdu, “Isothermal oxidation study on NiMnGa ferromagnetic shape memory alloy at 600-1000 °c,” *Appl. Surf. Sci.*, vol. 268, pp. 136–140, Mar. 2013.
[47] K. S. Kim, K. K. Jee, Y. B. Kim, W. Y. Jang, and S. H. Han, “Effect of oxidation on transformation and deformation behavior in Ni-Ti alloy,” *Eur. Phys. J. Spec. Top. 2008 1581*, vol. 158, no. 1, pp. 67–71, 2008.
[48] Y. Matsumoto, “Energy positions of oxide semiconductors and photocatalysis with iron complex oxides,” *J. Solid State Chem.*, vol. 126, no. 2, pp. 227–234, Nov. 1996.
[49] M. Eder, K. Terakura, and J. Hafner, “Initial stages of oxidation of (100) and (110) surfaces of iron caused by water,” *Phys. Rev. B - Condens. Matter Mater. Phys.*, vol. 64, no. 11, p. 115426, Aug. 2001.
[50] P. H. Holloway and J. B. Hudson, “Chemical changes in secondary electron emission during oxidation of nickel (100) and (111) crystal surfaces,” *J. Vac. Sci. Technol.*, vol. 12, p. 647, 1975.
[51] H. Scheidt, M. Glöbl, and V. Dose, “The oxidation of nickel: A study of empty electronic states by inverse photoemission and soft X-ray appearance potential spectroscopy,” *Surf. Sci.*, vol. 112, no. 1–2, pp. 97–110, Dec. 1981.
[52] K. Terakura, T. Oguchi, A. R. Williams, and J. Kübler, “Band theory of insulating transition-metal monoxides: Band-structure calculations,” *Phys. Rev. B*, vol. 30, no. 8, pp.

4734–4747, Oct. 1984.
[53] J. C. Védrine, “Metal Oxides in Heterogeneous Oxidation Catalysis: State of the Art and Challenges for a More Sustainable World,” *ChemSusChem*, vol. 12, no. 3, pp. 577–588, Feb. 2019.
[54] J. A. Altham, J. H. McLain, and G. M. Schwab, “The Reactivity of Nickel Oxide,” *Zeitschrift fur Phys. Chemie*, vol. 74, no. 3–6, pp. 139–145, 1971.
[55] W. Komatsu, H. Ooki, I. Naka, and A. Kobayashi, “Synergetic effect of oxide catalysts with different dopents on catalytic activity. I. Nickel oxide and zinc oxide for carbon monoxide oxidation,” *J. Catal.*, vol. 15, no. 1, pp. 43–49, Sep. 1969.
[56] A. Rahafrooz and S. Pourkamali, “High-frequency thermally actuated electromechanical resonators with piezoresistive readout,” *IEEE Trans. Electron Devices*, vol. 58, no. 4, pp. 1205–1214, Apr. 2011.
[57] S. C. Masmanidis, R. B. Karabalin, I. De Vlaminck, G. Borghs, M. R. Freeman, and M. L. Roukes, “Multifunctional nanomechanical systems via tunably coupled piezoelectric actuation,” *Science (80-.).*, vol. 317, no. 5839, pp. 780–783, Aug. 2007.
[58] M. D. Manrique-Juárez *et al.*, “Switchable molecule-based materials for micro- and nanoscale actuating applications: Achievements and prospects,” *Coordination Chemistry Reviews*, vol. 308. Elsevier B.V., pp. 395–408, 01-Feb-2016.
[59] T. Wada and M. Taya, “Spring-based actuators,” no. July 2002, pp. 294–302, 2002.
[60] A. Servant, F. Qiu, M. Mazza, K. Kostarelos, and B. J. Nelson, “Controlled in vivo swimming of a swarm of bacteria-like microrobotic flagella,” *Adv. Mater.*, vol. 27, no. 19, pp. 2981–2988, 2015.
[61] P. Pouponneau, G. Bringout, and S. Martel, “Therapeutic Magnetic Microcarriers Guided by Magnetic Resonance Navigation for Enhanced Liver Chemoembilization: A Design Review,” *Annals of Biomedical Engineering*, vol. 42, no. 5. Springer US, pp. 929–939, May-2014.
[62] V. Haehnel, S. Fähler, L. Schultz, and H. Schlörb, “Electrodeposition of Fe70Pd30nanowires from a complexed ammonium-sulfosalicylic electrolyte with high stability,” *Electrochem. commun.*, vol. 12, no. 8, pp. 1116–1119, 2010.
[63] T. Yamamoto, M. Taya, Y. Sutou, Y. Liang, T. Wada, and L. Sorensen, “Magnetic field-induced reversible variant rearrangement in Fe-Pd single crystals,” *Acta Mater.*, vol. 52, no. 17, pp. 5083–5091, Oct. 2004.
[64] M. Taya, C. Xu, T. Matsuse, and S. Muraishi, “Molecular dynamics model for nano-motions of FePd nanohelices,” *J. Appl. Phys.*, vol. 121, no. 15, p. 154302, Apr. 2017.
[65] T. W. Duerig, K. N. Melton, and D. Stöckel, *Engineering Aspects of Shape Memory Alloys*. 2013.
[66] M. Matsui, H. Yamada, and K. Adachi, “A New Low Temperature Phase (fct) of Fe–Pd Invar,” *J. Phys. Soc. Japan*, vol. 48, no. 6, pp. 2161–2162, Jun. 1980.
[67] R. W. Cahn, “Binary Alloy Phase Diagrams-Second edition. T. B. Massalski, Editor-in-Chief; H. Okamoto, P. R. Subramanian, L. Kacprzak, Editors. ASM International, Materials Park, Ohio, USA. December 1990. xxii, 3589 pp., 3 vol., hard- back. $995.00 the set,” *Adv. Mater.*, vol. 3, no. 12, pp. 628–629, Dec. 1991.
[68] R. Oshima, “Successive martensitic transformations in Fe- Pd alloys,” *Scr. Metall.*, vol. 15, no. i, pp. 829–833, 1981.
[69] J. Buschbeck, S. Hamann, A. Ludwig, B. Holzapfel, L. Schultz, and S. Fähler, “Correlation of phase transformations and magnetic properties in annealed epitaxial Fe–Pd

magnetic shape memory alloy films," *J. Appl. Phys.*, vol. 107, no. 11, p. 113919, Jun. 2010.
[70] K. Seki, H. Kura, T. Sato, and T. Taniyama, "Size dependence of martensite transformation temperature in ferromagnetic shape memory alloy FePd," *J. Appl. Phys.*, vol. 103, no. 6, p. 063910, Mar. 2008.
[71] R. Oshima and M. Sugiyama, "MARTENSITE TRANSFORMATIONS IN Fe-Pd ALLOYS," *Le J. Phys. Colloq.*, vol. 43, no. C4, pp. C4-383-C4-388, Dec. 1982.
[72] K. Z. Rozman *et al.*, "Austenite-martensite transformation in electrodeposited Fe70Pd30NWs: A step towards making bio-nano-actuators tested on in vivo systems," *Smart Mater. Struct.*, vol. 27, no. 3, 2018.
[73] C. Brett, *Electrochemistry: Principles, Methods and Applications*. Oxford University Press, 1994.
[74] K. J. Bryden and J. Y. Ying, "Electrodeposition synthesis and hydrogen absorption properties of nanostructured palladium-iron alloys," *Nanostructured Mater.*, vol. 9, no. 1–8, pp. 485–488, Jan. 1997.
[75] D. R. Gabe, "The role of hydrogen in metal electrodeposition processes," *J. Appl. Electrochem.*, vol. 27, no. 8, pp. 908–915, 1997.
[76] K. Asaka, T. Tadaki, and Y. Hirotsu, "Transmission electron microscopy and electron diffraction studies on martensitic transformations in nanometre-sized particles of Au-Cd alloys of near-equiatomic compositions," vol. 82, no. 3, pp. 463–478, Feb. 2002.
[77] K. Asaka, Y. Hirotsu, and T. Tadaki, "Transmission electron microscopy and electron diffraction study on structure and phase transformation of nanometre-sized Fe-15-30 at.% Ni alloy particles," *J. Electron Microsc. (Tokyo).*, vol. 48, no. 4, pp. 387–391, 1999.
[78] T. Tadaki, K. Kifune, Y. Kubota, and H. Yamaoka, "Stabilization of the gamma phase in Fe-Pt alloy nanoparticles with low Pt contents prepared by chemical synthesis method," *Mater. Sci. Eng. A*, vol. 438–440, no. SPEC. ISS., pp. 407–410, Nov. 2006.
[79] Y. Matsuoka, K. Suzuki, and N. Kudo, "Size effect for phase stability on Au-Cd-Ag of phase boundary composition," *J. Alloys Compd.*, vol. 577, no. SUPPL. 1, pp. S521–S524, Nov. 2013.
[80] Accuratus, "Aluminum Oxide | Al2O3 Material Properties," 2013. [Online]. Available: https://accuratus.com/alumox.html. [Accessed: 06-Sep-2018].
[81] M. Taya *et al.*, "Residual stresses in Fe-Pd nanomaterials in alumina template," *Int. J. Solids Struct. (under Rev.*, 2020.
[82] M. Taya, E. Van Volkenburgh, M. Mizunami, and S. Nomura, *Bioinspired Actuators and Sensors*. Cambridge University Press, 2016.
[83] J. D. Eshelby, "The determination of the elastic field of an ellipsoidal inclusion, and related problems," *Proc. R. Soc. London. Ser. A. Math. Phys. Sci.*, vol. 241, no. 1226, pp. 376–396, Aug. 1957.
[84] T. Mori and K. Tanaka, "Average stress in matrix and average elastic energy of materials with misfitting inclusions," *Acta Metall.*, vol. 21, no. 5, pp. 571–574, May 1973.
[85] T. Mura, *Micromechanics of Defects in Solids*. Springer Science & Business Media, 1987.
[86] M. Taya, *Electronic Composites*. 2005.
[87] S. Muraishi and M. Taya, "Average Eshelby tensor and elastic field for helical inclusion problems," *Int. J. Solids Struct.*, vol. 180–181, pp. 125–136, Dec. 2019.
[88] M. Taya, K. E. Lulay, and D. J. Lloyd, "Strengthening of a particulate metal matrix composite by quenching," *Acta Metall. Mater.*, vol. 39, no. 1, pp. 73–87, Jan. 1991.

[89] M. Taya and T. Mori, “Dislocations punched-out around a short fiber in a short fiber metal matrix composite subjected to uniform temperature change,” *Acta Metall.*, vol. 35, no. 1, pp. 155–162, Jan. 1987.
[90] S. Shibata, T. Mori, and M. Taya, “Stress relaxation by dislocation punching to radial direction from a long fiber in a composite,” *Scr. Metall. Mater.*, vol. 26, no. 3, pp. 363–368, Feb. 1992.
[91] S. Muraishi, “Formulation of Eshelby’s inclusion problem by BIEM (boundary integral equation method) and PDD (parametric dislocation dynamics),” *Mech. Mater.*, vol. 74, pp. 41–55, Jul. 2014.
[92] H. Masuda, K. Fukuda, N. Series, and N. Jun, “Ordered Metal Nanohole Arrays Made by a Two-Step Replication of Honeycomb Structures of Anodic Alumina Ofdered Metal Nanohole Arrays Made by a Two-Step Replication of Honeycomb Structures of Anodic Alumina,” vol. 268, no. 5216, pp. 1466–1468, 1995.
[93] A. P. Li, F. Müller, A. Bimer, K. Nielsch, and U. Gösele, “Hexagonal pore arrays with a 50-420 nm interpore distance formed by self-organization in anodic alumina,” *J. Appl. Phys.*, vol. 84, no. 11, pp. 6023–6026, 1998.
[94] H. Schlörb *et al.*, “Magnetic nanowires by electrodeposition within templates,” *Phys. Status Solidi Basic Res.*, vol. 247, no. 10, pp. 2364–2379, Aug. 2010.
[95] Y. Wu *et al.*, “Composite mesostructures by nano-confinement,” *Nat. Mater.*, vol. 3, no. 11, pp. 816–822, 2004.
[96] C. Xu, “Synthesis and Characterization of Fe70Pd30 Nanohelices,” 2017.
[97] C. J. Ji and P. C. Searson, “Synthesis and Characterization of Nanoporous Gold Nanowires,” *J. Phys. Chem. B*, vol. 107, p. 1194, 2003.
[98] N. S. Gajbhiye, S. Sharma, and R. S. Ningthoujam, “Synthesis of self-assembled monodisperse 3 nm FePd nanoparticles: Phase transition, magnetic study, and surface effect,” *J. Appl. Phys.*, vol. 104, no. 12, p. 123906, Dec. 2008.
[99] S. Kawaguchi *et al.*, “High-throughput powder diffraction measurement system consisting of multiple MYTHEN detectors at beamline BL02B2 of SPring-8,” *Rev. Sci. Instrum.*, vol. 88, no. 8, p. 085111, Aug. 2017.
[100] S. Yamamoto, S. Takao, S. Muraishi, C. Xu, and M. Taya, “Synthesis of Fe70Pd30 nanoparticles and their surface modification by zwitterionic linker,” *Mater. Chem. Phys.*, vol. 234, pp. 237–244, Aug. 2019.
[101] W. Y. Zhou, Y. B. Li, Z. Q. Liu, D. S. Tang, X. P. Zou, and G. Wang, “Self-organized formation of hexagonal nanopore arrays in anodic alumina,” *Chinese Phys.*, vol. 10, no. 3, pp. 218–222, 2001.
[102] D. Yang *et al.*, “Electrochemical synthesis of metal and semimetal nanotube-nanowire heterojunctions and their electronic transport properties,” *Chem. Commun.*, no. 17, pp. 1733–1735, Apr. 2007.
[103] J. Liu *et al.*, “Electrochemical fabrication of single-crystalline and polycrystalline Au nanowires: The influence of deposition parameters,” *Nanotechnology*, vol. 17, no. 8, pp. 1922–1926, Apr. 2006.
[104] M. Paunovic, *Fundamentals of Electrochemical Deposition*. John Wiley & Sons, Ltd, 1998.
[105] Z. F. Zhou, Y. Pan, Y. C. Zhou, and L. Yang, “Growth dynamics and thermal stability of Ni nanocrystalline nanowires,” *Appl. Surf. Sci.*, vol. 257, no. 23, pp. 9991–9995, Sep. 2011.

[106] M. E. T. Molares, A. G. Balogh, T. W. Cornelius, R. Neumann, and C. Trautmann, "Fragmentation of nanowires driven by Rayleigh instability," *Appl. Phys. Lett.*, vol. 85, no. 22, pp. 5337–5339, Nov. 2004.
[107] M. E. Toimil-Molares, "Characterization and properties of micro-and nanowires of controlled size, composition, and geometry fabricated by electrodeposition and ion-track technology," *Beilstein J. Nanotechnol*, vol. 3, pp. 860–883, 2012.
[108] Q. Meng, Y. Rong, and T. Y. Hsu, "Nucleation barrier for phase transformations in nanosized crystals," *Phys. Rev. B - Condens. Matter Mater. Phys.*, vol. 65, no. 17, pp. 1–7, May 2002.
[109] X. Zhao, Y. Liang, and Z. Hu, "Investigation on the martensitic transformation in γ-Fe(n) nanoparticles," *Nanostructured Mater.*, vol. 7, no. 3, pp. 313–325, Mar. 1996.
[110] C. Chiew, "2D/3D Helmholtz Coil for FePd Nanorobot Propulsion," 2019.
[111] W. Zhao, S. J. Carey, S. E. Morgan, and C. T. Campbell, *Energetics of adsorbed formate and formic acid on Ni(111) by calorimetry*, vol. 352. Academic Press Inc., 2017, pp. 300–304.
[112] R. C. Catapan, A. A. M. Oliveira, Y. Chen, and D. G. Vlachos, "DFT study of the water-gas shift reaction and coke formation on Ni(111) and Ni(211) surfaces," *J. Phys. Chem. C*, vol. 116, no. 38, pp. 20281–20291, Sep. 2012.
[113] J. V. Barth, G. Costantini, and K. Kern, "Engineering atomic and molecular nanostructures at surfaces," *Nature*, vol. 437, no. 7059. pp. 671–679, 29-Sep-2005.
[114] I. Lynch, T. Cedervall, M. Lundqvist, C. Cabaleiro-Lago, S. Linse, and K. A. Dawson, "The nanoparticle-protein complex as a biological entity; a complex fluids and surface science challenge for the 21st century," *Advances in Colloid and Interface Science*, vol. 134–135. pp. 167–174, 31-Oct-2007.
[115] B. Kasemo, "Biological surface science," *Surf. Sci.*, vol. 500, no. 1–3, pp. 656–677, Mar. 2002.
[116] T. L. Silbaugh, E. M. Karp, and C. T. Campbell, "Energetics of formic acid conversion to adsorbed formates on Pt(111) by transient calorimetry," *J. Am. Chem. Soc.*, vol. 136, no. 10, pp. 3964–3971, Mar. 2014.
[117] M. R. Columbia, A. M. Crabtree, and P. A. Thiel, "The Temperature and Coverage Dependences of Adsorbed Formic Acid and Its Conversion to Formate on Pt(111)," *J. Am. Chem. Soc.*, vol. 114, no. 4, pp. 1231–1237, Feb. 1992.
[118] N. R. Avery, "Reaction of HCOOH with a Pt(111)-O surface; identification of adsorbed monodentate formate," *Appl. Surf. Sci.*, vol. 14, no. 2, pp. 149–156, 1983.
[119] T. Matsumoto, A. Bandara, J. Kubota, C. Hirose, and K. Domen, "Adsorption and reaction of formic acid on a (2 × 2) NiO(111)/Ni(111) surface. 3. IRAS studies on the characterization of reaction sites using CO and the behavior of surface hydroxyl species," *J. Phys. Chem. B*, vol. 102, no. 16, pp. 2979–2984, Apr. 1998.
[120] A. Bandara, J. Kubota, A. Wada, K. Domen, and C. Hirose, "Adsorption and decomposition of formic acid (DCOOD) on NiO(111) and Ni(111) surfaces probed by SFG," *Appl. Phys. B Lasers Opt.*, vol. 68, no. 2–3, pp. 573–578, Mar. 1999.
[121] K. Kusafuka *et al.*, "Time-resolved study of formate on Ni(1 1 1) by picosecond SFG spectroscopy," in *Surface Science*, 2002, vol. 502–503, pp. 313–318.
[122] C. Houtman and M. A. Barteau, "Reactions of formic acid and formaldehyde on Rh(111) and Rh(111)-(2 × 2)O surfaces," *Surf. Sci.*, vol. 248, no. 1–2, pp. 57–76, May 1991.
[123] C. Xu and D. W. Goodman, "Identification of New Decomposition Intermediates of

Formic Acid on the O/Mo(110) Surface," *J. Am. Chem. Soc.*, vol. 117, no. 49, pp. 12354–12355, 1995.
[124] J. R. Rostrup-Nielsen, "Activity of nickel catalysts for steam reforming of hydrocarbons," *J. Catal.*, vol. 31, no. 2, pp. 173–199, 1973.
[125] K. R. Hwang, C. B. Lee, and J. S. Park, "Advanced nickel metal catalyst for water-gas shift reaction," *J. Power Sources*, vol. 196, no. 3, pp. 1349–1352, Feb. 2011.
[126] W. Erley and D. Sander, "The adsorption and decomposition of formic acid on Ni(111): The identification of formic anhydride by vibrational spectroscopy," *J. Vac. Sci. Technol. A Vacuum, Surfaces, Film.*, vol. 7, no. 3, pp. 2238–2244, May 1989.
[127] J. B. Benziger and G. R. Schoofs, "Influence of adsorbate interactions on heterogeneous reaction kinetics. Formic acid decomposition on nickel," *J. Phys. Chem.*, vol. 88, no. 19, pp. 4439–4444, 1984.
[128] K. Domen *et al.*, "SFG study of unstable surface species by picosecond pump-probe method," *Surf. Sci.*, vol. 427–428, pp. 349–357, Jun. 1999.
[129] H. M. Ajo, H. Ihm, D. E. Moilanen, and C. T. Campbell, "Calorimeter for adsorption energies of larger molecules on single crystal surfaces," *Rev. Sci. Instrum.*, vol. 75, no. 11, pp. 4471–4480, Nov. 2004.
[130] W. Lew, O. Lytken, J. A. Farmer, M. C. Crowe, and C. T. Campbell, "Improved pyroelectric detectors for single crystal adsorption calorimetry from 100 to 350 K," in *Review of Scientific Instruments*, 2010, vol. 81, no. 2.
[131] O. Lytken, W. Lew, J. J. W. Harris, E. K. Vestergaard, J. M. Gottfried, and C. T. Campbell, "Energetics of cyclohexene adsorption and reaction on Pt(111) by low-temperature microcalorimetry," *J. Am. Chem. Soc.*, vol. 130, no. 31, pp. 10247–10257, Aug. 2008.
[132] A. S. Coolidge, "The vapor density and some other properties of formic acid," *J. Am. Chem. Soc.*, vol. 50, no. 8, pp. 2166–2178, Aug. 1928.
[133] C. T. Campbell and J. R. V. Sellers, "Enthalpies and entropies of adsorption on well-defined oxide surfaces: Experimental measurements," *Chemical Reviews*, vol. 113, no. 6. American Chemical Society, pp. 4106–4135, 12-Jun-2013.
[134] C. T. Campbell and J. R. V. Sellers, "The entropies of adsorbed molecules," *J. Am. Chem. Soc.*, vol. 134, no. 43, pp. 18109–18115, Oct. 2012.
[135] R. C. Millikan and K. S. Pitzee, "Infrared spectra and vibrational assignment of monomeric formic acid," *J. Chem. Phys.*, vol. 27, no. 6, pp. 1305–1308, 1957.
[136] T. J. Lawton, J. Carrasco, A. E. Baber, A. Michaelides, and E. C. H. Sykes, "Hydrogen-bonded assembly of methanol on Cu(111)," *Phys. Chem. Chem. Phys.*, vol. 14, no. 33, pp. 11846–11852, Sep. 2012.
[137] T. J. Lawton, J. Carrasco, A. E. Baber, A. Michaelides, and E. C. H. Sykes, "Visualization of hydrogen bonding and associated chirality in methanol hexamers," *Phys. Rev. Lett.*, vol. 107, no. 25, Dec. 2011.
[138] M. D. Marcinkowski, C. J. Murphy, M. L. Liriano, N. A. Wasio, F. R. Lucci, and E. C. H. Sykes, "Microscopic View of the Active Sites for Selective Dehydrogenation of Formic Acid on Cu(111)," *ACS Catal.*, vol. 5, no. 12, pp. 7371–7378, Oct. 2015.
[139] A. Bandara, J. Kubota, A. Wada, K. Domen, and C. Hirose, "Adsorption and reactions of formic acid on (2×2)-NiO(111)/Ni(111) surface. 2. IRAS study under catalytic steady-state conditions," *J. Phys. Chem. B*, vol. 101, no. 3, pp. 361–368, Jan. 1997.
[140] M. Bowker, S. Haq, R. Holroyd, P. M. Parlett, S. Poulston, and N. Richardson,

"Spectroscopic and kinetic studies of formic acid adsorption on Cu(110)," *J. Chem. Soc. - Faraday Trans.*, no. 23, pp. 4683–4686, Dec. 1996.
[141] L. H. Dubois, T. H. Ellis, B. R. Zegarski, and S. D. Kevan, "New insights into the kinetics of formic acid decomposition on copper surfaces," *Surf. Sci.*, vol. 172, no. 2, pp. 385–397, Jul. 1986.
[142] J. Wellendorff *et al.*, "A benchmark database for adsorption bond energies to transition metal surfaces and comparison to selected DFT functionals," *Surf. Sci.*, vol. 640, pp. 36–44, 2015.
[143] Y. R. Luo, *Comprehensive handbook of chemical bond energies*. 2007.
[144] Q. Luo, G. Feng, M. Beller, and H. Jiao, "Formic acid dehydrogenation on Ni(111) and comparison with Pd(111) and Pt(111)," *J. Phys. Chem. C*, vol. 116, no. 6, pp. 4149–4156, Feb. 2012.
[145] J. A. Herron, J. Scaranto, P. Ferrin, S. Li, and M. Mavrikakis, "Trends in formic acid decomposition on model transition metal surfaces: A density functional theory study," *ACS Catal.*, vol. 4, no. 12, pp. 4434–4445, Dec. 2014.
[146] A. Mohsenzadeh, T. Richards, and K. Bolton, "DFT study of the water gas shift reaction on Ni(111), Ni(100) and Ni(110) surfaces," *Surf. Sci.*, vol. 644, pp. 53–63, Feb. 2016.
[147] T. L. Silbaugh and C. T. Campbell, "Energies of formation reactions measured for adsorbates on late transition metal surfaces," *Journal of Physical Chemistry C*, vol. 120, no. 44. American Chemical Society, pp. 25161–25172, 17-Nov-2016.
[148] W. Zhao, A. D. Doyle, S. E. Morgan, M. Bajdich, J. K. Nørskov, and C. T. Campbell, "Formic Acid Dissociative Adsorption on NiO(111): Energetics and Structure of Adsorbed Formate," *J. Phys. Chem. C*, vol. 121, no. 50, pp. 28001–28006, Dec. 2017.
[149] A. K. Singh, S. Singh, and A. Kumar, "Hydrogen energy future with formic acid: A renewable chemical hydrogen storage system," *Catalysis Science and Technology*, vol. 6, no. 1. Royal Society of Chemistry, pp. 12–40, 07-Jan-2016.
[150] D. Mellmann, P. Sponholz, H. Junge, and M. Beller, "Formic acid as a hydrogen storage material-development of homogeneous catalysts for selective hydrogen release," *Chemical Society Reviews*, vol. 45, no. 14. Royal Society of Chemistry, pp. 3954–3988, 21-Jul-2016.
[151] P. Dementyev *et al.*, "Water Interaction with Iron Oxides," *Angew. Chemie - Int. Ed.*, vol. 54, no. 47, pp. 13942–13946, Nov. 2015.
[152] W. Zhao, M. Bajdich, S. Carey, A. Vojvodic, J. K. Nørskov, and C. T. Campbell, "Water dissociative adsorption on NiO(111): Energetics and structure of the hydroxylated surface," *ACS Catal.*, vol. 6, no. 11, pp. 7377–7384, 2016.
[153] A. M. Diskin, R. H. Cunningham, and R. M. Ormerod, "The oxidative chemistry of methane over supported nickel catalysts," *Catal. Today*, vol. 46, no. 2–3, pp. 147–154, Nov. 1998.
[154] T. Zhu and M. Flytzani-Stephanopoulos, "Catalytic partial oxidation of methane to synthesis gas over Ni-CeO2," *Appl. Catal. A Gen.*, vol. 208, no. 1–2, pp. 403–417, Feb. 2001.
[155] A. Bandara, J. Kubota, A. Wada, K. Domen, and C. Hirose, "Adsorption and reactions of formic acid on (2×2)-NiO(111)/Ni(111) surface. 1. TPD and IRAS studies under ultrahigh vacuum conditions," *J. Phys. Chem.*, vol. 100, no. 36, pp. 14962–14968, Sep. 1996.
[156] A. Bandara, J. Kubota, A. Wada, K. Domen, and C. Hirose, "Adsorption and decomposition of formic acid on the NiO(111)-p(2 × 2) surface: TPD and steady state

kinetics studies," *Surf. Sci.*, vol. 364, no. 2, Aug. 1996.
[157] M. A. Langell and M. H. Nassir, "Stabilization of NiO(111) thin films by surface hydroxyls," *J. Phys. Chem.*, vol. 99, no. 12, pp. 4162–4169, 1995.
[158] P. R. Norton, R. L. Tapping, and J. W. Goodale, "A photoemission study of the interaction of Ni(100), (110) and (111) surfaces with oxygen," *Surf. Sci.*, vol. 65, no. 1, pp. 13–36, 1977.
[159] T. Okazawa, T. Nishizawa, T. Nishimura, and Y. Kido, "Oxidation kinetics for Ni(111) and the structure of the oxide layers," *Phys. Rev. B - Condens. Matter Mater. Phys.*, vol. 75, no. 3, Jan. 2007.
[160] N. Kitakatsu, V. Maurice, C. Hinnen, and P. Marcus, "Surface hydroxylation and local structure of NiO thin films formed on Ni(111)," *Surf. Sci.*, vol. 407, no. 1–3, pp. 36–58, Jun. 1998.
[161] D. A. King and M. G. Wells, "Molecular beam investigation of adsorption kinetics on bulk metal targets: Nitrogen on tungsten," *Surf. Sci.*, vol. 29, no. 2, pp. 454–482, 1972.
[162] G. Kresse and J. Hafner, "Ab initio molecular dynamics for liquid metals," *Phys. Rev. B*, vol. 47, no. 1, pp. 558–561, 1993.
[163] G. Kresse and J. Furthmüller, "Efficiency of ab-initio total energy calculations for metals and semiconductors using a plane-wave basis set," *Comput. Mater. Sci.*, vol. 6, no. 1, pp. 15–50, 1996.
[164] G. Kresse and J. Furthmüller, "Efficient iterative schemes for ab initio total-energy calculations using a plane-wave basis set," *Phys. Rev. B - Condens. Matter Mater. Phys.*, vol. 54, no. 16, pp. 11169–11186, 1996.
[165] J. P. Perdew, K. Burke, and M. Ernzerhof, "Generalized gradient approximation made simple," *Phys. Rev. Lett.*, vol. 77, no. 18, pp. 3865–3868, 1996.
[166] S. Dudarev and G. Botton, "Electron-energy-loss spectra and the structural stability of nickel oxide: An LSDA+U study," *Phys. Rev. B - Condens. Matter Mater. Phys.*, vol. 57, no. 3, pp. 1505–1509, 1998.
[167] A. D. Doyle, M. Bajdich, and A. Vojvodic, "Theoretical Insights to Bulk Activity Towards Oxygen Evolution in Oxyhydroxides," *Catal. Letters*, vol. 147, no. 6, pp. 1533–1539, Jun. 2017.
[168] A. J. Tkalych, K. Yu, and E. A. Carter, "Structural and Electronic Features of β-Ni(OH)2 and β-NiOOH from First Principles," *J. Phys. Chem. C*, vol. 119, no. 43, pp. 24315–24322, Oct. 2015.
[169] S. Gautier, S. N. Steinmann, C. Michel, P. Fleurat-Lessard, and P. Sautet, "Molecular adsorption at Pt(111). How accurate are DFT functionals?," *Phys. Chem. Chem. Phys.*, vol. 17, no. 43, pp. 28921–28930, Oct. 2015.
[170] B. Hammer, L. B. Hansen, and J. K. Nørskov, "Improved adsorption energetics within density-functional theory using revised Perdew-Burke-Ernzerhof functionals," *Phys. Rev. B - Condens. Matter Mater. Phys.*, vol. 59, no. 11, pp. 7413–7421, 1999.
[171] J. Wellendorff *et al.*, "Density functionals for surface science: Exchange-correlation model development with Bayesian error estimation," *Phys. Rev. B - Condens. Matter Mater. Phys.*, vol. 85, no. 23, Jun. 2012.
[172] G. Kresse and D. Joubert, "From ultrasoft pseudopotentials to the projector augmented-wave method," *Phys. Rev. B - Condens. Matter Mater. Phys.*, vol. 59, no. 3, pp. 1758–1775, Jan. 1999.
[173] X. D. Peng and M. A. Barteau, "Acid-base reactions on model MgO surfaces," *Catal.*

Letters, vol. 12, no. 1–3, pp. 245–253, Mar. 1992.
[174] S. Wang, V. Vorotnikov, J. E. Sutton, and D. G. Vlachos, “Brønsted-evans-polanyi and transition state scaling relations of furan derivatives on pd(111) and their relation to those of small molecules,” *ACS Catal.*, vol. 4, no. 2, pp. 604–612, Feb. 2014.
[175] W. Lee, “The anodization of aluminum for nanotechnology applications,” *Jom*, vol. 62, no. 6, pp. 57–63, Jun. 2010.